ON TACTILE SENSING AND DISPLAY

A DISSERTATION
SUBMITTED TO THE DEPARTMENT OF MECHANICAL ENGINEERING
AND THE COMMITTEE ON GRADUATE STUDIES
OF STANFORD UNIVERSITY
IN PARTIAL FULFILLMENT OF THE REQUIREMENTS
FOR THE DEGREE OF
DOCTOR OF PHILOSOPHY

William R. Provancher
August 2003

I certify that I have read this dissertation and that in my opinion it is fully adequate, in scope and quality, as a dissertation for the degree of Doctor of Philosophy.

Mark R. Cutkosky, Principal Advisor

I certify that I have read this dissertation and that in my opinion it is fully adequate, in scope and quality, as a dissertation for the degree of Doctor of Philosophy.

Kenneth J. Waldron

I certify that I have read this dissertation and that in my opinion it is fully adequate, in scope and quality, as a dissertation for the degree of Doctor of Philosophy.

Thomas W. Kenny

Approved for the University Committee on Graduate Studies.

Abstract

With the aid of telerobotics it has become possible to manipulate an object across the world or even on another planet. But how can the user feel what the remote robot hand is touching? The challenges associated with displaying tactile sensations are formidable, requiring the ability to recreate changing contact geometries, pressure distributions and vibrations at the user's fingertips. Despite years of research, telerobotic consoles provide their operators mainly with visual feedback and overall handling forces. The experience is akin to manipulating an object with fireplace tongs. The goal of the research presented herein is to extend the capabilities of current systems by imparting tactile sensations to their users.

This thesis presents new methods of tactile sensing and display for dexterous telemanipulation, i.e., telemanipulation that involves imparting forces and motions with the fingertips. The motivating hypothesis for this work is that sensing and displaying contact location provides essential information for dexterous telemanipulation. A new tactile sensor is presented that consists of an array of curvature-measuring elements. The curvature measurements provide information for manipulation planning and control and provide an estimate of the local object geometry, useful for grasp stability analysis. The approach is validated in simulation and experimentally.

The companion to the sensor is a display that allows users to track finger/object contact locations. The tactile display renders the location of the contact centroid on a user's fingertip and thereby provides the user with cues about object motion and curvature. The ability of users to discriminate among different object curvature and motion conditions is investigated in a series of experiments involving real and virtual objects rendered via the display. The results indicate that contact location provides an important cue for dexterous telemanipulation and that, for gently curved objects, the performance of users with the display is comparable to their performance when they touch objects directly with their own fingertips.

For Pam

Acknowledgments

The path to a Ph.D. has been a long and winding one. The route was not always well illuminated, but there have been many people who provided guidance and support along the way. I am grateful for their time, friendship, and words of wisdom.

I'd like to start by thanking my advisor, Mark Cutkosky. You took a chance on me by allowing a "composites guy" with no robotics experience to work in your lab. Because of this opportunity, I have learned and grown as an engineer and a researcher. I'd also like to thank the members of my reading and defense committees: Chris Chafe, Tom Kenny, Günter Niemeyer, and Ken Waldron. Thanks for your suggestions, they were instrumental in my completing this work.

I've been fortunate enough to work with the extremely talented and friendly members of the Dexterous Manipulation Lab. I had only a brief overlap with some of the previous members of the lab: Turner, Costa, Allison and Chris, but they helped me get started on the right track. As for the current members, I don't know where to begin. Sean, Weston, Jonathan, Moto, Arthur-Trey, Karpick, Dan, Miguel, Kevin, Eric, Sangbae and Li, it's been great getting to know all of you. I am especially indebted to Weston and Sean. I will miss our late afternoon "sugar breaks." Weston, you have always been quick to lend a helping hand. Sean, your critical eye was not always welcome, but it is greatly appreciated.

I'd like to express my gratitude to Dr. Herb Rauch. Thanks for your help and patience in developing the formal mathematical model for my sensor and your tremendous effort in editing and proofreading the paper I presented at ISER02. It was also particularly well timed.

I've also benefited from a foster research group in Günter Niemeyer's Telerobotics Lab. Vanessa and Katherine, because of your hard work the contact location experiments actually came to life in RTai Linux. Katherine, I particularly appreciate the many late nights you put in and your diligence in coping with the hiccups along the way. Günter,

thanks for playing “devil’s advocate” in our many philosophical discussions about contact displays and experiments.

I want to thank researchers from the “haptics community” for their many suggestions. My discussions with Susan Lederman, Rob Howe and Mandayam Srinivason were enlightening and helped me in thinking through the contact display experiments.

I’d also like to acknowledge the staff of CDR: Judy Lee, Jeff Aldrich and Alison Kather, for their administrative, behind the scenes support.

Thanks to James Hetfield and Chris Cornell for inspiration and Puma for entertainment. They really got me through the rough times.

I’d like to thank my parents and my brother, Jason, for supporting me over the years. I want to thank the Beilkes and Despreses, each of whom have been a surrogate family to me. Thanks also to Andre, Paul, Rob, and John for being good friends over the years. Most of all I’d like to thank my wife, Pam, for her endless encouragement and forgiving my being late for dinner.

I’d also like to acknowledge the National Science Foundation that supported my research under grant NSF/IIS-0099636.

Contents

Tables

Figures

1 Introduction

We use our hands every day to assess the size, shape, and texture of objects. We sense and interpret tactile stimuli from our environment and perform tasks with our hands in a nearly instinctual manner. The ability to discriminate among surface textures, sense incipient slip, and roll an object between fingers without dropping it can be attributed to the specialized mechanoreceptors in the hand. These touch receptors possess unrivaled range and acuity. They respond to both static and dynamic stimuli as well as temperature and pain. We are also equipped with reflexes and automatic responses (e.g., grasp force regulation) that allow us to make use of tactile information without expending cognitive effort. Despite the obvious importance of tactile cues in our everyday lives, the subject of tactile display for teleoperators, virtual reality, and more generally, human/machine interfaces, has only recently received significant attention.

This thesis presents new methods of tactile sensing and display. The goal of this research is to bring the level of tactile sensitivity and acuity that humans possess to telemanipulators and other human/machine interfaces. A new method for measuring local object geometry is presented based on an array of curvature measurements. Such information is indispensable for coordinating finger motions for object manipulation. Unfortunately, it is more the exception than the rule that even a portion of this information is relayed to teleoperators. Devising a device to display the full sensation of contact continues to elude researchers. Most commonly, researchers will present an abstraction of contact geometry and pressure with a pin array display. These devices recreate a reasonable facsimile of shape at the contact, but their large package size makes them impractical for use outside the laboratory. The method of displaying contact presented herein, represents a further abstraction. Rather than presenting the shape of the contact, a more minimalist approach of displaying only its centroid is proposed. Packaging and actuation requirements for this approach are modest in comparison to previous approaches. Results of experiments with human subjects demonstrate that it provides them with cues necessary to ascertain object curvature and motion capabilities.

1.1 Motivation

To date, telemanipulation systems have relied heavily on vision feedback and have required experienced operators. It has been shown, however, that adding the sense of touch to these systems connects the operator to the remote environment, making the system more intuitive [Dennerlein et al. 1997, Sheridan 1992].

Similarly, for virtual reality, when advanced graphics and sound are augmented by force and vibration feedback, one's perception is altered and one becomes immersed in an artificial reality [Burdea 1996].

Perhaps even more important than the sense of realism that tactile feedback creates is its ability to leverage innate human tactile ability. With tactile sensation at their fingertips humans can bring their extensive experience in handling objects to bear on the problem at hand. In areas where touch is extremely important, such as medicine, we create the ability for telesurgeons to palpate and probe biological tissue as if they were touching it with their own hands.

1.2 Contributions

The major contributions of this thesis are:

- A new sensor and mathematical framework for measuring local object geometry via an array of curvature measurements are presented. The sensor is analyzed and its inherent accuracy and sensitivity are determined numerically and in experiments.
- A new approach to tactile display based on displaying the centroid of contacts for telemanipulation and virtual reality is developed and tested.
- Evaluation of human perception of contact location feedback in prototypical manipulation tasks is conducted.
- Thresholds for cutaneous length-based perception, as used in rolling objects between the fingers, are determined.

1.3 Thesis Outline

This thesis is organized into five chapters. This chapter provides an introduction to and motivation for my research in tactile sensing and display and lists the contributions of this work.

Chapter 2 provides relevant background in human tactile sensing and perception. The physical parameters and role of human mechanoreception are outlined. This chapter also provides an overview of methods from psychophysics that are useful for evaluating human performance and the effectiveness of new haptic devices. Specific attention is given to the methods employed in the tests reported in chapter 4.

Chapter 3 introduces an approach for sensing local object geometry via an array of curvature measurements and reviews previous tactile array sensor technologies. An approach for surface reconstruction using Fourier series basis functions is presented and validated by simulation and experiments. A prototype incorporating a linear array of curvature measuring elements was fabricated to experimentally validate the design. Sensor design, construction and experimental results are presented. Additional background on sensor circuitry and thermal modeling is provided in Appendix A.

Chapter 4 reviews the design of current tactile displays and introduces the idea of displaying only the location of the centroid of contacts to users of telemanipulation and virtual reality systems. A prototype that renders contacts along the length of a single finger was designed and fabricated to investigate the approach. The device was mounted to a force feedback device to render environmental interaction forces. Human subject testing was conducted with virtual environments to evaluate the device and the user’s relevant perception. The contact location display design and test hardware are presented along with results of initial device evaluation in human subjects experiments. Additional details of the device design can be found in Appendix B. An in-depth derivation of the kinematics used in the curvature discrimination experiments can be found in Appendix C.

Chapter 5 summarizes the results of this research and suggests future extensions of this work.

2 Human Tactile Sensing and Perception

Designing hardware meant to convey artificial touch to the human hand is a significant challenge. The primary reason is that our hands are incredibly sensitive to even the slightest vibrations over a range from 10-100 Hz. To help define the design requirements of such hardware, it is crucial to understand underlying tactile sensing mechanisms. Not only will this serve as a source of inspiration for improving tactile sensor designs, it will also help focus on which signals are important to communicate and how to communicate them. Although this is requisite knowledge, there is more to consider than simply the neurophysiology of touch. Our sense of touch is really a fusion of tactile and kinesthetic information. The combination of cutaneous and kinesthetic sensing is referred to as haptic perception. At a high level, it is the perception or interpretation of these signals that ultimately interests us.

A field of cognitive psychology, psychophysics, provides methods well suited for understanding haptic perception. Researchers in psychophysics have developed specialized methods for quantifying perceived sensations that accompany physical stimuli, thus providing a systematic approach for evaluating human performance and the effectiveness of new hardware and implementations. The remainder of this chapter provides an overview of human mechanoreception and psychophysics and outlines methods used to evaluate human tactile ability.

2.1 Human Mechanoreception

The human hand contains a complex array of specialized receptors that are rugged enough to survive repeated impacts, while retaining the ability to detect faint vibrations and the softest touch. Neurophysiologists have identified four main types of tactile mechanoreceptors. Each is specialized to isolate specific sensations such as pressure, shear, vibration, or texture.

The sensing element of each of these receptors (a nerve ending) is quite similar; however, each type possesses physical packaging and placement within the skin that is uniquely adapted to its purpose. Figure 2-1 shows a cross-sectional view of the skin on a human fingertip and the placement of specialized touch receptors beneath the skin surface.

Mechanoreceptor types are divided into two categories based on their placement beneath the surface of the skin. Type I receptors are located near the surface of the skin

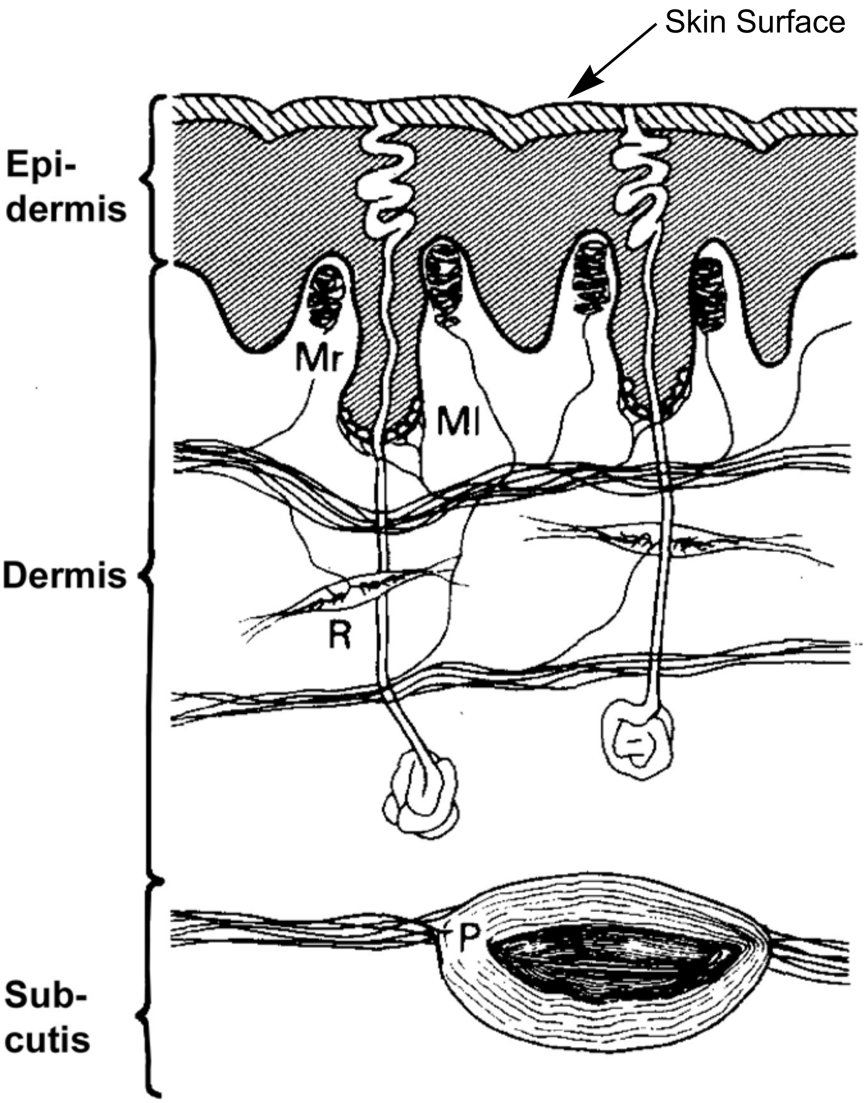

Figure 2-1. Cross-section of human fingertip skin showing four types of mechanoreceptors (with abbreviated labels) and major layers of the skin. Receptor type and abbreviations: FAI, Meissner Corpuscle (Mr); SAI, Merkel disk (MI); SAII, Ruffini ending (R); FAII, Pacinian corpuscle (P) (From Johansson & Vallbo 1983). Reprinted with permission.

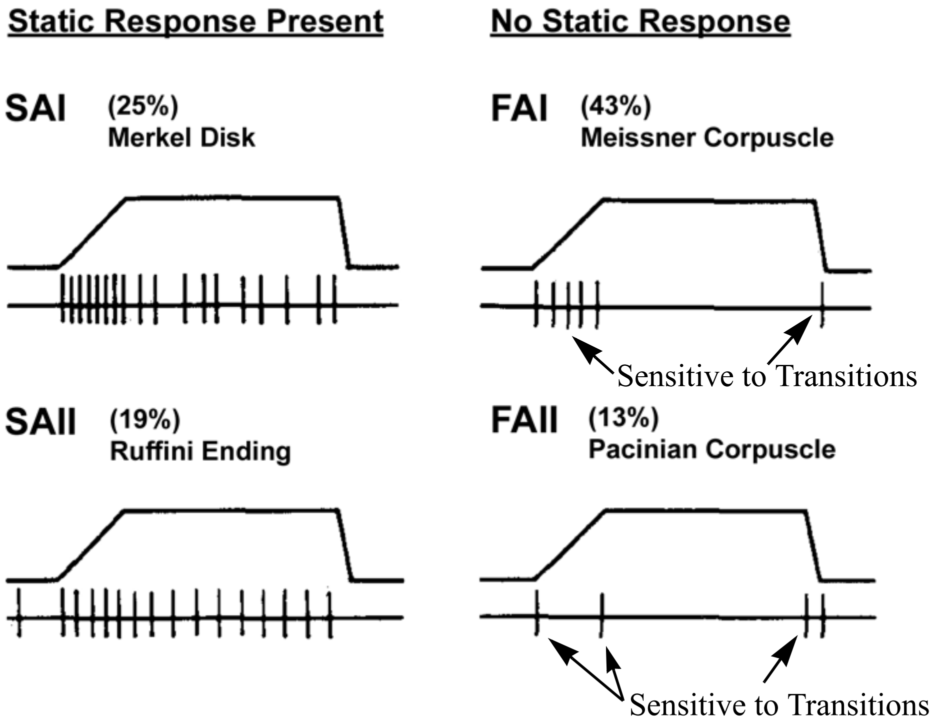

Figure 2-2. Responses of the four types of mechanoreceptors to normal indentation of the skin. The time profile of the indenter is shown above the neural firing pattern for each receptor type. Listed percentages indicate the relative number of each respective receptor type found on the human fingertip (Graphic adapted from Johansson & Vallbo 1983 and Johansson 1991). Reprinted with permission.

between the epidermis and the dermis on the papillary ridges. Type II receptors are located deeper beneath the skin in the dermis. Receptors that lie deeper beneath the skin have larger receptive fields. Correspondingly, fewer type II receptors are observed per unit area of skin.

Receptors are further divided into fast adapting (FA) types, which are sensitive only to transients, and slow adapting (SA) types, which are capable of registering steady state (DC) signals. These two types are analogous to the difference between piezoelectric and piezoresistive sensing elements, respectively. However, unlike man-made piezoelectric and

Table 2-1. Characteristics of mechanoreceptors found in human fingertip skin (sensed parameters suggested by Johnson and Phillips 1981, Johansson, Landstrom, and Lundstrom 1982 and Vallbo and Johansson 1984).

Receptor	Receptor Type	Field Diameter	Frequency Range	Sensed Parameter
Merkel Disks	SAI	3-4 mm	DC-30 Hz	Local skin curvature
Ruffini Endings	SAII	>10 mm	DC-15 Hz	Directional skin stretch
Meissner Corpuscles	FAI	3-4 mm	10-60 Hz	Skin stretch
Pacinian Corpuscles	FAII	>20 mm	50-1000 Hz	Unlocalized vibration

piezoresistive sensors, which provide analog signals, biological mechanoreceptors encode their signals as a series of pulses (as shown in Figure 2-2), similar to digital serial communication. Table 2-1 gives a summary of the characteristics of each mechanoreceptor and the physical parameters they measure.

For a more thorough review of tactile sensing mechanisms, see Johansson and Vallbo [1983] or Vallbo and Johansson [1984] (available on Johansson's Laboratory of Dexterous Manipulation website, http://www.humanneuro.physiol.umu.se/). For a review of research specifically related to the encoding of shape and curvature, such as that reported in section 4.4, see Srinivasan and LaMotte [1991] (available on the MIT Touch Lab website, http://touchlab.mit.edu/).

2.2 Psychophysics

Psychophysics is a subfield of cognitive psychology. It arose out of the desire to quantify the relationship "between sensations in the psychological domain and stimuli in the physical domain" [Gescheider 1997]. It was pioneered in the 1800's by the German scientists E. H. Weber and G. T. Fechner, who were interested in determining sensory thresholds for human perception.

Measuring such thresholds is central to psychophysics. Researchers in this field have measured both absolute and relative thresholds for nearly every imaginable sensory modality (hearing, vision, touch...). The absolute threshold refers to the minimum stimulus necessary to be registered as a perceptible sensation, whereas a relative or difference threshold (JND: Just Noticeable Difference), represents the minimum difference necessary to distinguish between two signals. An example of an absolute threshold could be the minimum amplitude of vibration (at a given frequency) necessary to perceive a vibration. In contrast, one might determine a JND based on the minimum necessary variation in amplitude, about some reference stimulus magnitude, necessary to distinguish between two vibratory signals of a given frequency.

As mentioned previously, the determination of absolute and difference thresholds is central to psychophysics; however, they represent only two of the four paradigms of psychophysics that could be exploited to evaluate haptic performance (the other two are recognition and scaling, which will not be addressed here). For a general introduction to psychophysics, including a review of established testing methods and procedures, see Gescheider [1997]. For a review of research focused specifically on human tactile sensing, see Loomis and Lederman [1986], and Schiff and Foulke [1982].

One interesting side note from this reading is that researchers have found a difference in tactile thresholds based on whether they were determined through active or passive touch. This can be an important consideration when constructing and interpreting psychophysical experiments [Loomis and Lederman 1986]. This is particularly relevant to the experiments in curvature discrimination presented in section 4.4, and will be discussed in more detail along with the experimental results. The remainder of this section provides a brief introduction to some of the concepts and methods that are germane to the experiments described in chapter 4.

2.2.1 Standard Psychophysical Protocol and Interpretation

The field of psychophysics includes well-established procedures and protocol specifically designed to measure human perception of physical stimuli. These procedures were established to reduce the possibility of introducing systematic bias into test procedures. The tests described in chapter 4 were constructed based on standard psychophysical protocol.

These tests employed a paired-comparison, forced-choice protocol, which is also the standard protocol used in an eye exam. The optometrist presents the patient with a series of comparisons, asking the subject to state which lens is more in focus ("Here's lens 'A', and here's lens 'B'."). There are several sources of error and bias, which are often order-based. For this reason, after honing in on the proper prescription, the optometrist will often invert the order of presentation of a pair of lenses. Likewise, standard protocol for establishing JNDs dictates that each combination of stimuli must be presented an even number of times, where the order of presentation is inverted half of the time.

The occurrence of presentation-order bias (also called a *time error*) is quite common and takes several forms. A *time error* results from the fact that there is always a small delay between the presentation of the comparison and standard stimuli. One example of this type of error is when the comparison is judged larger than the standard a larger proportion of the time when the comparison stimulus is presented second. One interpretation of this is that the memory of the first sensation fades with time, leaving a diminished memory of the sensation to compare with the more recent stimulus. This often leads subjects to identify the second stimulus as larger, even if it is not the case.

In addition to balancing presentation order to prevent order bias for sequentially presented stimuli, it is important to balance testing order within a test session (especially as test length increases). This reduces the influence of learning and fatigue in determining thresholds. Note, however, that one can also examine these groups separately (i.e., JNDs for standards completed at the beginning of the test versus at the end) to determine whether learning or fatigue had a substantial effect.

Another source of bias results from the nature of making sequential presentations of stimuli. It is difficult to ensure that the stimuli are judged by the same exact receptors; thus, this type of error is referred to as a *space error*. Though a *space error* is less of an issue when determining audible thresholds, it can be a concern for touch-based experiments. On the other hand, some of these concerns can be mitigated by increasing the number of test trials and by testing a broad number of human subjects.

2.2.1.1 Weber’s Law

It is interesting to examine the relationship between stimulus intensity and the corresponding JND. For a wide range of stimulus values, the JND is proportional to the stimulus intensity. This phenomenon was first observed by E. H. Weber when conducting experiments with weights [Gescheider 1997]. He found that as the mass of the standard increased, so did the incremental mass (JND) that subjects required to discern the difference between the standard and comparison stimuli. In examining data across a broad range, Weber found the JND to be linearly related to the stimulus intensity (stimulus magnitude). Weber’s law, rearranged in the form of the Weber fraction, is shown below.

$$Weber\ Fraction = \frac{JND}{Stimulus\ Intensity} \tag{2.1}$$

This relationship holds over a wide range of sensory modalities and is useful for making comparisons within data sets, though it should be noted that this law breaks down as the intensity of the stimuli approaches the absolute threshold (see Gescheider [1997]).

2.2.2 Classical Psychophysical Methods to Establish JNDs

In classical psychophysics there are three primary methods that are used to evaluate perceptual thresholds: the method of constant stimuli, the method of limits, and the method of adjustment. The experiments presented in chapter 4 establish difference thresholds (JNDs) for curvature and motion, so the description of each of these methods will be expressed with that goal in mind, though it should be noted that these methods can also be used to measure absolute thresholds. Each of these methods has its own merits that should be considered when establishing a testing methodology. The following subsections provide a description of each of these methods and note some of the advantages and disadvantages of each. The greatest attention is given to the method of constant stimuli because it is the method that was used for the experiments described in chapter 4.

2.2.2.1 Method of Constant Stimuli

In this method, a set of constant stimuli are repeatedly presented to test subjects. Typically, stimuli are presented on the order of one hundred times each to establish JNDs. Quite often, experiments are conducted on only a few individuals, necessitating multiple testing sessions; however, one could also pool data from multiple subjects to reduce the time commitment of each subject.

To establish a difference threshold (JND), a set of predetermined comparison stimuli are presented in combination with a standard stimulus (the reference point about which the differences of the comparison stimuli are judged). The comparison stimuli are both greater and smaller in size than the standard stimulus and should be equally spaced (as a general rule, at least six comparison stimuli should be used, three smaller and three larger). Subjects will decide which of the presented stimuli has the particular characteristic of interest (e.g., which is larger).

Preliminary testing is helpful in establishing a range over which the largest of the comparison stimuli is almost always identified as being larger and the smallest of the comparison is almost never mistaken as being larger than the standard stimulus. It should be noted that with all psychophysical testing it is essential to make preliminary test runs (pilot tests) to verify appropriateness of procedures and selection of proper test stimuli before investing considerable time in gathering test data.

Each time a particular stimulus is selected, it is recorded to determine the proportion of times each stimulus is chosen:

$$Proportion = \frac{Number\ of\ Times\ Chosen}{Number\ of\ Times\ Presented} \tag{2.2}$$

The proportion is the number of times that each stimulus is judged as being larger than the standard divided by the number of times that that stimulus is presented. For each stimulus, the proportion is plotted against its associated intensity/magnitude, resulting in a graph called a psychometric function. It should be noted that even though the standard is not compared to a stimulus of identical magnitude, it is compared to both stimuli of greater and smaller magnitude. Therefore, we expect that half of the time the standard will be identified as the larger. Whereas the other data points show the judgement on how an individual comparison stimulus relates to the standard, the data point which corresponds to the magnitude of the standard reflects judgements of the standard with respect to the entire stimulus set. Note that slight deviations from a proportion of 0.5 are expected for the standard, due to possible bias.

These graphs typically resemble an S-shaped curve as shown in Figure 2-3. Fitting an S-shaped curve to points of the psychometric function is supported by theory and experimental findings across many sensing modalities [Gescheider 1997]. The shape of this curve is related to the fact that variations in psychophysical measurements tend to be normally distributed. The S-shaped curve is a cumulative form of this distribution. This is illustrated schematically in Figure 2-4 for the case of three distinct comparison stimuli. In each graph in this figure, two signals are shown (i.e., the standard and comparison stimuli), each represented by a normal distribution.

One can see that if the two signals are of similar magnitude, as in Figure 2-4(a), that there is a large region of overlap between the two distributions. A large region of overlap means that there is a greater possibility for error (interpreting the two stimuli as equal or even interpreting the smaller signal as the larger of the two stimuli). As the difference between the two signals becomes greater, the overlapping region is reduced, and the likelihood of correctly identifying the relative magnitude of the two stimuli increases. As shown in Figure 2-4(a), it is quite likely that the comparison stimulus is indistinguishable from the standard, thus the probability of correctly identifying the comparison stimuli as being greater in magnitude is just slightly greater than chance. For the case shown in Figure 2-4(c), there is very little overlapping region and thus a very small probability of incorrectly identifying the standard as the larger of the two stimuli. However, there remains a small possibility for error.

Even as the stimuli become even more distinct, there will continue to be a small portion of the two distributions that overlap, thus explaining the reason that the S-shaped curve in Figure 2-3 asymptotically approaches a proportion of 1.00 (100% accuracy). Figure 2-4 illustrates this point for the case of comparing the standard stimulus to three comparison stimuli of greater magnitude than the standard. These three graphs correspond qualitatively to the data points found to the right of the standard in Figure 2-3.

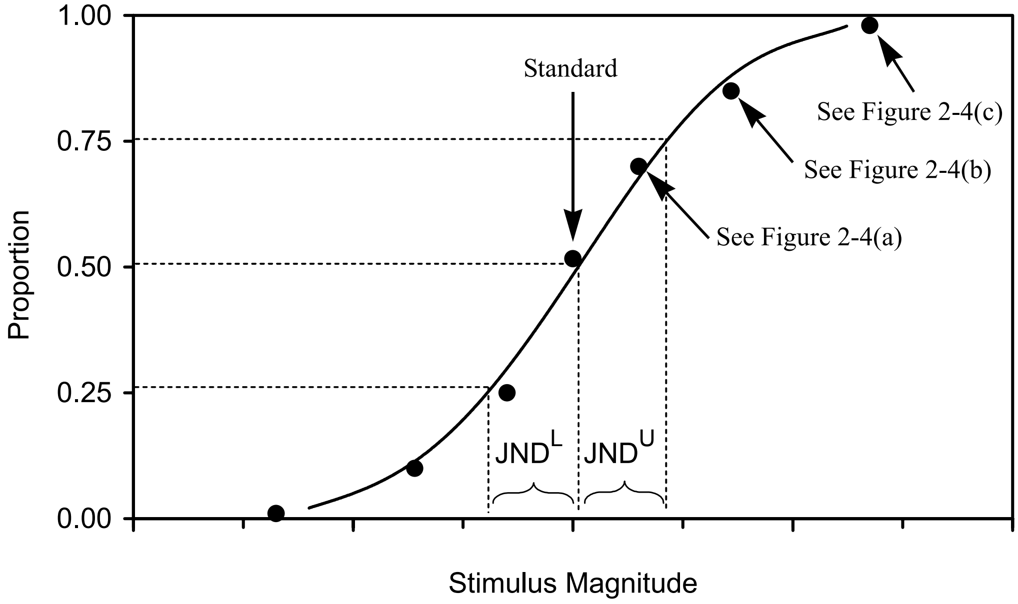

Figure 2-3. Graph of a S-shaped psychometric function. The proportion represents the number of times a stimulus is chosen divided by the times it is presented. The shape of the curve is derived from the fact that psychophysical measurements tend to be normally distributed. The interpretation for the reported proportion and shape of the right side of the curve (i.e., for the comparison stimuli that are larger than the standard) is illustrated in Figures 2-4(a), (b), and (c). Similar reasoning can be used to explain the reported proportions and shape of the left side of the curve (i.e., for the stimuli that are smaller than the standard).

Various methods can be employed to fit psychometric data. Gescheider [1997] outlines a method by which data can be mathematically transformed to a linear function, on which standard least-squares methods can be used. The sigmoidal function can be trans-

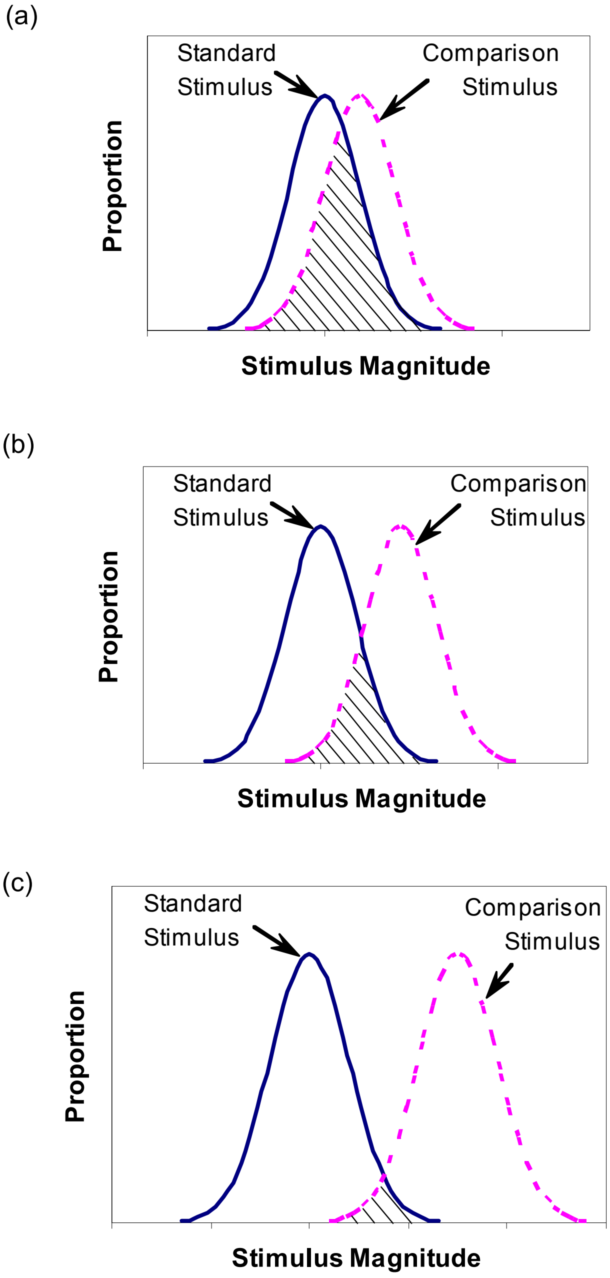

Figure 2-4. The variations in psychophysical measurements tend to be normally distributed. Pairs of stimuli are represented by neighboring normal distributions. In each of the cases shown, the comparison stimulus is greater in magnitude than the standard. As the overlapping region of the two distributions decreases, the probability of correctly identifying the comparison stimulus as larger increases. As shown in (a), it is quite likely that the comparison stimulus is indistinguishable from the standard, thus the probability of correctly identifying the comparison stimulus as being greater in magnitude is just slightly greater than chance. For the case shown in (c), there is very little overlap and thus a very small probability of incorrectly identifying the standard as the larger of the two stimuli. However, there remains a small possibility for error.

formed to a linear function by converting the proportion of times the subjects choose a particular stimulus to z-scores. Tables of z-scores can be found in any introductory book on statistics.

A z-score is the value of the abscissa which corresponds to a particular probability of occurrence (the *proportion* of times a stimulus was chosen) on a "standard normal distribution." A "standard normal distribution" is simply a normal distribution with a mean of zero and standard deviation of one. The interested reader should review properties of discrete probability distributions for a better understanding of the underlying theory.

Once converted to z-scores, a line is fit to the data using the method of least squares. The sigmoidal curve fit results from converting the linear fit back to equivalent proportions. Figure 2-5 shows graphs of the (a) raw and (b) transformed data, along with corresponding curve fits.

By convention the JND is established at the point of 50% recognition. Since typically stimuli both larger and smaller than the standard are tested, there are two JNDs - an upper JND (designated JND^U in Figure 2-5(a)) and a lower JND (designated JND^L in Figure 2-5(a)). For stimuli that are larger than the standard, a proportion of 0.75 (z-score of +0.67), that (as graphed in Figure 2-5(a)) represents the point of 50% recognition. For stimuli that are smaller than the standard, a proportion of 0.25 (z-score of -0.67) represents the point of 50% recognition. Upper and lower JNDs are established as the difference between 0.75 and 0.50, and 0.50 and 0.25 proportions, respectively [Gescheider 1997]. The upper and lower JNDs are often averaged to give one JND value for a particular standard stimulus (as is reported in section 4.4).

The method of constant stimuli is the most accurate of the three methods. It is also preferable because is requires fewer comparison stimuli than the method of limits, though the stimuli must be more carefully chosen. Unfortunately, this method is also the most time consuming. The method of constant stimuli was chosen for the tests described herein due to the method’s general simplicity for administering the tests and applicability for both physical and virtual experiments.

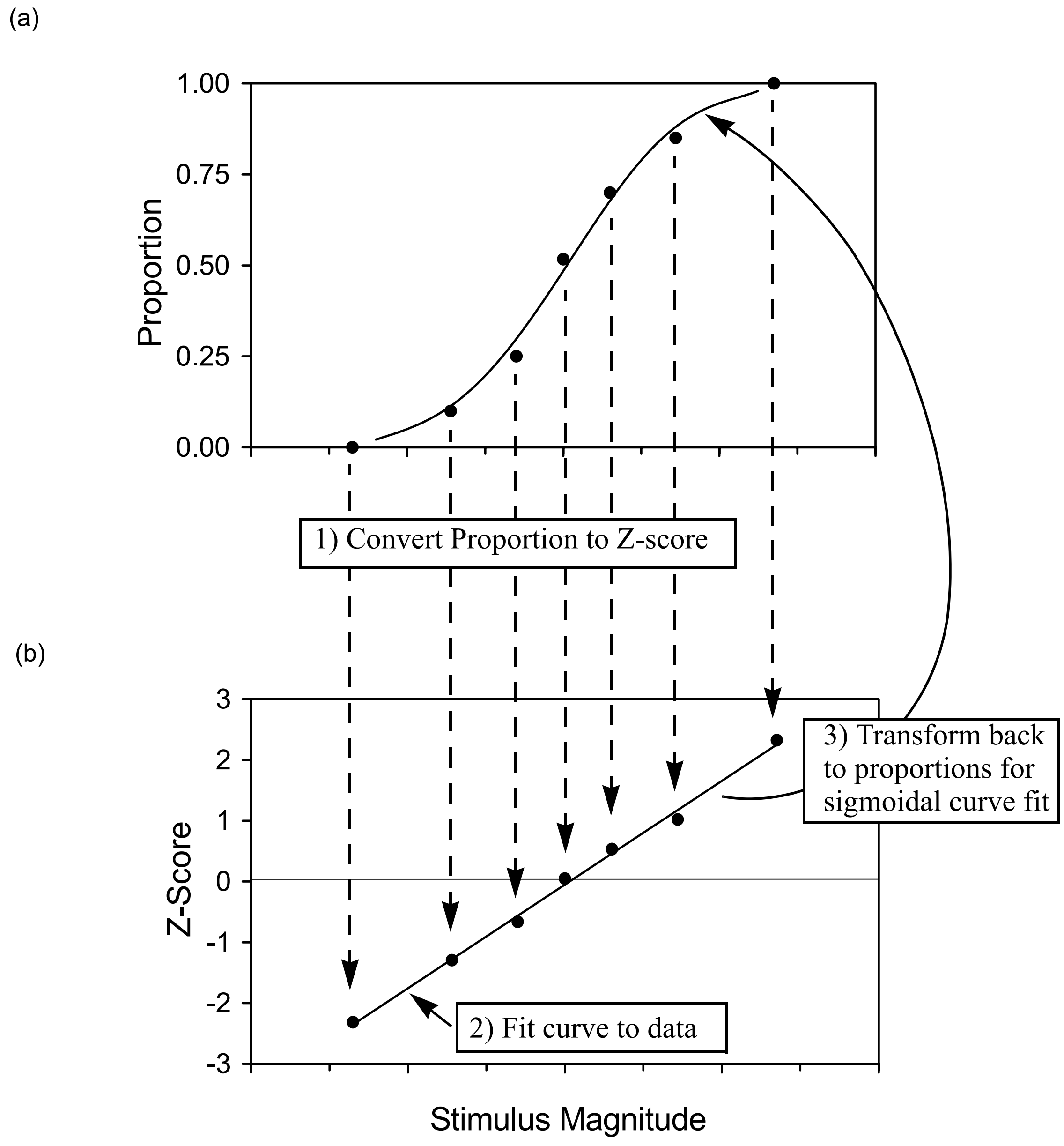

Figure 2-5. Methodology of curve fit for typical data. 1) Sigmoidal curve fit established by converting proportions to z-scores. 2) Once converted to z-scores, a line is fit to the data by the method of least squares (shown in (b)). 3) The sigmoidal curve fit results from converting the linear fit back to equivalent proportions (shown in (a)).

2.2.2.2 Method of Limits

In the method of limits, a series of stimuli are presented to test subjects in an ascending or descending order. To establish a JND, the stimuli are paired with a standard stimulus. Initially, testing begins by presenting stimuli well above or well below the standard, so that it is easily distinguished from the standard. For an ascending series, the value of the comparison stimuli is increased by small increments until it can no longer be distinguished from the standard. After recording this point, testing continues (incrementing the value of the comparison stimuli) until the subject can once again distinguish a difference between the standard and comparison stimuli. This results in a gap over which the subjects can not discern the difference between the two stimuli. The JND is established as half of the width of this gap.

The process is repeated several times for each standard. To help reduce the possibility of habituation (e.g., always choosing the stimulus presented fourth), the series are run in both ascending and descending order for each standard. Each series should also begin at a slightly different comparison value, though care should be taken not to start with a value too far from the standard, as this could extend test time and lead to disinterest and fatigue.

The method of limits is less time consuming and generally more popular than the method of constant stimuli. While it is not as accurate as the method of constant stimuli, it is more accurate than the method of adjustment. However, the large number of comparisons in this method necessitates having a large number of comparison stimuli. This is undesirable if the fabrication of test stimuli is difficult or time consuming. This was not the case for the experiments presented in chapter 4; however, it would have presented a logistical issue to accurately present this many physical stimuli in rapid succession (since the method of constant stimuli requires only seven stimuli per test, these stimuli could easily be fit around the perimeter of the "curvature wheel" (see Figure 4-6), thus simplifying the presentation of stimuli).

2.2.2.3 Method of Adjustment

This method is quite similar to the method of limits; however, in the method of adjustment, the test subjects themselves adjust the value of the comparison stimuli to match the standard. Subjects complete many trials for each standard, and though some scatter in the data is expected, they should nominally cluster around the value of the standard. For this method, a measure of the dispersion of the data, such as its standard deviation, is used as the JND. Precautions similar to those mentioned for the method of limits can be employed to reduce habituation.

Researchers have presented mixed views about this method. Some argue that the extra dimension of control afforded to test subjects can help to reduce boredom and apathy. However, others believe that this can put undue pressure on the test subjects. Furthermore, it must be possible to format the test such that it can be self-administered. The bottom line is that the method can proceed quite rapidly, but is acknowledged to be less accurate than the other two methods.

3 Shape Sensor: A Tactile Sensor for Measuring Local Object Geometry

Dexterous manipulation in humans and in robots requires information about the contact conditions between the fingertips and a grasped object. For example, when rolling an object between the fingertips, the curvature of the object and the locations of contacts on the finger and object surfaces must be known to plan the required finger motions. Other surface properties such as friction and compliance also influence the manipulation strategy. In humans, such information is obtained through a combination visual and tactile sensing and is essential for skillful object handling.

In robots, despite many years of research, the state of the art in tactile sensing and interpretation is comparatively primitive. The challenge of creating a sensate artificial "skin" for robotic hands is formidable. Trade-offs must inevitably be made among spatial resolution, robustness, pressure sensitivity and the ability to comply with irregular or curved surfaces. Providing power and transporting signals along the robot fingers are also difficult, especially when the digits are human-sized or smaller. Nonetheless, many kinds of tactile sensors have been reported in the literature.

The following sections present previous work in tactile sensing, the conceptual approach of the sensor, the sensor design and construction, and the results of simulations and experiments. The chapter concludes with a discussion of the results.

3.1 Previous Work

Numerous examples of tactile sensors exist in the literature. For reviews of the state of the art in robotic tactile sensing see Dario [1991], Lee [2000], Maeno [2002] and Petriu et al. [2002]. However, more specifically we find that others have also made estimates of object curvature and shape as discussed in this chapter. Notably, Fearing and Binford [1991] used

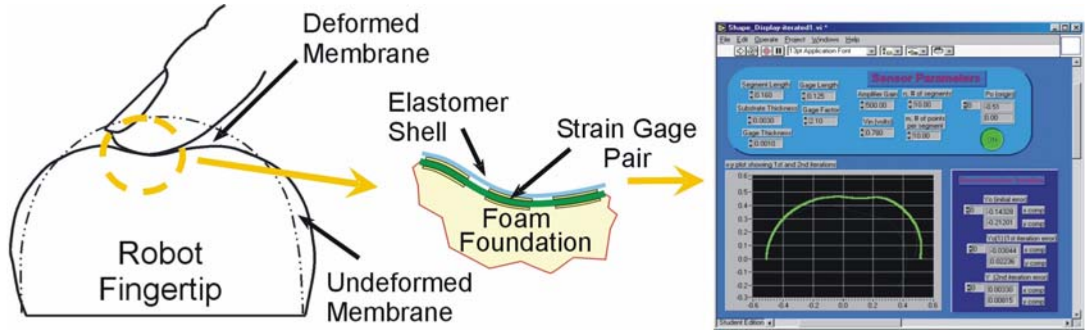

Figure 3-1. Schematic of sensor construction and typical results for a linear sensor prototype.

Hertzian contact models as the basis of their pressure-based estimates. Rucci and Dario [1994] and Canepa et al. [1992], used a piezoresistive tactile array and neural network to measure object curvature. Charlebois et al. [1997] used position estimates from a tactile sensor to estimate local shape.

In most implementations, the tactile sensors consist of an array of pressure or pressure and shear-sensing elements [Fearing and Binford 1991, Chang 1995]. The compliance of these sensors can be tailored but, in general, cannot accommodate large deformations. However, other researchers starting with Brocket [1985] have argued the merits of soft robotic fingertips consisting of a skin covering an inner layer of liquid or foam. With these sensors, it becomes more practical to measure deformations of the skin rather than pressure and shear stress distributions. Nowlin [1991], Russel [1992], and Ferrier and Brocket [2000] present tactile sensors of this type. The salient characteristic of these sensors is that they measure deflections of the skin and, with suitable processing, can provide measurements of local object geometry. Thus, in addition to the practical advantages afforded by soft fingertips [Shimoga and Goldenberg 1996], they provide information that is of direct use for planning dexterous motions with rolling and/or sliding. A difficulty with previous soft-finger designs, however, is that they pose challenging numerical problems to reconstruct the skin geometry from (noisy) sensor readings.

3.2 Sensor Concept

This section describes our general approach for measuring robot fingertip geometry (and by inference, local object geometry) using an array of curvature measuring elements.The sensing approach is compatible with a soft skin covering a layer of foam or fluid

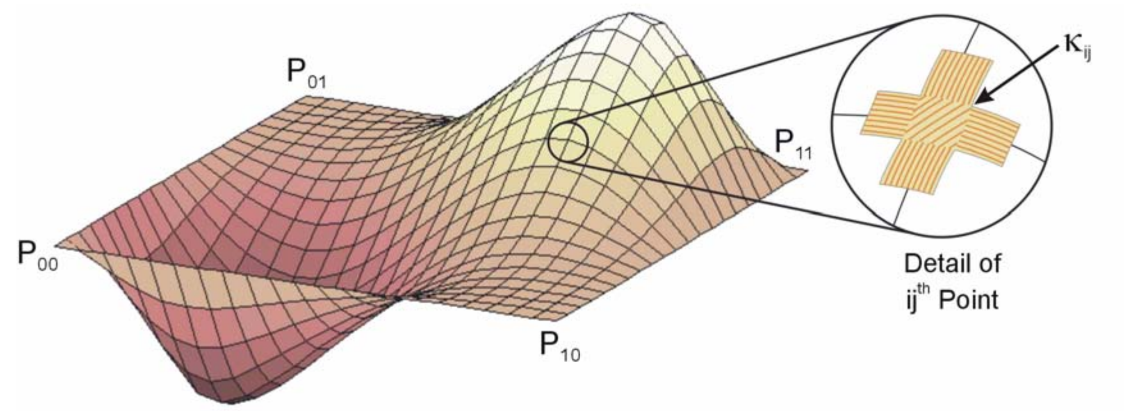

Figure 3-2. General (n x m) parametric surface patch. Detail of local surface shows curvature sensing element κ_{ij} which indicates curvature of the ijth point.

(Figure 3-1) and allows the skin geometry to be reconstructed with a minimum of computation. For measuring local object geometry we consider a curved patch, as shown in Figure 3-2. We measure the surface patch at (n x m) points resulting in an array of curvature information (principal curvatures, κ_{xx}, κ_{yy}, and torsion, κ_{xy}) [Montana 1988].

The shape of the patch is obtained by matching curvatures of the basis functions and satisfying boundary conditions.

3.2.1 Data Fitting Approach

The curved membrane resembles a deforming drum head and its surface can be represented by a two-dimensional Fourier sine series.

$$f = \sum c_{kl} \cdot \sin(k\pi x) \cdot \sin(l\pi y)\text{; for } \quad k = 1\ldots r, l = 1\ldots s \tag{3.1}$$

In this example, the Fourier series is chosen so all terms are identically zero at x = 0 and 1, and y = 0 and 1, corresponding to a square membrane. Similar representations can be used for other shapes[1]. The degree of the Fourier series is indicated by the variables r and s,

---

[1] For example, one could model a circular membrane using polar variables, R and θ.

$$f = \sum C_{kl} \cdot \cos(k\pi R) \cdot \sin(l2\pi\theta) + \sum D_{kl} \cdot \cos(k\pi R) \cdot \cos(l2\pi\theta)\text{;}$$
$$\text{for } \quad k = 1\ldots r, l = 1\ldots s$$

where $f = 0$ for R = 0 and R = 0.5, and for θ = 0 and θ = 1. Thus we have a cosine series for R (from zero to 0.5) and sine/cosine series for θ (which repeats every period).

which are generally equal. And as a two-dimensional series is used, r^2 coefficients are required to describe the sensor surface. Generally, the accuracy of the reconstruction improves by choosing a higher order for the Fourier series, but should not exceed the number of sensor measurements to avoid numerical difficulties.

The curvature measurements, κ_{xx}, κ_{yy} and κ_{xy} are related to the surface deformation by the following equations:

$$\kappa_{xx} = \frac{\partial^2 f}{\partial x^2} \qquad \kappa_{yy} = \frac{\partial^2 f}{\partial y^2} \qquad \kappa_{xy} = \frac{\partial^2 f}{\partial x \partial y} \tag{3.2}$$

The standard least squares procedure is used to solve for the Fourier coefficients. The measurements are represented by the following matrix equation:

$$K = M\,c \tag{3.3}$$

where K is the (N_κ by 1) vector of curvature measurements,

$$K = \begin{bmatrix} \begin{bmatrix} \\ \kappa_{xx} \\ \\ \end{bmatrix} \\ \begin{bmatrix} \\ \kappa_{yy} \\ \\ \end{bmatrix} \\ \begin{bmatrix} \\ \kappa_{xy} \\ \\ \end{bmatrix} \end{bmatrix} = \begin{bmatrix} \kappa_{xx}\big|_{x_1,\,y_1} \\ \kappa_{xx}\big|_{x_1,\,y_2} \\ \ldots \\ \kappa_{xx}\big|_{x_n,\,y_{m-1}} \\ \kappa_{xx}\big|_{x_n,\,y_m} \\ \kappa_{yy}\big|_{x_1,\,y_1} \\ \ldots \\ \kappa_{yy}\big|_{x_n,\,y_m} \\ \kappa_{xy}\big|_{x_1,\,y_1} \\ \ldots \\ \kappa_{xy}\big|_{x_n,\,y_m} \end{bmatrix}$$

M is the (N_κ by N_c) measurement matrix,

$$M = \pi^2 \begin{bmatrix} -\sin(\pi x_1)\cdot\sin(\pi y_1) & -\sin(\pi x_1)\cdot\sin(2\pi y_1) & \dots & -\sin(r\pi x_1)\cdot\sin(s\pi y_1) \\ -\sin(\pi x_1)\cdot\sin(\pi y_2) & -\sin(\pi x_1)\cdot\sin(2\pi y_2) & \dots & -\sin(r\pi x_1)\cdot\sin(s\pi y_2) \\ \vdots & \vdots & \vdots & \vdots \\ -\sin(\pi x_n)\cdot\sin(\pi y_{m-1}) & -\sin(\pi x_n)\cdot\sin(2\pi y_{m-1}) & \dots & -r^2\sin(r\pi x_n)\cdot\sin(s\pi y_{2m-1}) \\ -\sin(\pi x_n)\cdot\sin(\pi y_m) & -\sin(\pi x_n)\cdot\sin(2\pi y_m) & \dots & -r^2\sin(r\pi x_n)\cdot\sin(s\pi y_m) \\ -\sin(\pi x_1)\cdot\sin(\pi y_1) & -4\sin(\pi x_1)\cdot\sin(2\pi y_1) & \dots & -s^2\sin(r\pi x_1)\cdot\sin(s\pi y_1) \\ \vdots & \vdots & \vdots & \vdots \\ -\sin(\pi x_n)\cdot\sin(\pi y_m) & -4\sin(\pi x_n)\cdot\sin(2\pi y_m) & \dots & -s^2\sin(r\pi x_n)\cdot\sin(s\pi y_m) \\ \cos(\pi x_1)\cdot\cos(\pi y_1) & 2\cos(\pi x_1)\cdot\cos(2\pi y_1) & \dots & rs\cos(r\pi x_1)\cdot\cos(s\pi y_1) \\ \vdots & \vdots & \vdots & \vdots \\ \cos(\pi x_n)\cdot\cos(\pi y_m) & 2\cos(\pi x_n)\cdot\cos(2\pi y_m) & \dots & rs\cos(r\pi x_n)\cdot\cos(s\pi y_m) \end{bmatrix}$$

and c is the (N_c by 1) vector of Fourier coefficients.

$$c = \begin{bmatrix} c_{11} \\ c_{12} \\ c_{13} \\ \vdots \\ \vdots \\ c_{r\,s-1} \\ c_{rs} \end{bmatrix}$$

Each row of the measurement matrix, M, represents the basis functions evaluated at the location of a single sensor. This matrix was populated in the order corresponding to sequentially progressing down each row on the physical device, repeating for each of the principle curvatures (i.e., the first n·m rows correspond to κ_{xx} measurements followed by those corresponding to κ_{yy} and κ_{xy}). The K and M arrays were correspondingly populated. The K, M, and c arrays were concatenated in this manner for computation simplicity.

Measurements are taken over an $m \times n$ rectangular grid of points. The total number of measurements is three times the number of grid points ($N_\kappa = 3\cdot m\cdot n$) because three scalar curvature measurements are made at each grid point. The total number of Fourier coefficients, N_c, corresponds to the square of the series order (technically $N_c = r\cdot s$, but realistically, as stated, $r = s$, thus $N_c = r^2$).

The standard least squares procedure gives the following estimate for the Fourier coefficients using the Moore-Penrose left pseudo-inverse:

$$c = (M^T M)^{-1} M^T K \tag{3.4}$$

Note that since the measurement matrix, M, is dependent only on the geometry of the sensor that the quantity $(M^T M)^{-1} M^T = \hat{M}$ can be calculated offline reducing the real time computation of Equation 3.4 to:

$$c = \hat{M} K \tag{3.5}$$

3.3 Sensor Design and Construction

To experimentally validate the sensor concept a simple linear array was constructed. The linear array uses standard photoimaging and flexible circuit fabrication techniques combined with standard strain gage technology. Bending strains, which are proportional to curvature, are isolated using a specialized configuration of strain gages. Details of the design, including design trades, thermal modeling, theory of operation, electronics, and construction are outlined in the following subsections.

3.3.1 Design Trades

As with any device, one must consider a complex space of design trades. The primary trades involved the electrical, thermal, and mechanical design, which influence sensor sensitivity, drift, and compliance. Informal design trades were made in order to maximize sensor performance. The trades were not rigorous because unlike criteria that can be modeled easily, performance was limited by relatively subjective constraints such as manufacturing risk and lead time.

Sensor performance is driven by two primary sources: resolution and membrane compliance. Unfortunately these requirements are in direct conflict. While it is important for the sensor to be highly sensitive, it would be useless if it did not conform to manipulated objects. As one can see from Equation 3.14, measured signals are proportional to sensor thickness. On the other hand, the bending stiffness is proportional to $(\text{thickness})^3$, so even a small addition in sensor thickness drastically reduces its compliance. Ultimately, prototypes were simply made as thin as possible with the commercially available prefabricated strain gages (~175 μm and 100 μm thick, respectively for the first and second-generation prototypes). It was also important for the sensor to be as thin as possible to prevent yielding of the strain gages.

Another consideration in the construction of this sensor is the issue of how one should go about measuring curvature. Strain gages were chosen as they provide a straightforward way to measure bending strains, which are proportional to curvature. The sensor makes use of standard bridge circuitry, from which there are many gage configurations to choose. Of all the possible options, a half-bridge design was chosen. The half-bridge configuration (shown in Figure 3-5) reduces thermal effects and rejects axial strains, which allows bending strains to be isolated (see Fraden [1996] and Appendix A). Both of these properties are essential for this sensor. These characteristics are also common to full-bridge designs; however, with the half-bridge this is accomplished with half as many active gages and in half the amount of space. See Appendix A for more details concerning strain gage circuitry and section 3.3.2 for further discussion of the half-bridge circuitry.

As with many sensors, it is very important to consider thermal issues in the final sensor design, since most sensors are also thermometers. This sensor is no exception. By utilizing a half-bridge as the sensing element, the detrimental effects of temperature fluctuations are partially mitigated. However, the finite thermal resistance associated with the polymer substrate can lead to a temperature differential between paired gages in a half-bridge. This temperature differential creates a slight bridge imbalance that can be interpreted as a false curvature signal. To quantify these effects it is useful to construct a simple thermal model of the sensor, as shown in Figures 3-3 and 3-4.

The thermal model represents a single gage-pair. The model assumes that each gage has a uniform temperature and that its thermal capacitance is small compared to that of the substrate and sensor skin. $R_{sub,X1}$ and $R_{sub,X2}$ represent the through-thickness thermal resistance of the substrate for outboard and inboard gages, respectively. $R_{sub,Y}$ is the thermal resistance for heat dissipation into the polyimide substrate and $C_{sub,Y}$ is the heat capacity of the polyimide substrate. $R_{skin,X1}$ represents the thermal resistance of heat flowing from the outboard strain gage into the silicone skin. $R_{skin,Y}$ is the thermal resistance for heat dissipation into the silicone skin and $C_{skin,Y}$ is the heat capacity of the silicone skin. $R_{skin,X2}$ is the through-thickness thermal resistance of the silicone rubber skin, which is important when the sensor comes in contact with hot or cold objects.

This model is useful when considering environmental conditions that the sensor will encounter during use. Some of the possible scenarios that could lead to a thermally induced bridge imbalance are addressed in section A.2. The largest contributions to thermally induced sensor drift are summarized in Table 3-2. The key conclusions from this thermal modeling is that the sensor should be designed to maximize conductivity through the substrate. A polyimide substrate was used based on availability, which has moderately good conductivity. Furthermore, the sensor should be covered with a protective skin to insulate the sensor from the environment. See Appendix A for a more detailed discussion of thermal issues.

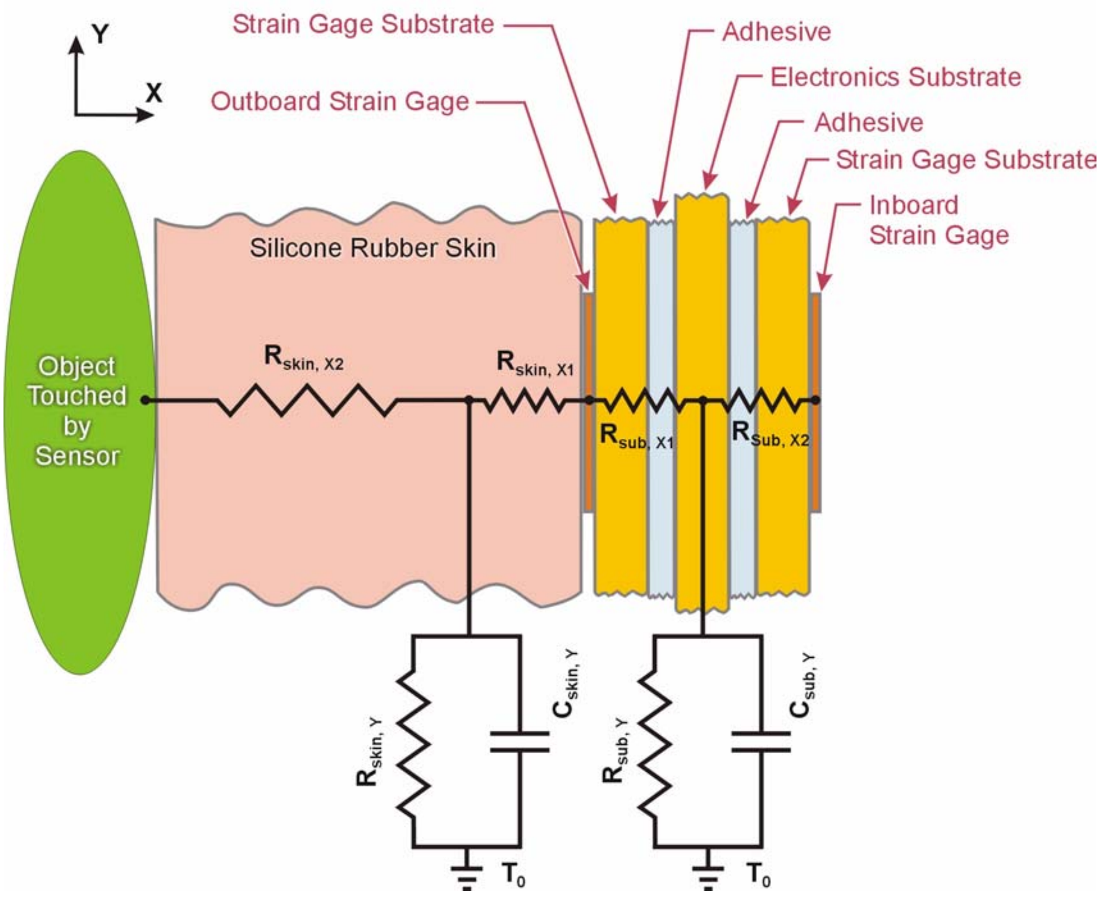

Figure 3-3. Sensor thermal conduction model overlaid on detailed cross-section of the sensor. The model is useful for predicting the operation temperature of the gage elements, as well as for investigating events that could result in a temperature differential between the gages of a half-bridge.

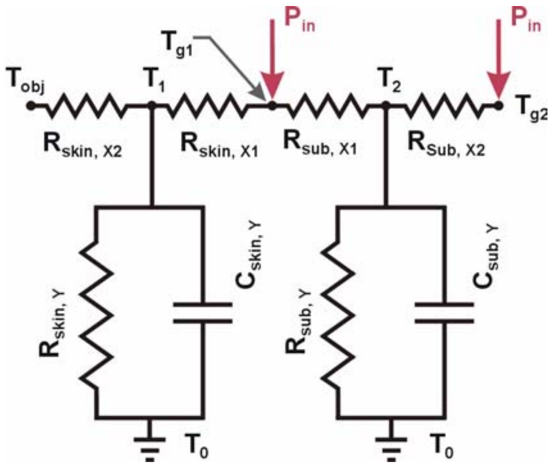

Heat equations for thermal circuit

$$\dot{T}_1 = \frac{1}{C_{skin,Y}}\left[\frac{T_{g1}}{R_{skin,X1}} - \left(\frac{1}{R_{skin,X1}} + \frac{1}{R_{skin,X2}} + \frac{1}{R_{skin,Y}}\right)T_1 + \frac{T_{obj}}{R_{skin,X2}} + \frac{T_0}{R_{skin,Y}}\right]$$

$$\dot{T}_2 = \frac{1}{C_{sub,Y}}\left[\frac{T_{g1}}{R_{sub,X1}} + \frac{T_{g2}}{R_{sub,X2}} - \left(\frac{1}{R_{sub,X1}} + \frac{1}{R_{sub,X2}} + \frac{1}{R_{sub,Y}}\right)T_2 + \frac{T_0}{R_{sub,Y}}\right]$$

Steady state thermal equations

$$T_1 = \frac{\left[\frac{T_{g1}}{R_{skin,X1}} + \frac{T_{obj}}{R_{skin,X2}} + \frac{T_0}{R_{skin,Y}}\right]}{\left(\frac{1}{R_{skin,X1}} + \frac{1}{R_{skin,X2}} + \frac{1}{R_{skin,Y}}\right)} \qquad T_2 = \frac{\left[\frac{T_{g1}}{R_{sub,X1}} + \frac{T_{g2}}{R_{sub,X2}} + \frac{T_0}{R_{sub,Y}}\right]}{\left(\frac{1}{R_{sub,X1}} + \frac{1}{R_{sub,X2}} + \frac{1}{R_{sub,Y}}\right)}$$

Expressions for the gage temperatures

$$T_{g1} = \left[\frac{T_1}{R_{skin,X1}} + \frac{T_2}{R_{sub,X1}} - P_{in}\right]\left(\frac{R_{skin,X1} + R_{sub,X1}}{R_{skin,X1} \cdot R_{sub,X1}}\right) \qquad T_{g2} = T_2 + P_{in} \cdot R_{sub,X2}$$

Figure 3-4. Sensor thermal conduction model. Electrical circuit representation of the sensor thermal model. The thermal equations of motion describe the dynamic behavior of the sensor. T_{g1} and T_{g2} are the temperatures of the outboard and inboard gages, respectively. T_0 is the ambient temperature - also assumed to be the temperature of the sensor base. T_{obj} is the temperature of an object touched by the sensor. $R_{sub,X1}$ and $R_{sub,X2}$ are the through-thickness thermal resistance of the substrate for outboard and inboard gages, respectively. $R_{skin,X1}$ is the thermal resistance of heat flowing from the outboard strain gage to the silicone skin and $R_{sub,Y}$ is the thermal resistance for heat dissipation into the polyimide substrate. $C_{sub,Y}$ is the heat capacity of the polyimide substrate. $R_{skin,X1}$ represents the thermal resistance of heat flowing from the outboard strain gage to the silicone skin and $R_{skin,Y}$ is the thermal resistance for heat dissipation into the silicone skin. $C_{skin,Y}$ is the heat capacity of the silicone skin. $R_{skin,X2}$ is the through-thickness thermal resistance of the silicone rubber skin, which is important when the sensor comes in contact with hot or cold objects.. This value of this resistance is set to infinity when the sensor is not in contact.

Though the conductivity of the polyimide substrate is moderately good, it can not approach the conductivity of graphite or metallic materials. As a result of the limited heat sinking capability of the polyimide substrate, a standard 5-volt bridge excitation will actually melt the strain gages, so a lower excitation voltage must be used. However, lowering the excitation voltage means a direct loss of sensitivity. To be conservative, the excitation voltage was chosen to stay within a modest power dissipation range of 0.50 W/m^2, which is recommended when placing strain gages on a polymer substrate[2]. An excitation voltage of 1.2 volts was adopted, to stay within the allotted power dissipation budget, which limited self-heating of the gages to less than a few degrees. One could also use the thermal model presented herein to optimize the sensor sensitivity.

To minimize manufacturing risks while building the initial sensor prototype, this prototype was produced in halves and subsequently laminated together. This is an example of a design trade that was difficult to quantify initially, and unfortunately resulted in significant degradation of sensor performance due to hysteresis. Sensor resolution is both a function of sensitivity and noise, so it is important to do more than simply maximize Equation 3.14, especially since the hysteresis dwarfed all other sources of noise in the sensor. The hysteresis was mitigated by the new design discussed in section 3.3.4.

3.3.2 Sensor Operational Theory

The sensor utilizes well established strain gage theory to measure the curvature of each element in the linear array. Strain gages are well characterized and known to follow the relationship:

$$\frac{\Delta R}{R_g} = GF \cdot \varepsilon \tag{3.6}$$

where R_g is the gage resistance before strain is applied, ΔR is the change in resistance due to an applied strain, ε is the strain applied to the gage, and *GF* is the gage factor (a material property). As mentioned in the previous section, the sensor utilizes a half-bridge wheatstone bridge configuration. A pair of strain gages placed back-to-back on a flexible substrate correspond to the bridge resistor values, R_1 and R_2, shown in Figure 3-5. As will be shown, it is possible to derive a closed-form solution for each sensor element (gage-pair) which relates the output voltage to the average radius of curvature of the gages (see Equations 3.14 and 3.15). This relationship is a function of the geometry of the sensor as well as the circuitry. To better understand how the geometry relates to the measured strains

---

[2] Source: Georgia Tech AE3145 course notes (www.ae.gatech.edu/%7Eae3145/ae3145/Lab2/strain-gages.html).

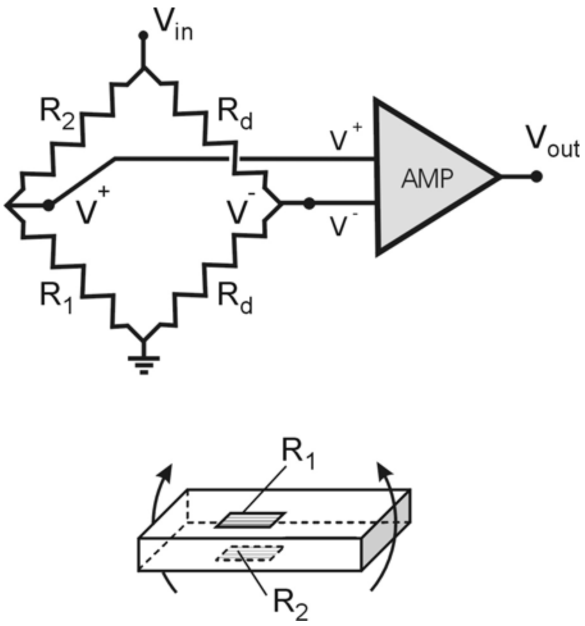

Figure 3-5. Schematic of sensor half-bridge used to measure curvature.

refer to Figure 3-6. Figure 3-6(a) shows a cross-section of the sensor in contact with a circular object of radius, r_{obj}, with relevant dimensions of the substrate and gages given in Figure 3-6(b).

To develop the equation that describes the relationship between bending strain and curvature, consider the strains experienced by a single gage-pair as shown in Figure 3-6(c). As a result of the symmetric sensor construction, the mid-line of the substrate is coincident with the neutral axis and is therefore inextensional. Making use of this fact, it is possible to directly relate the radius of curvature of the substrate, r_{ave}, to the original length of the strain gage, L_0 ($L_0 = L_g$, the gage length). Assuming a constant curvature in the localized area of the gage-pair, gives the relationship:

$$s = r_{ave} \cdot \theta \tag{3.7}$$

where s is the arc-length and θ is the angle inscribed by that arc length. However, since the substrate mid-line is inextensional, the portion of the substrate corresponding to the length of each strain gage is always equal to L_0. Therefore, the inscribed angle for that portion of the sensor is simply:

$$\theta = \frac{L_0}{r_{ave}} \tag{3.8}$$

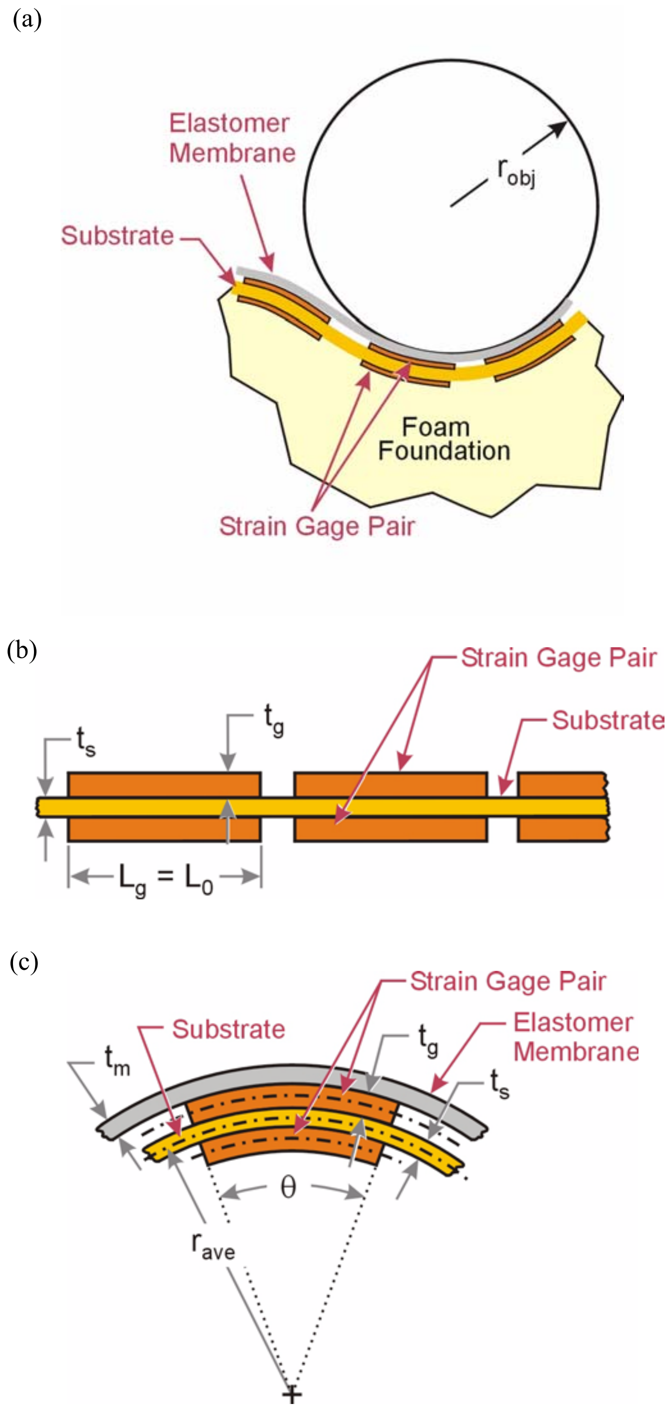

Figure 3-6. (a) Cross-sectional view of sensor pressed against an object of radius, r_{obj}. (b) Relevant dimensions of the sensor substrate and strain gages viewed with sensor array flattened and in cross-section. (c) The radius of curve is measured and computed at the mid-line of the substrate, r_{ave}, which can be related to the radius of curvature of the object, r_{obj}, by accounting for the substrate, gage, and membrane thicknesses, t_s, t_g , and t_m , respectively.

A modified version of Equation 3.7 can also be used to express the current length, L, of the mid-line of the upper strain gage (in tension), by making a small correction to the radius:

$$L = \left(r_{ave} + \frac{t_s + t_g}{2}\right) \cdot \theta \tag{3.9}$$

where t_g and t_s are the gage and substrate thicknesses, respectively. Combining Equations 3.8 and 3.9, gives a formula for the current gage length expressed in terms of a single unknown, r_{ave}.

$$L = \left(r_{ave} + \frac{t_s + t_g}{2}\right) \cdot \frac{L_0}{r_{ave}} \tag{3.10}$$

The length of the bottom strain gage can be calculated in a similar fashion.

The next step is to compute the strain experienced by the strain gages. The formula for the engineering strain is:

$$\varepsilon = \frac{L - L_0}{L_0} \tag{3.11}$$

As expressed earlier, L and L_0 are the current and undeformed lengths of a strain gage element, respectively. Substituting the result from Equation 3.10 into Equation 3.11, gives the strain in the upper strain gage, expressed as a function of the substrate radius.

$$\varepsilon = \frac{\left(r_{ave} + \frac{t_s + t_g}{2}\right) \cdot \frac{L_0}{r_{ave}} - L_0}{L_0} = \frac{t_s + t_g}{2\ r_{ave}} \tag{3.12}$$

The strain in the bottom strain gage is equal and opposite to that shown in Equation 3.12 (from sensor symmetry). Solving for the change in resistance which accompanies bending induced strain is now simply a matter of combining Equations 3.6 and 3.12.

$$\Delta R = \frac{R_g\ GF\ (t_s + t_g)}{2\ r_{ave}} \tag{3.13}$$

Substituting Equation 3.13 into a standard wheatstone bridge formulation (see Appendix A: Equations A.3 and A.4) yields the final bridge equation for measuring bending strains with a pair of back-to-back gages wired in a half-bridge configuration (as shown in Figure 3-5).

$$V_{out} = \frac{V_{in} \cdot GF \cdot (t_s + t_g) \cdot Gain}{4r_{ave}} \tag{3.14}$$

where V_{in} is the bridge excitation voltage, r_{ave} is the curvature of the membrane centerline, t_s is the thickness of the membrane substrate, t_g is the gage thickness and “Gain” is the bridge amplification. Equation 3.14 can be rearranged in terms of average curvature, κ, where curvature can be shown as the reciprocal of radius of curvature and $\kappa(i)$ represents the curvature of the i^{th} gage-pair.

$$\kappa(i) = \frac{1}{r_{ave}} = \frac{4V_{out}}{V_{in} \cdot GF \cdot (t_s + t_g) \cdot Gain} \tag{3.15}$$

The sensor was designed to stay within the elastic limits of the metal foil strain gages (about 1% strain for constantan alloy).

3.3.3 Sensor Electronics

The sensor electronics are comprised of the multiplexed (Analog Devices, ADG506) strain gage half-bridges balanced by a dummy half-bridge and amplified by a commercial instrumentation amplifier (Analog Devices, AD620). The amplifier output was filtered by a 60 Hz low-pass filter. As indicated on the schematic in Figure 3-7, R_d is the resistance of the bridge dummy resistor, R_g is the resistance of the active gages, and V_{bal} is the nominal voltage of the dummy half-bridge required to balance the circuit. The dummy half-bridge consists of 1% 10KΩ surface mount resistors. The bridge excitation voltage is generated by a reference diode (LM4051) that is run through a buffer (AD8009) to provide the required current.

The component values chosen for the prototype resulted in an average sensitivity[3] of the gage-pairs of 126 mV/m^{-1}. This means that a one bit increment on the A/D converter represents a change in curvature of $\Delta\kappa = 0.039\ m^{-1}$ (for 12-bit A/D conversion with measurement range of ±10 volts). For reference, if the sensor were in contact with a 3 cm radius cylinder, adding one bit of noise would result in an interpretted radius of 2.996 cm. Therefore, one bit represents a very small increment of curvature.

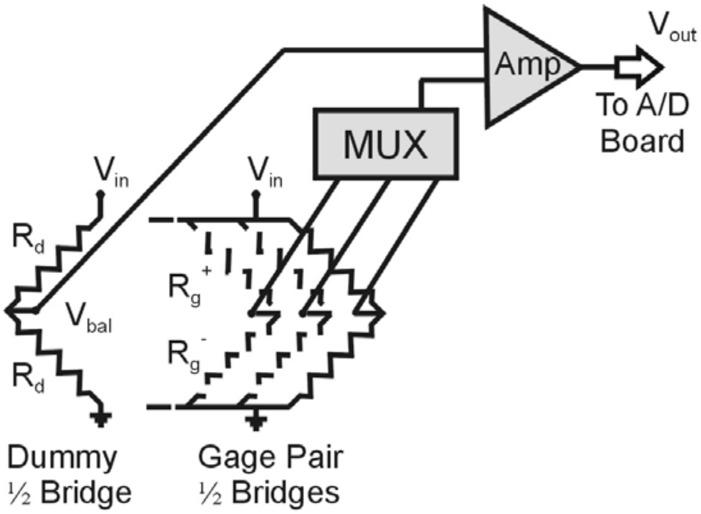

Figure 3-7. Sensor array electrical schematic.

---

[3] The calculated sensitivity of 126 mV/m^{-1} represents an average across all gage-pairs after calibration. See section 3.5.2.1 for an accounting of the sensitivity calculated for individual gage-pairs.

The ultimate resolution of the sensor is both a function of the sensitivity and noise.

$$Resolution = \frac{Noise}{Sensitivity} \tag{3.16}$$

To compute the theoretical resolution of the sensor, an estimate of the sensor noise is required. Table 3-1 lists the individual contributions to RMS electrical measurement noise in the sensor. Sensor drift is treated as a separate source of noise. An estimate of drift is calculated at the full-scale 1.0% strain level (the yield strain of the gages) over a 20°C operating range (see section A.2.1.3 for details). Unlike RMS electrical noise, which generally has a zero mean and is Gaussian in nature, drift directly affects the gain of the sensor and, therefore, also its sensitivity. This source of noise can be very large in comparison to the RMS noise, as shown in the worst case estimate shown in Table 3-2. This drift can be partially compensated for by using local temperature sensing and/or thermal modelling. However, without compensating for temperature changes, the guaranteed resolution over the 20°C, full-scale range is only 0.387 m^{-1}. This is based on the additive effects of drift and noise that are provided in Tables 3-1 and 3-2. On the other hand, if the sensor were temperature compensated or operated in a narrow temperature range around room temperature (as is the case for the experiments conducted herein), then the theoretical resolution of the sensor is 0.041 m^{-1}. Coincidentally, this is slightly more than one bit on the A/D converter.

Table 3-1. Sources of electrical noise in sensor measurements. Both pre- and post- amplification sources of electrical noise are given. The pre-amplification noise is combined and this resultant is amplified as reported. Note that the dominant noise sources are from the reference diode used to generate the bridge excitation voltage and A/D conversion.

	Noise density	Filtered RMS Noise[a]	Filtered Post-Amplifier Noise[a,b]
Pre-amplification Noise Source			
Reference diode (bridge excitation)	see data sheet[c]	1.7 µV	
Buffer for excitation voltage	1.9 nV/$\sqrt{Hz}$	14.7 nV	
Resistor Johnson noise[d]	12.9 nV/$\sqrt{Hz}$	99.7 nV	
	Total RMS	1.81 µV	1.60 mV
Post-amplification Noise Source			
Instrumentation amplifier	9.0 nV/$\sqrt{Hz}$		69.7 nV
Analog-to-digital conversion			3.46 mV[e]
		Total RMS	5.12 ,mV

---

a. Amplifier output filtered through a 60 Hz low-pass filter.

b. The instrumentation amplifier has calculated gain of approximately 880.

c. LM4051 data sheet gives a plot of the noise spectral density

d. The formula for resistor Johnson noise is $\sqrt{4kRT}$, where k is Boltzman's constant ($k = 1.38 \times 10^{-23}$), R is the resistor value, and T is the temperature in Kelvin. Only the largest contribution of Johnson noise is reported, which comes from10KΩ resistors in the dummy half-bridge.

e. Source: National Instruments product manual

Table 3-2. Major sources of sensor drift. Drift primarily affects the sensor gain and therefore the sensor accuracy. Estimates for sensor drift are based on a 1% strain level in the gages and a 20°C drop in operating temperature.

Source of Drift[a]		Percent Change in Gain	Full-Scale Noise[b]
Pre-amplification Noise Source			
Reference diode (bridge excitation)		-0.033%	3.05 mV
Amplifier drift (AD620B)		-0.18%[c]	~20 µV[d] + 16.6 mV[c]
Gage factor		-0.26%	24.02 mV
	Total	-0.473%	43.7 mV

---

a. Only primary sources of drift are reported here. See section A.2.1.3 for more detailed discussion.

b. Full-scale noise is based on either 1% strain and/or 20°C drop in temperature, as applicable.

c. Due to gain resistor drift

d. Source: AD620 data sheet.

3.3.4 Sensor Construction

A custom fabricated flex circuit serves as the substrate supporting the array of gages and routing their associated interconnects. To mitigate the risk of possible fabrication difficulties, the first prototype array was built in halves. Commercially available strain gage arrays (Measurements Group, EA-06-125MW-120) were bonded to single-sided custom-fabricated polyimide (DuPont Pyralux 1 oz. copper clad Kapton^{TM} laminate) flex circuits. The pattern was created using standard contact print photo-imaging techniques. The polyimide laminate was dip-coated with positive photoresist (Injectorall Electronics Corp.) and developed with diluted Sodium Hydroxide (NaOH). Electrical junctions between the flex circuit and strain gages were made using solder paste and 13 μm thick copper foil to maintain a thin sensor profile. The two halves were bonded together using acrylic pressure sensitive (film) adhesive (PSA) (as shown in Figure 3-8(a)). The second-generation prototype, shown in Figures 3-8(b), 3-9 and 3-10, was fabricated with strain gages are bonded directly to a two-sided flex circuit of 25 μm polyimide clad with 35 μm thick copper on both sides. In addition, the second-generation prototype includes local multiplexing, amplification and

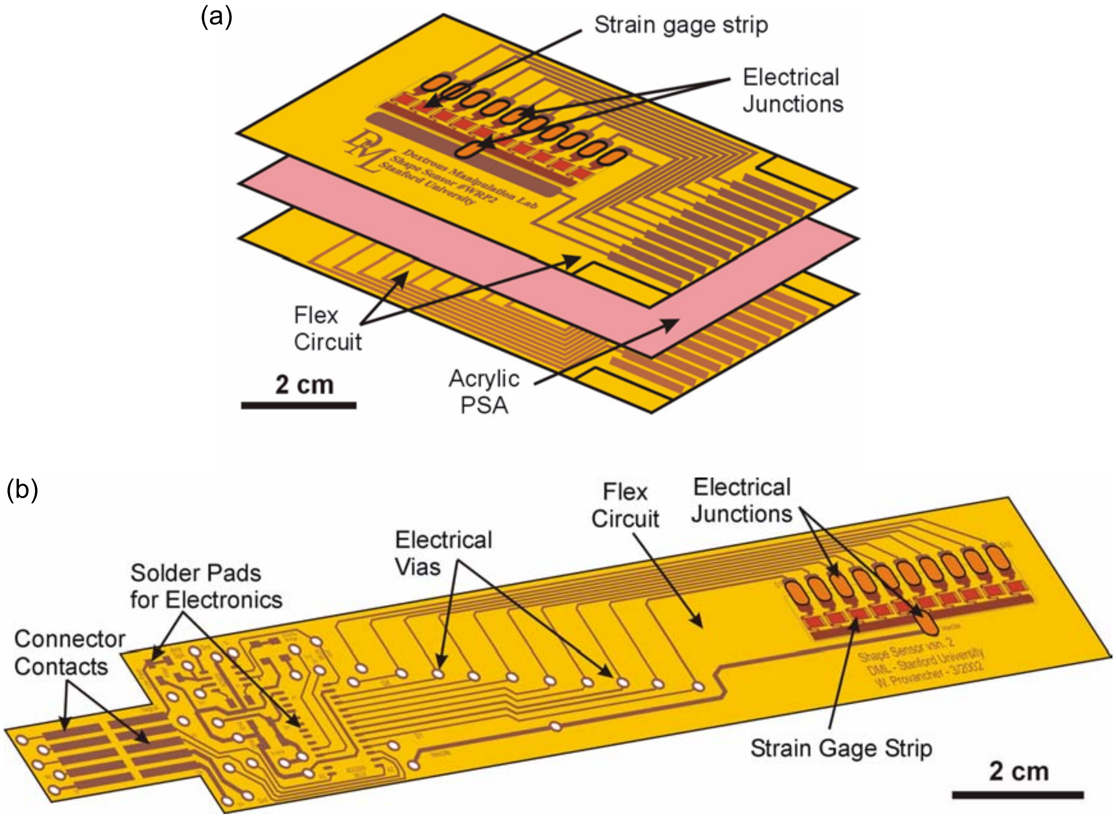

Figure 3-8. Sensor array construction for the (a) first- and (b) second-generation prototypes.

signal conditioning using surface mount devices on the same flexible circuit that supports the strain gages. Eliminating the center layer of acrylic adhesive dramatically reduced sensor hysteresis. Through-thickness electrical connections (vias) were provided by crimping and soldering small (0.062 inch diameter) metallic eyelets (purchased from Keystone Electronics) on either side of the substrate.

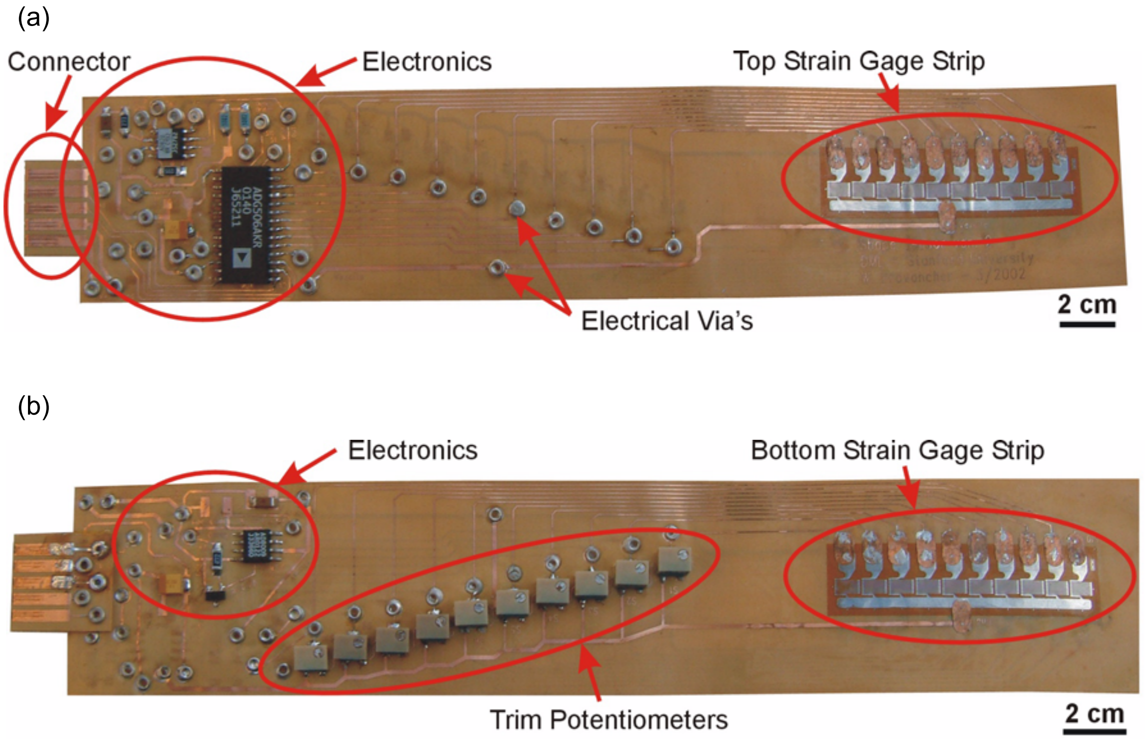

Figure 3-9. Second generation sensor prototype. (a) Top and (b) bottom of two-sided flex circuit are shown.

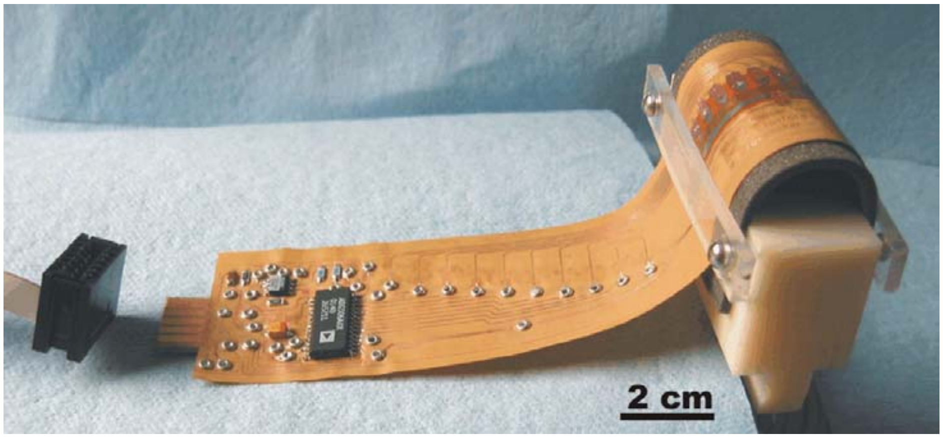

Figure 3-10. Second generation sensor shown as it would be packaged at the fingertip of a telerobot.

3.4 Simulation

Numerical simulation was conducted with two goals in mind: (1) to determine the effects in position space of fitting to a surface in curvature space, and (2) to characterize the effects of sensor noise on reconstruction. To make this evaluation, surface reconstructions made from simulated data were compared to a reference surface. The reference surface was generated using standard thin plate formulations. Simulated curvature data were manufactured by adding random noise to the differentiated surface function of the "perfect" reference surface. The data fitting approach was tested for a general surface as well as the one-dimensional configuration of the linear array sensor prototype.

3.4.1 Two-Dimensional Simulation of Surface

The fitting routine was tested for a general surface as depicted in Figure 3-2 and represented by the basis functions of Equation 3.1. The Fourier coefficients of the basis functions were solved based on simulated curvature measurements using the Moore-Penrose left pseudo-inverse (Equation 3.4).

3.4.1.1 Two-Dimensional Reference Surface

The first step in validation is to generate a reference surface chosen to approximate some expected load. A reference surface was generated using published solutions for thin plate deformations. It is convenient if this reference surface can be approximated by a continuous function *f(x,y)* that permits direct calculation of simulated curvature data (κ_{xx}, κ_{yy} and κ_{xy}). Timoshenko and Gere (1961) present such a solution for deformations of a thin plate due to an arbitrary point load. The solution in Equation 3.17, which describes the displacements in the z-direction as a function of x and y, is represented as a two-dimensional Fourier sine series similar to that shown in Equation 3.1 for the basis functions:

$$w = \sum a_{ij} \cdot \sin(i\pi x) \cdot \sin(j\pi y) \tag{3.17}$$

$$\text{where } a_{ij} = \frac{4 \cdot Q \cdot \sin(i\pi\xi) \cdot \sin(j\pi\eta)}{D\pi^4(i^2 + j^2)^2}$$

ξ, η are the x, y coordinates of load Q

D is the flexural rigidity of the plate, $D = E \cdot h^3 / [12(1 + \upsilon^2)]$

E is Young's Modulus, h is the plate thickness, ν is Poison's ratio

More complex load cases can be represented through superposition of several point loads.

For simulation, three load cases were considered: (1) a centered point load ($\xi = 0.5$, $\eta = 0.5$), (2) an off-center point load ($\xi = 0.2$, $\eta = 0.8$), and (3) a skewed line load (from $\xi = 0.1$, $\eta = 0.9$ to $\xi = 0.9$, $\eta = 0.1$). Simulated curvature data were produced by taking appropriate derivatives of the reference surface displacement function. To simulate the effects of sensor noise on the reconstruction, random noise, with RMS value of $\Delta\kappa = 0.23\ \mathrm{m}^{-1}$ (approximately 25% of the average curvature values) and a maximum value of $\Delta\kappa = 0.40\ \mathrm{m}^{-1}$, was added to the simulated curvature data. The basis functions were fit directly to the simulated curvature data. The "truth" model for the two-dimensional surface was represented by a two-dimensional (15×15) Fourier series. There were 100 measurement points (10×10) with three measurements at each point for a total of 300 measurements. The fitted model had 64 parameters (8×8) Fourier coefficients. An eighth order series was chosen because it is a realistic size for real time computation.

3.4.1.2 Two-Dimensional Simulation Results

The quality of data fitting was quantified by recording the maximum calculated displacement, w_{Max}, at the point of load application and the distributed RMS error, $E_{w,RMS}$, relative to the reference surface. The first metric was chosen because of its significance to manipulation kinematics. During manipulation, the point of load application is the same as the object contact point and small deformations at the robot fingertip ultimately affect the precision of fine manipulations. Table 3-3 reports the maximum calculated displacement at the point of load application, w_{Max}, the absolute error of this displacement, $E_{w,Max}$, and the RMS error for the entire surface, $E_{w,RMS}$, as compared to the reference surface. Figure 3-11 shows mesh plots of two-dimensional simulation results.

(a) Centered Point Load

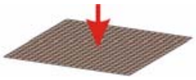

Reference Surface

Curve Fit (with noise)

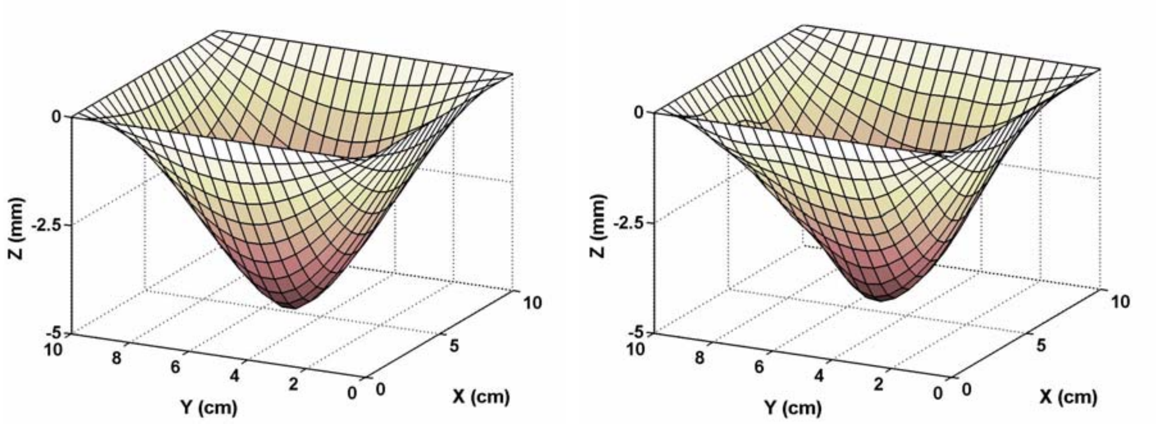

(b) Off-center Point Load

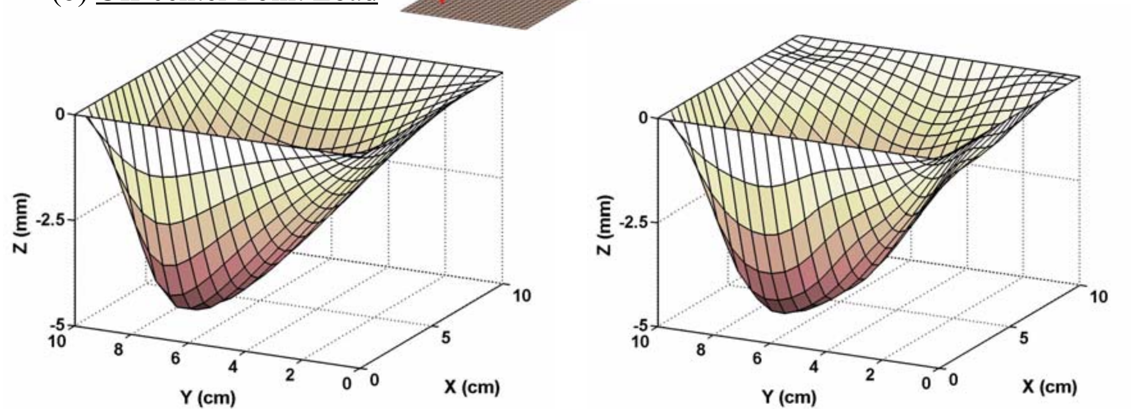

(c) Skewed Line Load

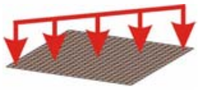

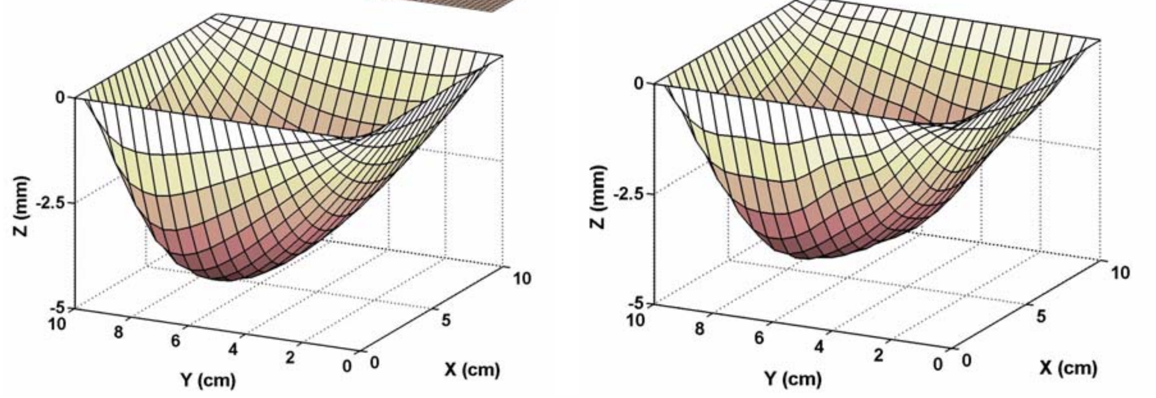

Figure 3-11. Mesh plots for various load cases. For each load case, the reference surface is shown on the left and the surface fit to data with simulated noise is shown on the right. The load cases presented are: (a) *Centered Point Load,* (b) *Off-center point load,* and (c) *Skewed line load.* The reference surface for each load case was generated using a 15th order Fourier sine series (see Timoshenko & Gere 1961). See Table 3-3 for numerical results.

Table 3-3. Simulation results for a 10 cm x 10 cm surface patch with a 10 x 10 array of curvature measuring elements subjected to various load conditions

Load Case	Maximum Displacement			Error	RMS Error
	$w_{Applied}$ [mm]		w_{Max} [mm]	$E_{w,Max}$ [mm]	$E_{w,RMS}$ [mm]
Centered Point Load ($\xi = 0.5, \eta = 0.5$)	4.70	(no noise)	4.59	-0.11	0.067
		(w/ noise)	4.58	-0.12	0.083
Off-center Point Load ($\xi = 0.2, \eta = 0.8$)	4.89	(no noise)	4.58	-0.31	0.316
		(w/ noise)	4.56	-0.34	0.317
Skewed Line Load ($\xi = 0.1, \eta = 0.9$ to $\xi = 0.9, \eta = 0.1$)	4.68	(no noise)	4.63	-0.05	0.193
		(w/ noise)	4.62	-0.06	0.191

3.4.2 One-Dimensional Simulation of Planar Curve

The fitting routine was also tested on the specific geometry of the sensor prototype (assumed to be a planar curve). The sensor membrane was modeled as a curved semi-circular beam of radius, $R_0 = 12.9$ mm. The procedure for fitting a planar curve is the same as that described earlier for the surface; however, the basis functions are simply a one-dimensional Fourier sine series.

$$f = \sum c_i \cdot \sin(i\pi\theta) \text{; for } i = 1\ldots r \tag{3.18}$$

With the planar curve, only in-plane curvature, κ_θ, is measured. The curvature of a planar curve with non-zero initial curvature is slightly more complex.

$$\kappa_\theta \approx \frac{1}{R_0^2} \cdot \frac{\partial^2 u}{\partial \theta^2} + \frac{1}{R_0} u \tag{3.19}$$

3.4.2.1 One-Dimensional Reference Surface

Radial deflections, *u*, of the reference curve representing the sensor membrane were calculated using a standard Rayleigh-Ritz approximation (in polar coordinates) for an inextensional center-loaded curved beam.

$$u = a_0(\sin(\theta) + 3 \cdot \cos(\theta)) \text{; for } \theta = 0\ldots\pi \tag{3.20}$$

where $$a_0 = \frac{-Q \cdot R_0^{\,3}}{72\pi \cdot EI}$$

The "truth" model for the one-dimensional curve was represented by Equation 3.20. There were 10 "sensor" locations with one curvature measurement at each location so there were a total of 10 data points. The fitted model had 8 parameters (8 Fourier coefficients).

As reported for the surface, the quality of data fitting, for the planar curve was quantified by recording both the maximum calculated displacement, u_{Max}, (and error, $E_{u,Max}$) at the point of load application and distributed RMS error, $E_{u,RMS}$, relative to the reference curve. Results of simulation are shown in Table 3-4 and Figure 3-12.

3.4.2.2 One-Dimensional Simulation Results

Simulation was limited to a single load case, a centered line load as indicated, "**Q**", by the arrows shown in respective plots in Figure 3-12. This load case was repeated at three load magnitudes and was chosen for comparison to experimental results. These results are also tabulated in Table 3-4.

Table 3-4. Simulation results for a center loaded inextensional curved beam with a 10 x 1 array of curvature measuring elements with 12.9 mm radius.[a]

Load Case	Maximum Displacement			Error	RMS Error
	$u_{Applied}$ [mm]		u_{Max} [mm]	$E_{u,Max}$ [mm]	$E_{u,RMS}$ [mm]
Centered Line Load	.64	(no noise)	0.64	0	0
		(w/ noise)	0.69	0.06	0.178
	1.27	(no noise)	1.27	0	0
		(w/ noise)	1.37	0.10	0.160
	1.90	(no noise)	1.90	0	0
		(w/ noise)	1.83	-0.07	0.115

---

a. Sensor noise was simulated as an additive random source with RMS value of $\Delta\kappa \approx 4.5\ \mathrm{m}^{-1}$ (approximately 90% of the average curvature value of the $u_{Applied} = 0.63$ mm load case) and maximum value of $\Delta\kappa \approx 8.2\ \mathrm{m}^{-1}$.

(a) Centered Line Load ($\mathbf{u}_{\mathbf{Applied}} = 0.64$ mm)

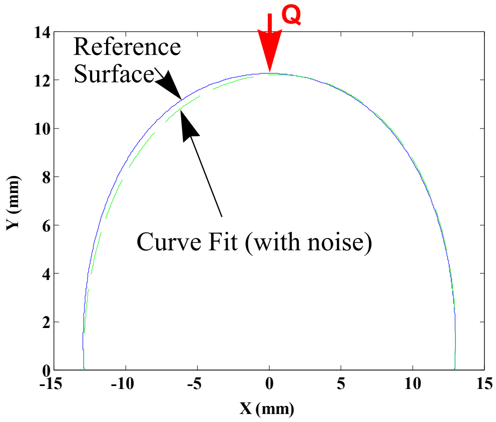

(b) Centered Line Load ($\mathbf{u}_{\mathbf{Applied}} = 1.27$ mm)

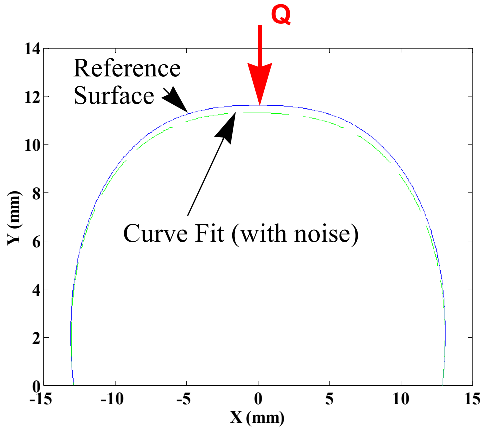

(c) Centered Line Load ($\mathbf{u}_{\mathbf{Applied}} = 1.90$ mm)

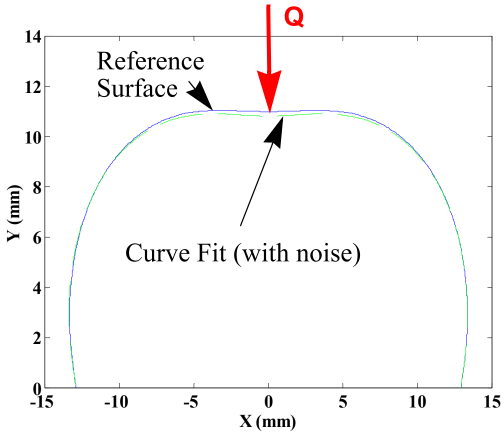

Figure 3-12. Line plots for a centered loaded inextensional curved beam. Results are presented for increasing magnitude of center deflection. Reference curves are shown with the solid line while the curve fit to data with simulated noise is indicated with the dashed line in each graph.

3.4.3 Discussion of Simulation Results

The numerical simulation results show that a series of discrete curvature measurements can be used to create a reasonably accurate reconstruction of the deformed membrane. When moderate levels of noise are added, the maximum position error increases to as much as 10% for moderate deflections. Since it is difficult to predict the RMS noise of actual sensor data without extensive characterization, random noise was introduced to the simulation at the same order of magnitude as the widest "hysteresis gap" presented in Figure 3-13, in the next section. The accuracy of the surface reconstruction improves and the sensitivity to sensor noise rapidly decreases as the number of sensors increases. Of course, increasing the number of sensors also increases the difficulty in manufacturing and the computation time.

3.5 Experimental Validation

This section presents results of the sensor calibration and testing. The following sub-sections present the experimental procedure and a discussion of the results.

3.5.1 Experimental Procedure

3.5.1.1 Calibration and Hysteresis Testing

To confirm proper sensor operation before embedding in a robot fingertip, the sensor was calibrated against cylindrical objects of known curvature. One would expect the sensor output to be directly proportional to object curvature. This was confirmed for objects with small curvature.

Testing of a first-generation sensor revealed hysteresis, which was traced to creep in the acrylic film adhesive. To quantify the hysteresis, measurements were made against a sequence of objects of known curvature, as shown in Figure 3-13(a). Data were recorded starting with objects of large radius of curvature (small curvature) and progressing to objects of decreasing radius of curvature and back again to objects of larger radius of curvature. The sensor was then flipped over and measurements of objects were made with the opposite face of the sensor in contact with the objects, again starting with large objects and progressing as described above. This procedure was carried out to form one complete hysteresis loop. Each gage-pair of the sensor was calibrated over the range of measurements taken during the above procedure. Calibration consisted of standard least-squares fitting of curvature data.

3.5.1.2 Centered Line Load Test

A simple test configuration was chosen to validate the sensor concept experimentally. The sensor was tested as it would be used on a cylindrical robot fingertip (Figure 3-10). A centered line load was applied to the sensor, indicated as "**Q**" in Figure 3-14. For this type of loading, the sensor deforms as a curved beam of radius, $R_0 = 12.9$ mm.

For practicality, instead of applying a line load, a known line-deflection was applied to the center of the sensor using a height gauge. The applied center deflection, u_{Max}, of the sensor was recorded for three discrete load cases of increasing magnitude ($u_{Applied} = 0.64$ mm, 1.27 mm and 1.90 mm). Only one measurement per gage-pair was taken during testing. These discrete curvature signals were utilized to reconstructed the deformed shape of the sensor, as described previously. The quality of data fitting for the experiments was quantified by comparing the maximum calculated displacement, u_{Max}, at the point of load application with the applied deflection. The reconstructed sensor shape is also compared to the shape expected from standard solutions. There were ten curvature measurements, one at each of ten data points.

3.5.2 Experimental Results and Discussion

3.5.2.1 Calibration and Hysteresis Testing

The second-generation prototype (shown in Figures 3-9 and 3-10) was characterized and calibrated as described in section 3.5.1.1. Data were recorded at each gage-pair at each step through the calibration procedure. Sensor data were collected to complete one hysteresis loop. The second generation of the shape sensor represents a three-fold improvement over the first generation design, though significant hysteresis persists (as shown in Figure 3-13).

Figure 3-13(a) shows data for each gage-pair on the sensor in a different color. Note that there are slight variations between the behavior of individual gage-pairs; however, they all bear resemblance to one another, having similar slope and shape. Figure 3-13(b) shows calibration from a single gage-pair, while Figure 3-13(c) shows calibration data averaged across all gage-pairs in the sensor. Both of these graphs show the formation of a small hysteresis loop. The widest hysteresis gap exists for positive curvature measurements, $\Delta\kappa_{\text{Max, hysteresis}} \approx 7\ \text{m}^{-1}$. There is also significant non-linearity in the curves shown in Figure 3-13(a), with a value of $\Delta\kappa_{\text{Max, non-linearity}} \approx 12\ \text{m}^{-1}$ at extreme positive curvatures. Linearity was measured as the distance between the edge of the hysteresis loop and the vertical intersection with a line of slope equal to one that intersects the origin (this line represents the ideal sensor output). A careful examination of the hysteresis in Figure 3-13 gives some indication that the sensor is more repeatable for negative curvature readings. This may be the result of inhomogeneous bonding of strain gages to the substrate.

The hysteresis and non-linearity shown in these graphs is over two orders of magnitude greater than the theoretical resolution, 0.041 m^{-1}. So what could be responsible for this amount of error? It is unlikely that this is related to RMS electrical noise, measured to be less than 10 mV. One source of information that could shed light on this question is the calibration data of the gage-pairs themselves. The calibration data will be discussed in some detail before returning to the issue of sensor hysteresis.

There is considerable variation between the calibrated sensitivity of the gage-pairs, ranging from 0.0818 m^{-1} to 0.1520 m^{-1}, with a mean and standard deviation of 0.1264 m^{-1} and 0.0231 m^{-1}, respectively. There are two plausible explanations for these variations, both of which are related to the bonding conditions between the gages and the substrate.

Variations in bond thickness could explain the difference in the observed sensitivity. A thicker bond-line will increase the separation between the gages and therefore increase the sensitivity of the sensor. If the gage-pair with the lowest sensitivity had a bond-line thickness of 12 μm, then the one with the highest sensitivity would have bond-line thicknesses of 55 μm (refer to Equation 3.15). This is quite reasonable and could easily explain the variation in sensitivity between the gage-pairs, but it does not explain the observed sensor hysteresis.

(a)

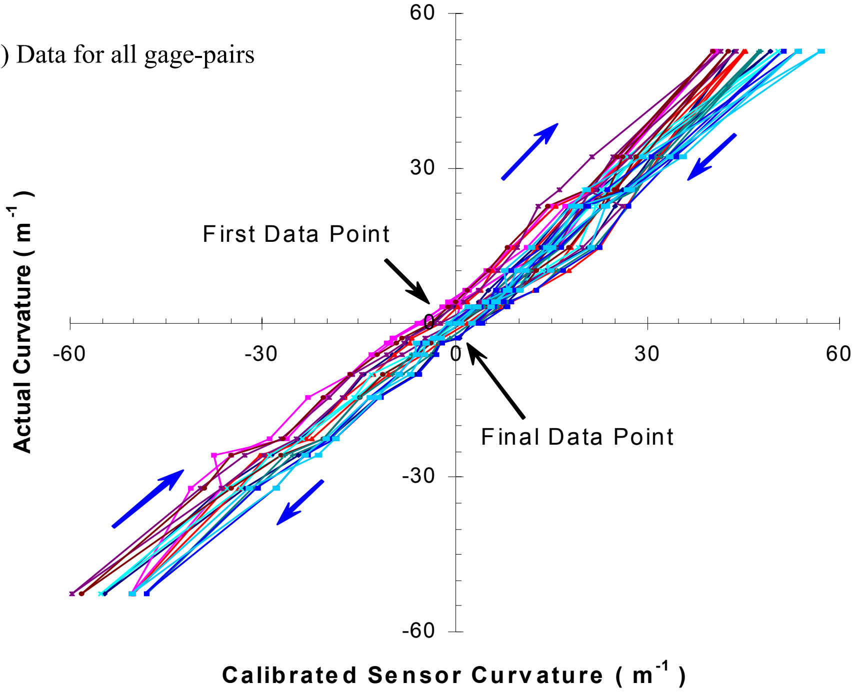
(b) Data for all gage-pairs

(c) Data for single gage-pair

(d) Averaged data for all gage-pairs

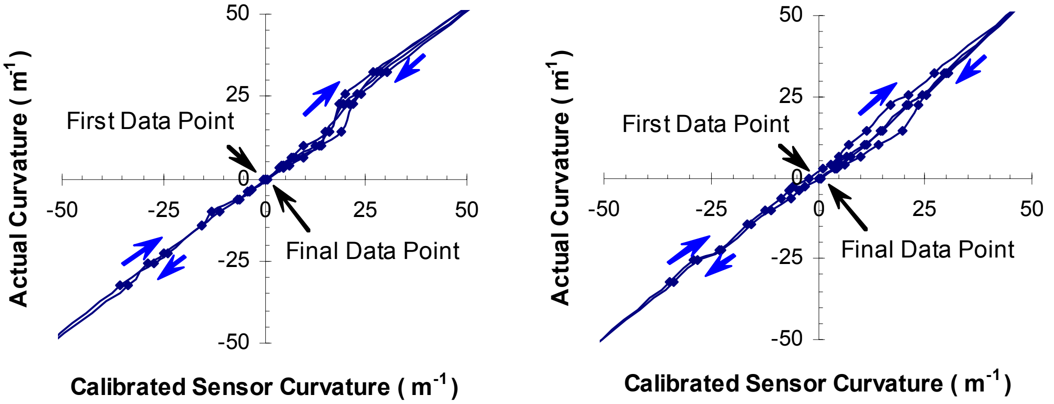

Figure 3-13. Sensor calibration and quantification of mechanical hysteresis for second generation strain gage array prototype. (a) Sensor held against known singly-curved surface. (b) Calibration data for all gage-pairs. (c) Calibration data for a single gage-pair (5th gage-pair). (d) Averaged calibration data for all gage-pairs. Some hysteresis is evident in each graph, as the data form an open loop rather than falling on a straight line.

The variations in sensitivity of the gage-pairs can also be explained by inhomogeneous bonding between the substrate and gages. Variations in bond strength or even delamination will significantly reduced the shear transfer through the substrate, hence reducing the sensor's sensitivity. This could also contribute to the observed hysteretic behavior. The mechanical consequences of a local delamination could easily explain the loss in sensitivity; however, there are also accompanying thermal consequences. These tests were run in a single session, in a laboratory environment, with the sensor in contact with plastic cylinders. Therefore, very little variation in sensor temperature is expected. Even if a thermal imbalance of 10°C were to exist between the gages, this would only result in an error of 0.17 m^{-1}, an order of magnitude less than the observed hysteresis (see typical thermal calculations in section A.2).

Now, returning to answer to the question of "what caused the hysteresis that is observed in Figure 3-13?" It seems most likely that this is a result of inhomogenous bonding conditions between the substrate and gages. This explanation is consistent, both with the magnitude of the hysteresis and with the variations in sensitivity between gage-pairs.

3.5.2.2 Centered Line Load Test

Experimental results are shown in Table 3-5 and Figure 3-14. Table 3-5 reports the maximum calculated displacement at the point of load application, u_{Max}, as well as the absolute error of this displacement, $E_{u,Max}$, compared to the applied displacement, $u_{Applied}$. Results are plotted in Figure 3-14.

The centered line-load tests show that reasonable shape reconstruction can be obtained despite errors in the estimated maximum deflection, u_{Max}. The accuracy of the

Table 3-5. Experimental results for center loaded sensor. Results are presented in increasing order of the magnitude of center deflection.

Load Case	Applied Displacement $u_{Applied}$ [mm]	Calculated Displacement u_{Max} [mm]	Error $E_{u,Max}$ [mm]
Centered Line-Load	0.64	1.13	0.49
	1.27	1.53	0.26
	1.90	1.79	-0.11

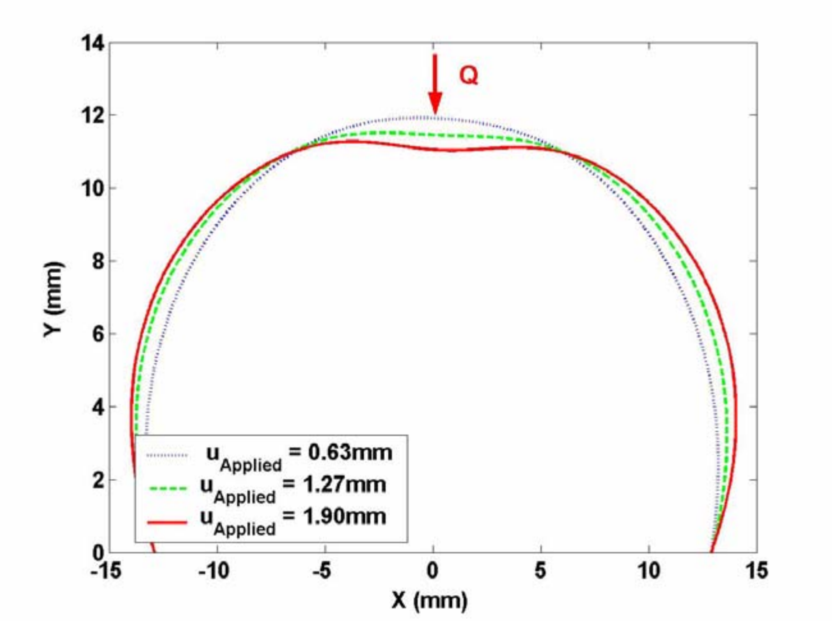

Figure 3-14. Plot of reconstructed shape for centered loaded sensor based on measured curvature

estimated center deflection, u_{Max}, is quite poor for small displacements. However, the accuracy of the calculated center deflection improves as the applied deflection, $u_{Applied}$, increases. The influence of noise on sensor measurements becomes less significant at higher deflections, as deflection induced signals increase.

In looking at these results it is important not only to consider the magnitude of noise, but also their distribution. The reconstruction model presented in section 3.2.1 has the effect of averaging out the contributions of noise over the entire sensor surface and therefore works well when signals have noise components that are zero mean uncorrelated. However, the noise introduced to mechanical sensor hysteresis would be concentrated in the center portion of the sensor, in the inflected region. This would explain the poor performance at low levels of deflection, where noise had a greater influence in comparison to the small curvature changes measured by the gage-pairs. Also, because of the nature of the reconstruction model, additional sensor readings should improve results.

3.6 Conclusions

The approach of directly sensing curvature in a compliant membrane holds promise for dexterous manipulation and telemanipulation. The resulting sensors are inexpensive and robust and can be applied to soft, curved fingertips. Estimation of local object geometry is computationally simple and sensor bandwidth is limited primarily by analog conversion time. If combined with intrinsic contact sensing [Bicchi et al. 1993, and Haidacher and Hirzinger 2002] it is possible to reduce conversion time by only sampling regions of interest.

From calibration testing and thermal modeling, one can conclude that the choice substrate is critical for good sensor performance. The substrate must have good thermal conduction and must be uniformly bonded to the gages in order to dissipate heat and reduce temperature gradients between the gages. Uniform bonding is also important for reducing mechanical hysteresis. The sensor should also be isolated from the environment with a compliant protective skin, such as silicone rubber. Not only will this protect the sensor from damage, it also reduces heat transfer from the environment and thus reduces internal thermal gradients.

Though the sensor concept is validated with this work, levels of mechanical hysteresis are two orders of magnitude greater than the predicted sensor resolution. Future designs will clearly need to improve to be practical for common use.

4 Contact Location Display

At present, telemanipulation systems cannot approach the sensitivity and dexterity of the human hand. To illustrate this point, imagine waking up in the dark and groping for your glasses on the bedside table. Without much difficulty, your fingertips locate the table surface and the glasses resting on it. They manipulate the glasses gently and bring them toward your face. To attempt the same set of operations using a teleoperator would be an exercise in frustration. Without tactile sensors at the slave and tactile displays at the master, locating the glasses would be difficult, and attempts to manipulate the glasses would likely damage them.

Among all the types of sensory information available in the above scenario, none is more important than knowing where objects are touching our fingertips. Early in the study of dexterous manipulation, Fearing [1988] demonstrated that contact information is equally indispensable for manipulating objects in a robotic hand. Without this knowledge, grasp errors accumulate rapidly, and the robot drops the object. Subsequently, many robotics researchers developed tactile array sensors capable of measuring contact location, pressure distribution, and local object geometry.

In contrast, tactile displays that render contact information for virtual reality or teleoperation have proven far more challenging. Accurate recreation of the local shape and pressure distribution at each fingertip requires a dense array of actuators. The peak force, velocity, and displacement required of each element all but preclude packaging the system at the fingertips of a standard haptic display system. The tactile displays that have appeared in the literature are instead benchtop devices, with a small array of pins in a stationary frame, actuated via wires or tubes [Kontarinis et al. 1995, Hasser and Weisenberger 1993, Pawluk et al. 1998, Moy et al. 2000a].

As an alternative, displaying only the location of the centroid of contact on each finger requires far less extensive actuation. Even when objects are handled rapidly, the contacts progress along the fingertips at only a few centimeters per second. To display contact location, it suffices to move a single contact element over the surface of the finger in the proximal/distal and lateral directions, which can be accomplished with just two actuators (Figure 4-1(a)). The experiments reported in sections 4.4 and 4.5 consider only the proximal/distal location of the contact centroid, displayed using a roller that translates along the user's finger pad (Figure 4-1(b)).

Current haptic display systems treat contact even more simply, as a point force applied to the user's fingertip via a thimble. Incorporating contact centroid motion into such haptic interactions requires only minor system changes but improves the interaction significantly. Such a display has the potential to create a richer, more realistic experience of fingertip manipulation than traditional haptic devices provide.

While manipulating an object between our fingers, we receive a wide variety of information about the object such as object stiffness, contact pressure and area (as well as thermal properties) through fingertip receptors. Therefore, the idea of representing arbitrary contacts with a single moving element raises several interesting questions. Of primary concern is how people perceive differences in object curvature. With this device, one can no longer ascertain information about local object geometry from a single static contact, as humans and many robotic tactile sensors [Fearing and Binford 1991, Provancher and Cutkosky 2002] are capable of doing. Contact shape and pressure distribution provide local object information. If this full set of tactile information is not available, one alternative is to adopt an "exploratory procedure" [Klatzky and Lederman 1990] for the human tactile evaluation of curvature, similar to the one outlined by Montana [1988] for robot manipula-

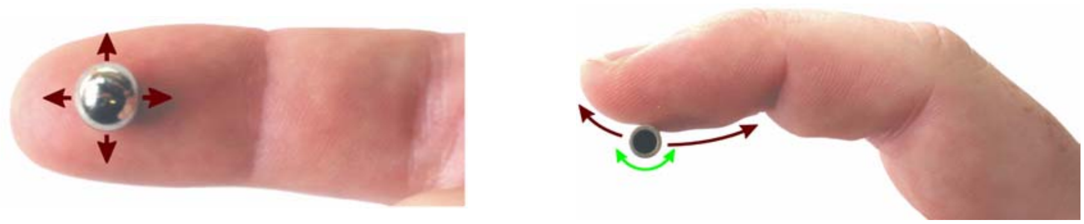
(a) (b)

Figure 4-1. a) Concept for contact location display. The centroid of contact is represented with a single tactile element. (a) Two-dimensional and (b) one-dimensional variations are illustrated.

tors. Montana suggests that one can evaluate object curvature via rolling kinematics by monitoring the migration of the contact patch over the finger surface during manipulation. Contact location is also useful in other manipulation scenarios, such as pushing a knob or slider. In these cases, the migration of the contact patch can indicate sliding or rolling of the object relative to the finger.

To further explore these issues, I have developed a device to display contact location together with force feedback. Two separate experiments were conducted to evaluate the device and the user's relevant perceptions. First, subjects were asked to distinguish between objects of different curvature for both real and virtual interactions. The second experiment studied the perceived motion of a virtual object, simulating rolling and anchored behaviors. The following sections outline previous work in the area of tactile display and describe the device, experiments, and conclusions.

4.1 Previous Work

Many examples of tactile displays have appeared in the literature. Typically, tactile displays consist of an array of pin elements that move normal to the surface. These devices use a wide range of actuator technologies: piezo-electric, shape memory alloy (SMA), electromagnetic, pneumatic, electrorheological, MEMS, and electrotactile. Quite often, these systems are augmented with omnidirectional vibrotactile feedback. For a review of designs and relevant issues, see Shimoga [1993], Kaczmarek and Back-Y-Rita [1993], Burdea [1996], Shimojo [2002] and Tachi [2002]. General design guidelines for tactile display have been reported by Fearing et al. [1997], Peine et al. [1997], Moy et al. [2000b] and Asamura et al. [2001]. An evaluation of various actuator technologies is presented by Kammermeier and Schmidt [2002].

The following subsections provide a review of previous designs, which are classified as active and passive displays. There are three general categories of active tactile displays: displays with an array of vertically-moving pins, displays with laterally-moving elements, and electrotactile displays which stimulate cutaneous touch receptors using an array of finely-spaced electrodes. Researchers have also investigated displays which use materials whose mechanical properties can be modified with the application of electrical currents, such as electrorheological (ER) materials. Since one can only discern these differences through active touch, the designs that utilize this actuation approach are termed "passive."

4.1.1 Vertically Moving Pin Arrays

Some of the first tactile displays were adapted from braille machines. In fact some of the early experiments were completed with such a device, the Optacon[1]. Most braille machines are driven by piezoelectric actuators, which have very good bandwidth but lack the actuation amplitude required to render curved surfaces with a haptic display. The performance of piezoelectric tactile arrays can be enhanced by using bimorph (piezoelectric) actuators as shown by Summers and Chanter [2002], but the pin displacements are still only 50 μm or less. To address these limitations, researchers began experimenting with tactile arrays driven by SMA (shape memory alloy) actuators [Hasser and Weisenberger 1993, Kontarinis et al. 1995, Taylor et al. 1995].

Two primary variations of the SMA-driven design currently exist, both which utilize SMA wires to actuate their pins. In the first variation, SMA wires are placed in-line with the axis of pin actuation and used in combination with a return spring. Such a design is presented by Taylor et al. [1995]. They created a large area 45 x 100 pin array for display to an entire hand.

In the second variation of SMA-driven arrays, the SMA wires run transverse to the axis of pin actuation, allowing greater wire lengths in a thin profile package. The increased wire length also increases total wire end-deflection. These designs incorporate various linkages to convert transverse SMA wire deflection to vertical pin motion.

Hasser et al. [1993, 1996] evaluated a SMA array designed by Dr. A. David Johnson of TiNi Alloy Co. This design utilized SMA wires to pull on L-shaped beam elements in a 5 x 6 pin array. Kontarinis et al. [1995] and Wellman et al. [1998] present a design that incorporates a linkage to transform a small amount of high-force/low-displacement actuation into high-displacement pin actuation (3 mm) with a force of over 1 N. The primary shortcomings of these designs have been device bandwidth and package size. Researchers

---

[1] Optacon is a trademark of TeleSensory, Mountain View, CA. Optacon is no longer in business, though an Israeli company, Virtouch Ltd, now sells an inexpensive mouse which includes two braille cells (the VirTouch Mouse, VTM, for about $700).

have optimized bandwidth with clever control schemes and by water-cooling the SMA wires [Howe et al. 1995]. Displays with a single line of pins have also been built to reduce package size. These devices can be placed on robotic masters for telepalpation [Peine et al. 1994].

In an effort to further improve device bandwidth, researchers have investigated designs driven by solenoids [Fischer et al. 1995], voice-coils [Pawluk et al. 1998], and other electromagnetic actuators. Kammermeier et al. [2000] produced a 6 x 6 pin array (3mm pin spacing) driven by electro-magnetic rocker-lever actuators driven open-loop. With this design, they are able to accomplish an actuation stroke of 1.6 mm at 4.5 N and an impressive bandwidth exceeding 100 Hz. Fukuda et al. [1997] used an array (3 x 3) of electromagnetic resonators in their device.

Researchers have also pursued pneumatic designs driven by the desire to make these devices more compact and lightweight [Cohn et al. 1992, Caldwell et al. 1999, Moy et al. 2000a]. Cohn et al. [1992] present one of the first pnuematically-actuated tactile displays composed of an array of pneumatic cylinders. Moy et al. [2000a] have designed a 5 Hz display composed of a 5 x 5 array of small air pockets driven via PWM with binary valves. Binary valves were chosen because of their suitability for miniaturization. The display is fastened to a user's fingertip, supplied with air, and controlled by an external source via individual air lines. Caldwell et al. [1999] report a similar glove-based design that also supplies vibrotactile and either thermal or shear feedback. Caldwell et al. accomplish an impressive 11 Hz on the 4 x 4 array with proportionally-controlled valves. Asamura et al. [1998] have similarly augmented their device by adding vibrotactile feedback to an array of airjets. In fact, many researchers have augmented their devices with vibrotactile feedback. Kontarinis and Howe [1995] show that vibrotactile feedback can be a simple yet effective way to display the high frequency content present during slip and collision. They show that even a single voice-coil actuator improves performance. Furthermore, the orientation of the vibrating element does not appear to be critical, thus allowing flexible packaging.

Several researchers have taken a more pragmatic approach to the design of tactile displays by using commercially available servomotors in their design [Wagner et al. 2002, Iwata et al. 2001]. Wagner et al. [2002] present a tiered 6 x 6 construction with a small motion bandwidth of 25 Hz accomplished with commercial RC servo motors. Iwata et al. [2001] present a full hand tactile display with pins driven by DC motors and leadscrews.

In the interests of further miniaturization, Ghodssi et al. [1996] present one of the first MEMS-based tactile arrays. Siegel [2002] reports another interesting MEMS array designed by Fedder and Lopez[2] at Carnegie-Mellon. Fedder and Lopez use electrostatic forces to actuate their MEMS array. Each element of their array contains air trapped between a metal-coated polymer membrane and silicon substrate. Each element consists of a center chamber connected to an annular chamber. When an attractive electrostatic charge is applied to the annular region, that portion of the membrane collapses, forcing the air to bulge the central tactile element. With the ongoing goal of producing tactile displays at a smaller scale, one may expect to see more MEMS designs emerge in the future.

4.1.2 Laterally Moving Pin Arrays

Another novel display design is presented by Hayward et al. [2000]. Their design utilizes an array of 64 piezoelectric actuators that move an array of 112 pins laterally rather than normal to the surface of the skin. This device presents distributed skin stretch[3]. It is particularly attractive because of its small relative size and ability to integrate with device electronics.

4.1.3 Electrotactile Arrays

Ultimately, one might like to provide sensation directly to the nerve endings of the finger, thus eliminating the need for external hardware. As a middle ground, researchers such as Tang and Beebe [1998] provide electrostatic[4] feedback to the fingerpad of a user in a band-aid sized package. However, despite the advantages of slim packaging, users have not embraced it due to discomfort. For a more in depth review of this technology (as well as vibrotactile feedback), see Kaczmarek et al. [1991].

---

[2] http://www.ri.cmu.edu/projects/project_470.html

[3] Immersion corp. developed a trackpad for laptop computers which incorporated lateral motion of the entire trackpad, for tactile feedback. However, the trackpad was never commercialized.

[4] Electrostatic is a voltage-controlled form of electrotactile feedback (which is current based)

4.1.4 Passive Arrays

In contrast to pin arrays, which actively stimulate the user's fingertip, Monkman [1992], Taylor et al. [1995] and Voyles et al. [1996], present tactile arrays with a thin layer of electrorheological (ER) fluid beneath a conductive rubber skin. In these designs, electrodes beneath the rubber surface alter the viscosity of the ER fluid, thus locally increasing the resistance experienced when stroking a finger across its surface. It should be noted that, Voyles et al. [1996] present their design along with a companion tactile sensor of similar construction.

4.2 Device Design

Figure 4-2 shows a solid model of the apparatus developed to investigate the display of contact location. The tactile element is a small roller housed in a thimble that slips over the user's finger. A servo-motor drives the roller along the user's finger via two sheathed push-pull wires. The roller is suspended underneath the fingertip by these drive wires, so that it does not touch the user when no forces are applied. Figure 4-3(a) shows a picture of the prototype.

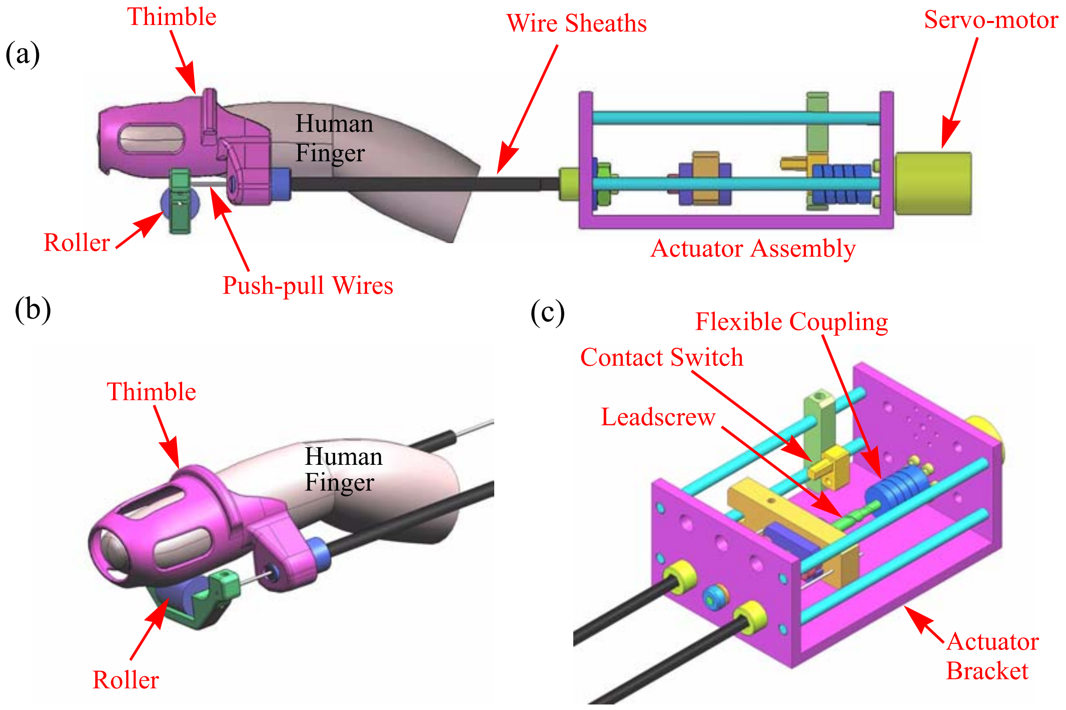

Figure 4-2. Solid Model of the contact location display. (a) Side view of the device and close-ups of the (b) thimble and (c) actuator.

The display's roller is attached to a Phantom™, a robotic arm used for haptic feedback, as depicted in Figure 4-3(b). The Phantom™ is used to measure the position of the user's finger and to provide reaction forces, which push the suspended roller into contact with the user's finger. The display can thus render the making and breaking of contact as shown in Figure 4-4. As noted by Yoshikawa and Nagura [1999] and Springer and Ferrier [2002], this type of arrangement yields a realistic sensation of contact as the roller stimulates mechanoreceptors in the user's fingertip.

The present design locates the roller actuator remotely on the user's forearm. This placement reduces device inertia at the hand and minimizes actuator vibration transmitted to the user's fingertip mechanoreceptors. A series of interchangeable thimbles was created

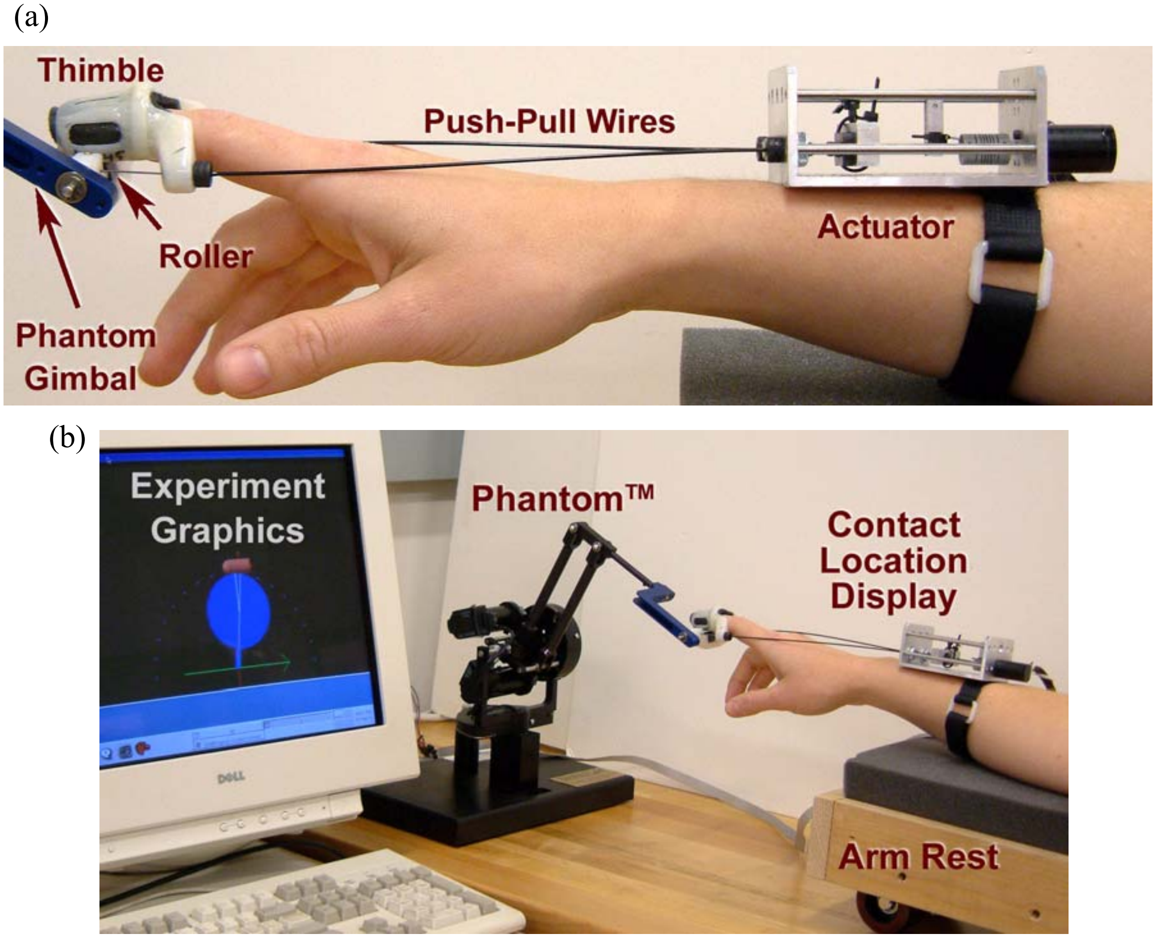

Figure 4-3. a) Prototype of contact location display. Contacts are rendered by a roller housed in a thimble. The roller is attached to a commercial force-feedback device to provide reaction forces to the finger. A small servo-motor provides precise positioning of the roller via push-pull wires. The roller is suspended below the finger, only touching the user when interaction forces are displayed by the Phantom$^{\text{TM}}$. b) Experimental setup and graphics showing a contact between the user's finger and a virtual object.

using rapid-prototyping techniques to insure a snug fit for subjects with a range of finger sizes. In order to display haptic interactions with this device, virtual objects were programmed in C on a computer running RTai Linux.

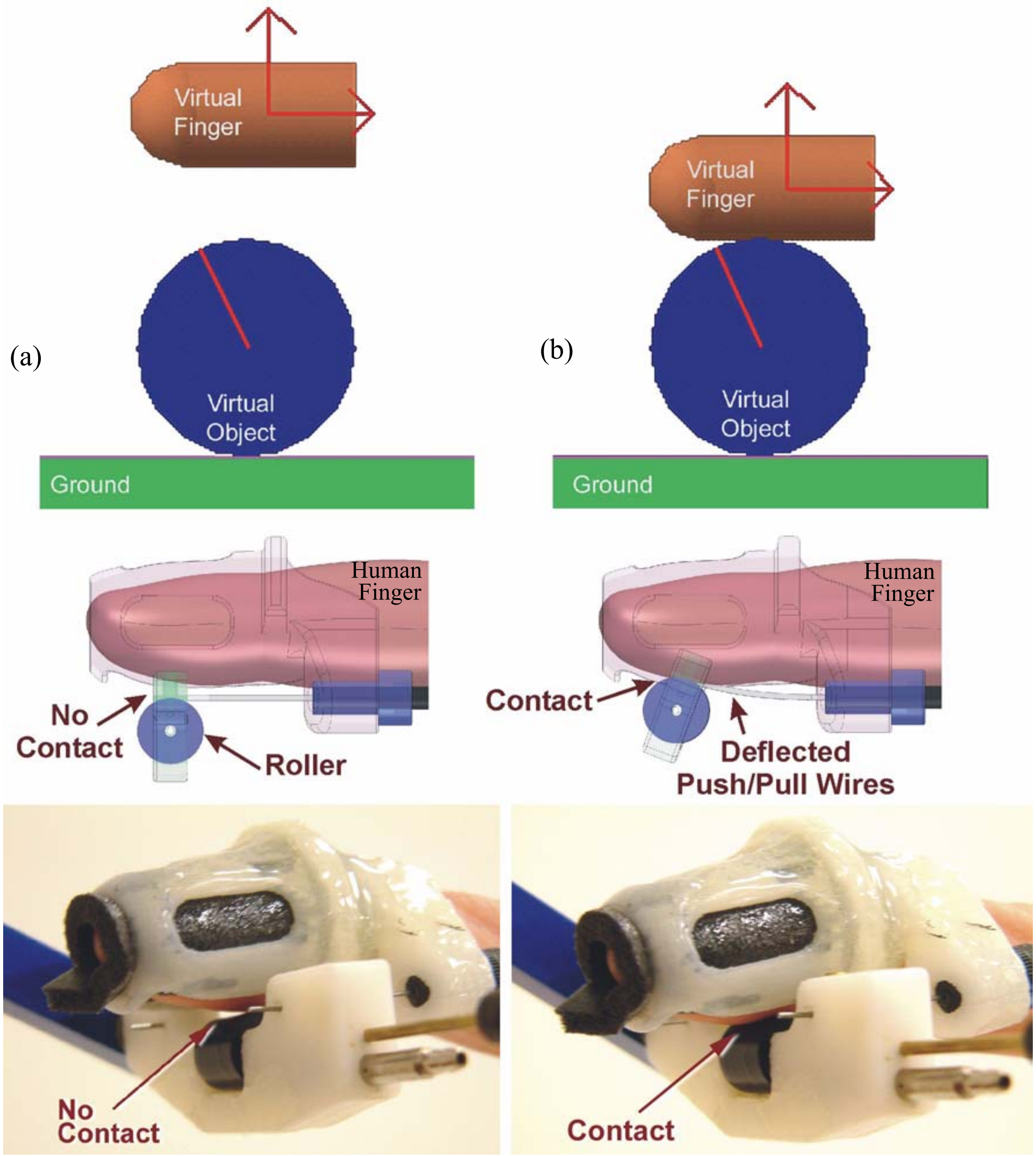

Figure 4-4. The illusion of making and breaking contact with virtual objects is enhanced as the tactile element is brought into contact with the user's finger when making contact. Experimental graphics are shown along with solid models and pictures of the thimble in analogous states. (a) In free-space, the roller remains separated from the user's finger. (b) Interaction forces, supplied by the haptic feedback device, bring the roller into contact with the users finger when making contact with virtual objects.

Figure 4-5 depicts the control scheme used to regulate horizontal object position during psychophysical testing. The kinematics of each simulated environment determine a characteristic relationship between finger motion and contact location. This shows up in the control law in the block labeled "kinematic model" in Figure 4-5(b). For example, for object motion experiments, the desired Phantom™/roller position is determined by the object motion ratio, α; hence, the reference input, $R(s) = \alpha \cdot x_{Finger}$. The motion kinematics for experiments in curvature perception are slightly more complex and are described in Appendix B. Assuming that the finger remains horizontal, the finger position can be calculated as $x_{Finger} = x_{Roller} - x_{Contact}$. The controller closes a loop around Phantom™/roller position, x_{Roller}, compared to the reference, R(s), thus ensuring accurate rendering of object position (see Figure 4-5(b)). A proportional-integral-derivative (PID) feedback controller was employed to ensure accurate positioning of the contact using the display's servo-motor to adjust the position of the roller.

There is an interesting philosophical question that arises for the design and control of motions for this device. In contrast to traditional haptic devices, which are designed to be backdriveable, the current design is actuated with a high pitch leadscrew. Whereas backdriveability is essential for force feedback with haptic devices, it was the *positions* of contacts that were critical for the human subject tests of this device. It was felt that accurate positioning would be best accomplished with a leadscrew. However, since the device is used in combination with a low inertia, backdriveable linkage (Phantom™), it is also possible to accurately render interaction forces transmitted through the thimble.

In contrast to the horizontal contact positions (controlled using the contact display servo-motor), the vertical reaction forces were rendered by the Phantom™. These forces were computed based on the depth of object penetration of the virtual finger and were enforced using standard impedance control [Hogan 1985]. Typical interpenetration depths were on the order of 5 mm. To ensure stable interaction and prevent motor saturation, the empirically determined gains limited interaction forces to a maximum of 10 N. As with many haptic interactions, this gives virtual objects a "squishy" feel. To reduce the perceived compliance of virtual objects, displayed object interpenetration for graphics was reduced by a scaling factor. This follows in the same spirit of Zilles and Salisbury's [1995] god-object method.

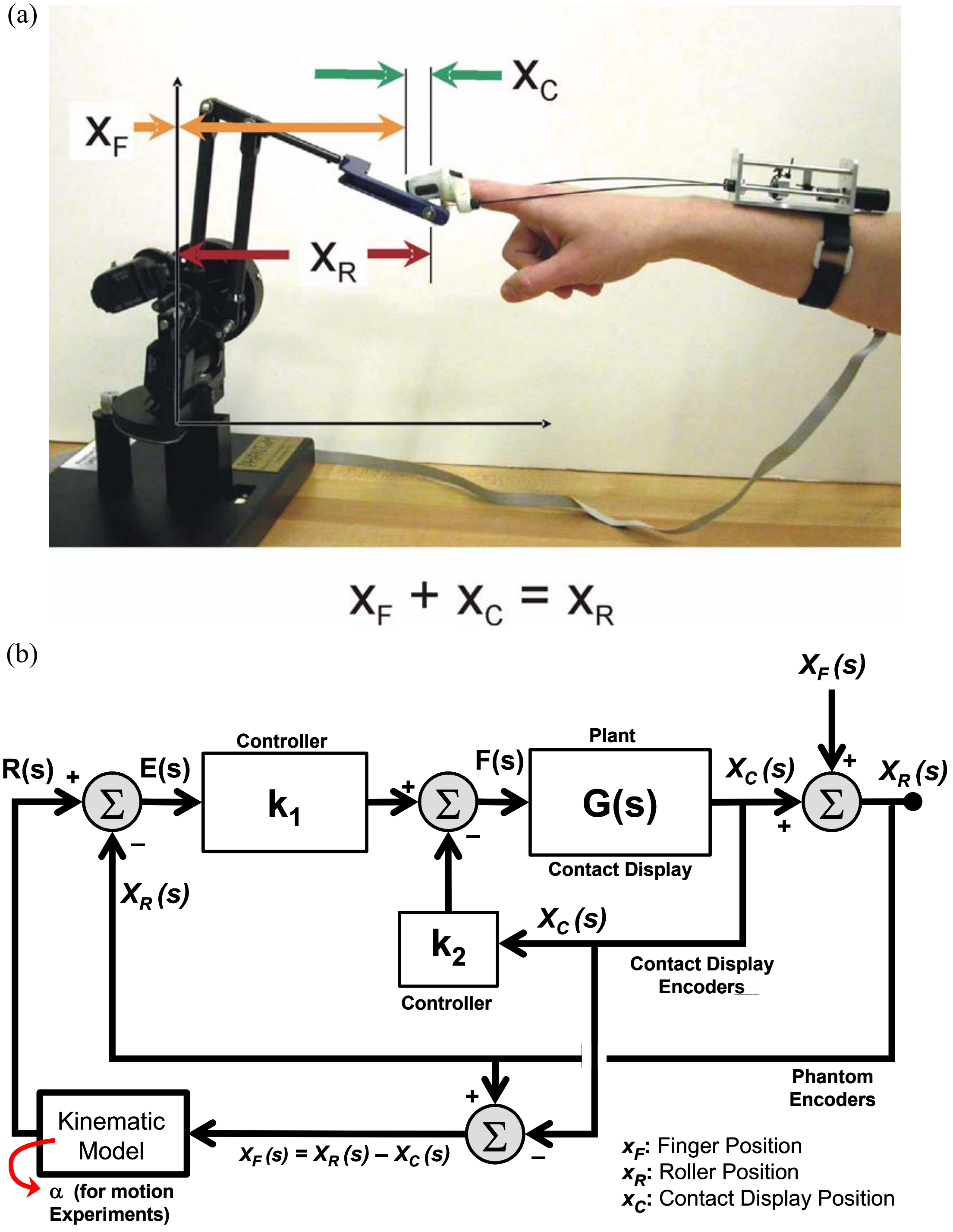

Figure 4-5. Contact display control diagram. Motions of the contact were driven as a function of finger position, x_F. Finger position was calculated from known Phantom™/roller position, x_R, and contact display leadscrew position, x_C. As shown in (a) $x_F = x_R - x_C$. (b) Controller block diagram. The desired Phantom™/roller position was driven by a kinematic contact model. For example, for object motion experiments, the reference input, $R(s) = \alpha \cdot x_F$. Controller design and graphics are shown courtesy of Katherine J. Kuchenbecker of the Stanford Telerobotics Lab.

The small motion closed-loop bandwidth of the roller exceeds 5 Hz for a travel of 10 mm (the actual bandwidth was determined by driving the roller with a 10 mm pk-pk sinusoidal input was determined to be approximately 8 Hz). Roller positions along the finger are rendered with a maximum error of 0.05 mm for fast hand motions (5 cm/sec) and an error of about 0.01 mm for the slow motions typically used by subjects. For additional details of the device design see Appendix B.

4.3 Experimental Goals and Approach

Two sets of experiments were conducted to evaluate the device and the merits of displaying contact location to users. Of primary concern is how subjects interpret virtual object interactions when each of the contacts is represented by the same (constant curvature) tactile element (a roller). To investigate this effect, a first set of experiments was constructed in which object kinematics were directly proportional to object curvature. Subjects were asked to distinguish between objects of different curvature for both real and virtual interactions. The experiments in perception of object curvature are described in section 4.4. In a second set of experiments, described in section 4.5, subjects discriminated between objects with differing motion conditions. The motion of the virtual objects rendered in these experiments was independent of object radius.

The goal of the two sets of experiments is to answer the following questions:

- How does a subject's ability to discriminate between objects of varying curvature handled directly compare to his ability when handling virtual objects rendered via the contact location display?
- Can subjects identify motion conditions, found in prototypical manipulation tasks, of virtual objects rendered via contact location display?

The following subsection describes the framework and detailed protocol followed in both experiments.

4.3.1 General Experimental Protocol

Both of the conducted experiments followed the same general protocol. The experimental approach was reviewed by established researchers in the fields of psychophysics and neurphysiology[5] and followed closely to the methods outlined by Gescheider [1997]. For a general review of classical psychophysical methods, refer back to chapter 2 of this thesis.

All experiments employed the method of constant stimuli with a paired-comparison forced-choice protocol to evaluate perceptual thresholds (JNDs) and sensitivity. To investigate perceptual sensitivity over a broad range, the experiment was divided into blocks. In each block, subjects were presented with stimuli clustered around a nominal value, referred to as a standard stimulus. Each standard was accompanied by six comparison stimuli (three larger and three smaller, presented twice each). Subjects were presented with two stimuli in rapid succession (separated by 2-4 seconds) and asked to state which met the specified condition. Standard precautions were taken to prevent presentation order bias. To isolate the effects of learning and fatigue, half of the subjects completed virtual discrimination experiments first. Subjects were blindfolded and wore hunter's earmuffs to reduce distractions and ambient noise.

Sighted and blindfolded training preceded each block of testing. Virtual simulations were accompanied by computer graphics to reinforce haptic cues during training. Positive feedback on discrimination accuracy was provided at the beginning of curvature discrimination experiments. However, it was not provided in motion discrimination experiments to prevent habituation.

All subjects completed the experiment using the index finger of their right hand. For consistency between virtual- and direct-discrimination experiments, subjects performed these tests with their fingers extended and horizontal. The virtual apparatus did not measure rotations of the subject's finger, and kinematic modeling assumed that the finger orientation was always horizontal. The subject's fingers were placed at the center of each stimulus. They made a single sustained contact with each stimulus and were not to allowed to slide on the stimulus' surface while exploring the physical models.

There were no time restrictions made on subjects during testing. However, to minimize the time required of each subject, tests were completed by two test groups. A majority of subjects completed the test in under one-and-a-half hours. There were 14 people in the

---

[5] Experiments were discussed in pilot testing stage with Susan Lederman of Queens University and Mandayam Srinivasan of MIT.

first test group, which consisted of 10 males and 4 females ranging in age from 20 to 34. All subjects in this group were right-handed. There were 10 people in the second group, which consisted of 8 males and 2 females ranging in age from 20 to 38. Two of the males in the second group were left handed. The number of people completing virtual or direct experiments first was equally balanced (i.e., for the second group, 1 left-handed male and 3 right-handed males, and 1 right-handed female completed the virtual experiments first). Subjects completed a short questionnaire at the conclusion of the experiments.

4.4 Curvature Discrimination for Real and Virtual Objects

A series of experiments was performed to quantify a user's ability to discriminate between objects of varying curvature. To simplify testing, only planar objects were studied and the interaction was limited to horizontal motion of a single finger. This simplification allowed a direct comparison of results between direct physical manipulation and manipulation with virtual objects via the contact display device.

As outlined in section 4.3.1, the experiments were designed following standard psychophysical procedures involving constant stimuli, with forced-choice comparisons between pairs of cases [Gescheider 1997].

4.4.1 Experimental Procedure

These discrimination tests focused on the user's perception of curvature while rolling planar objects with a single finger. As illustrated in Figure 4-6(a), such simple one-fingered interaction is representative of more general object manipulation. All objects, whether real or virtual, pivoted about a fixed axis distinct from the centers of curvature. This pivoting motion allowed the user to explore the curved surface using only a fingertip movement. For convenience, fourteen test curves were arranged onto a single "curvature wheel," as is shown in Figure 4-6(b). Two wheels were used for the experiments, each with stimuli for two standards. For each curve, the wheel could pivot 15°, corresponding to approximately ±1 cm of fingertip movement. The radius of curvature of the objects varied from 8.3 mm to 52.6 mm.

During the tests, subjects were blindfolded and used an armrest to maintain a horizontal hand position. Both real and virtual versions of the curvature wheel were presented in the same fashion. For the physical wheel, the limits of travel for each sector were indicated with spring-loaded ball detents; analogous force detents were implemented in software for the virtual wheel. Graphics shown during training of the virtual curvature discrimination experiments are shown in Figure 4-6(c).

The curvature discriminations were conducted as a randomized series of comparisons in which users compared two stimuli and reported which of the two samples had a larger radius of curvature. For each comparison, one of the two samples was a standard value, while the other was selected from among six comparison stimuli (three smaller and three larger neighboring sizes). The sizes were explicitly chosen to determine the just noticeable difference (JND) [Gescheider 1997] relative to the standard size. This meant that comparison stimuli for direct and virtual discriminations would not necessarily match.

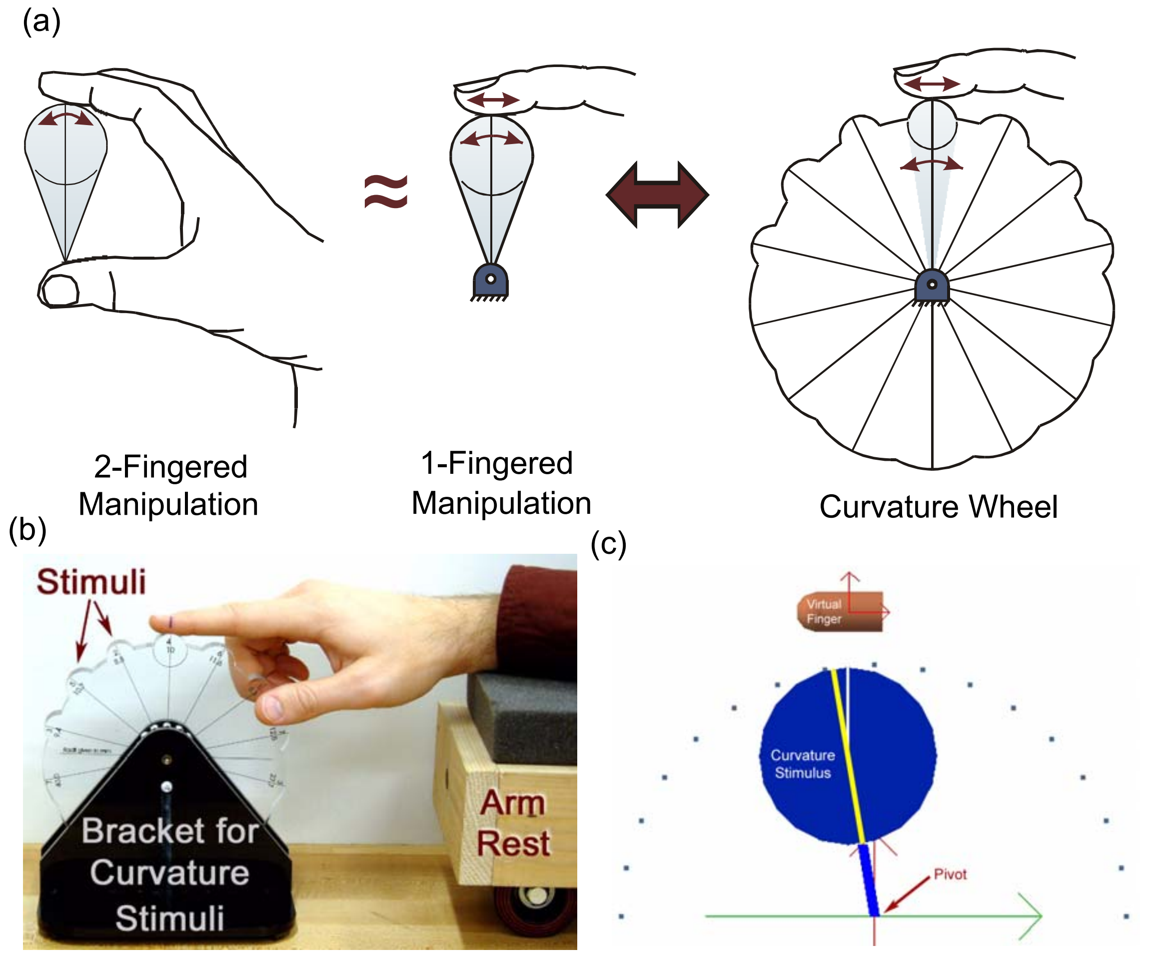

Figure 4-6. (a) One-fingered planar perception of curvature provides a simplified form of object manipulation and highlights the use of contact location while exploring an object's geometry. (b) The experiments were performed exploring 15° sectors of a "curvature wheel" for the direct manipulation. An arm rest, that could roll horizontally, helped users maintain horizontal motion. (c) Experiment graphics used during initial training.

Gescheider [1997] recommends selecting comparison stimuli such that the easiest to distinguish from the standard (the largest and smallest stimuli) can be identified approximately 90% of the time. The remaining comparison stimuli are equally spaced between the extremes and the standard. As with any psychophysical experiment, pilot tests were conducted to ensure that stimuli were appropriately chosen. Pilot testing is essential to the success of any set of perceptual experiments, as one can improve procedure or modify the tests performed before making a more significant time investment during subject tests. Subjects made curvature discriminations with respect to four radius standards ranging from 10 mm to 40 mm.

4.4.2 Results and Discussion of Curvature Discrimination Experiments

Results for direct and virtual curvature comparison tests are shown in Table 4-1 and Figure 4-7. The graphs in Figure 4-7 represent the pooled responses of all subjects for 10, 20, 30, and 40 mm standards. They plot the proportion of times subjects reported each stimulus as the larger of the two presented.

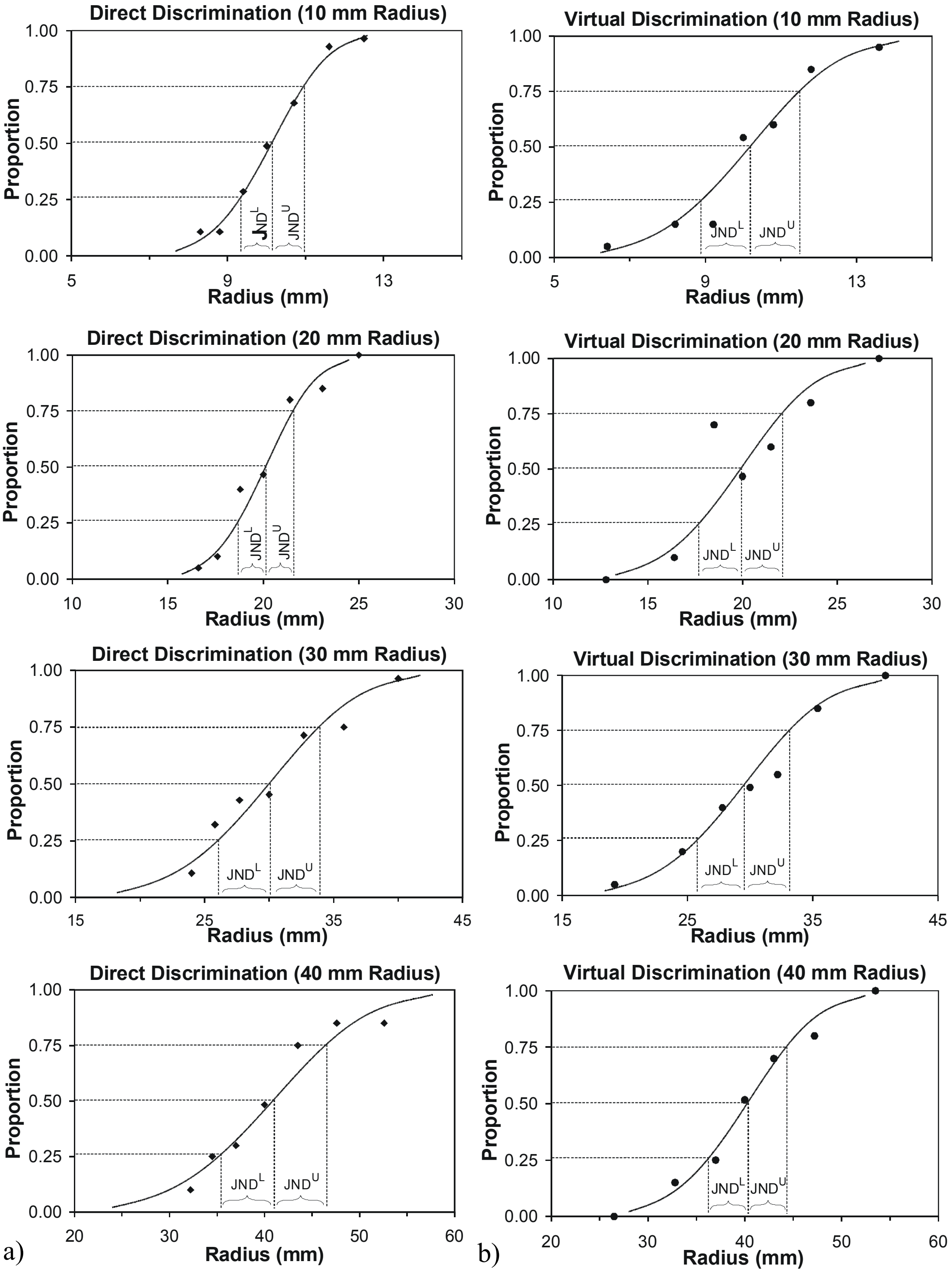

Figure 4-7. Pooled results of all subjects for radius of curvature discriminations during (a) direct physical interaction and (b) simulated virtual interaction rendered via the contact location display. The graphs display the proportion of times a particular stimulus was reported as having a greater radius of curvature. The JNDs are indicated with dotted lines.

As expected, the data have a sigmoidal distribution; stimuli that are considerably different from the standard are almost always correctly identified, while smaller differences are harder to discern (see section 2.2.2.1 for more rigorous explanation). Figure 4-8 illustrates the method by which curves were fit to subject data. As outlined by Gescheider [1997], the sigmoidal curve fit was established by converting the proportions which subjects chose a particular stimulus as being the greater of the pair of stimuli presented in each trial. These proportions are converted to z-scores, the abscissa of a "standard normal distribution[6]." Once converted to z-scores, a line is fit to the data by the method of least squares. The sigmoidal curve fit results from converting the linear fit back to equivalent proportions. By convention, the JND for each standard is established as the average of the upper and lower difference thresholds (JND^U, JND^L, see Figure 4-7), being the difference between 0.75 and 0.50, and 0.50 and 0.25 proportions, respectively [Gescheider 1997] (see chapter 2 for more details).

The data reported in Table 4-1 are shown as both the JND and the Weber fraction. The Weber fraction is the ratio of the JND to the nominal stimulus value. The JNDs are also plotted against the nominal values in Figure 4-9. The direct discrimination data are slightly nonlinear and are fit by a power curve (as suggested by Steven's Power Law [Gescheider 1997]). In contrast, the virtual discrimination data are nearly linear with object size, in agreement with the underlying motion kinematics of the simulation. The average Weber

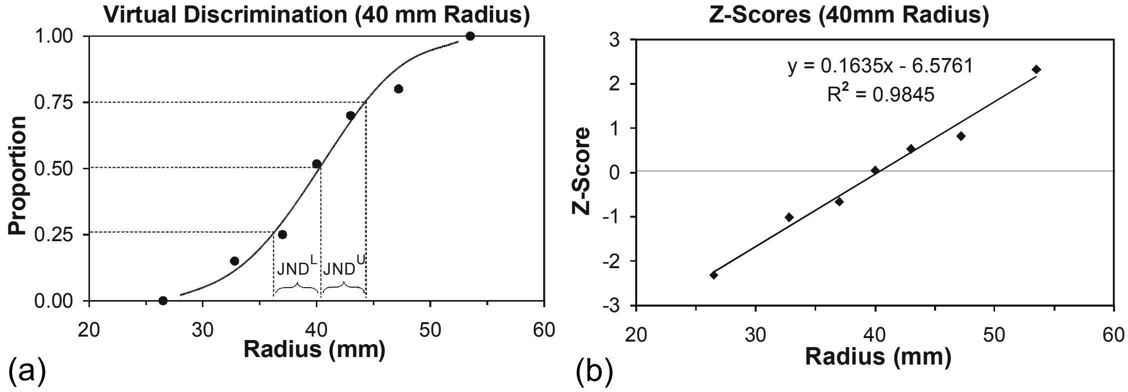

Figure 4-8. Methodology of curve fit for typical data. Sigmoidal curve fit established by converting proportions to z-scores (abscissa) of a "standard normal distribution[4]." Once converted to z-scores, a line is fit to the data by the method of least squares (shown in (b)). The sigmoidal curve fit results from converting the linear fit back to equivalent proportions (shown in (a)).

---

[6] A normal distribution with a mean of zero and standard deviation of one represents the "standard normal distribution."

fraction for virtual discriminations across the range of stimuli tested is about 0.11. This is consistent with the level of sensitivity reported by Biggs and Srinivasan [2002] for other cutaneous sensing modalities.

Table 4-1. Results of direct and virtual radius of curvature perception experiments in the form of JNDs and Weber fractions for each curvature standard. The right side of the table shows length-based results for virtual discriminations.

	Direct Discrimination		Virtual Discrimination		Length-Based Discrimination		
Radius [mm]	Radius [mm]	Weber Fraction	Radius [mm]	Weber Fraction	Nominal Roller Travel [mm]	Radius [mm]	Weber Fraction
10	0.84	0.084	1.35	0.135	2.67	0.36	0.135
20	1.49	0.074	2.25[a]	0.112[a]	5.33	0.60[a]	0.112[a]
30	4.00	0.133	3.77	0.126	8.00	1.01	0.126
40	5.74	0.143	4.16	0.104	10.67	1.11	0.104

---

a. Data reported from pilot study representing 5 subjects.

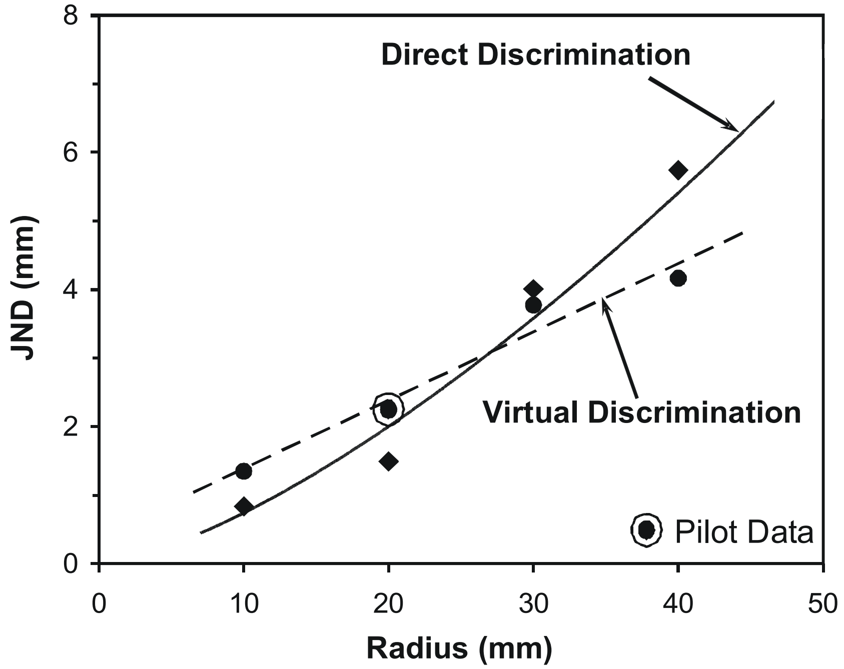

Figure 4-9. JNDs of direct and virtual radius of curvature discrimination tests are plotted versus their nominal stimuli value.

Direct exploration of objects smaller than 25 mm in radius yields better performance (smaller JND) than virtual discrimination. The presumption is that for small objects, local pressure distribution, which is not rendered by the virtual display, becomes the dominant mode of perception. For radii above 30 mm, subjects performed better with virtual contacts. Here it is believed that the relatively small size of the roller in the contact display provides better localization and hence better contact movement cues than the increased contact patch experienced in direct manipulation. Subjects also commented that they found the larger radius virtual discriminations easier to perform.

Per experimental protocol, the anticipated factors which could impact experimental results were balanced. For example, half the subjects completed direct curvature discrimination trials at the beginning of the experiment while the others began with virtual cases. Also, each of the combinations was presented twice, with the order of presentation reversed the second time the trial was presented. While balancing these effects is important for establishing perceptual thresholds, it is also informative to examine the data partitioned by these distinctions. An examination of these groups can reveal effects of learning and fatigue

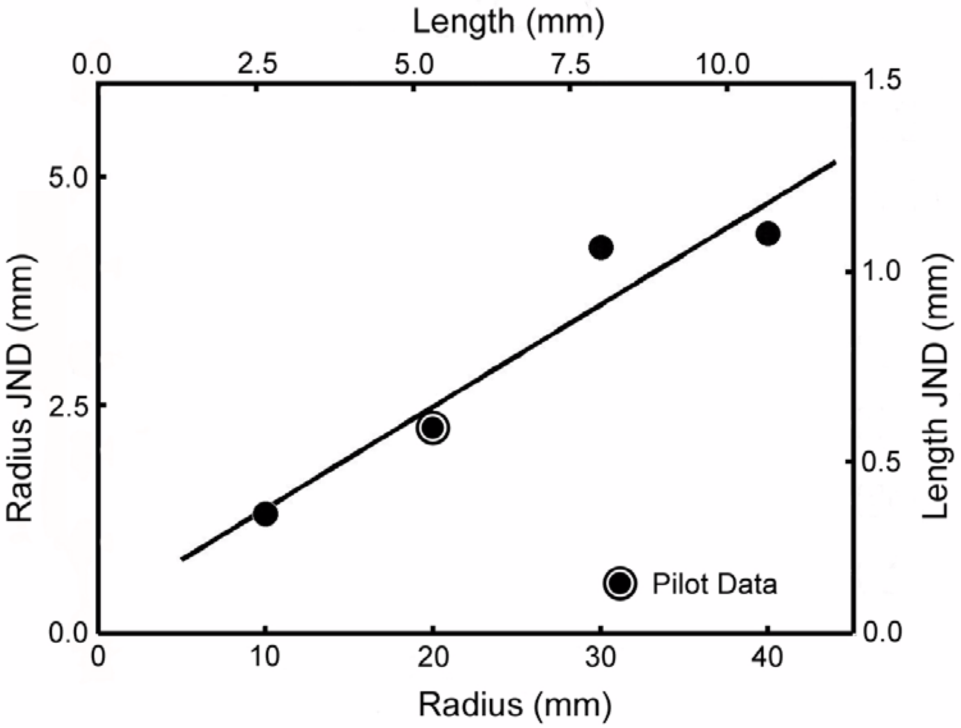

Figure 4-10. Radius and equivalent length JNDs for virtual discrimination tests.

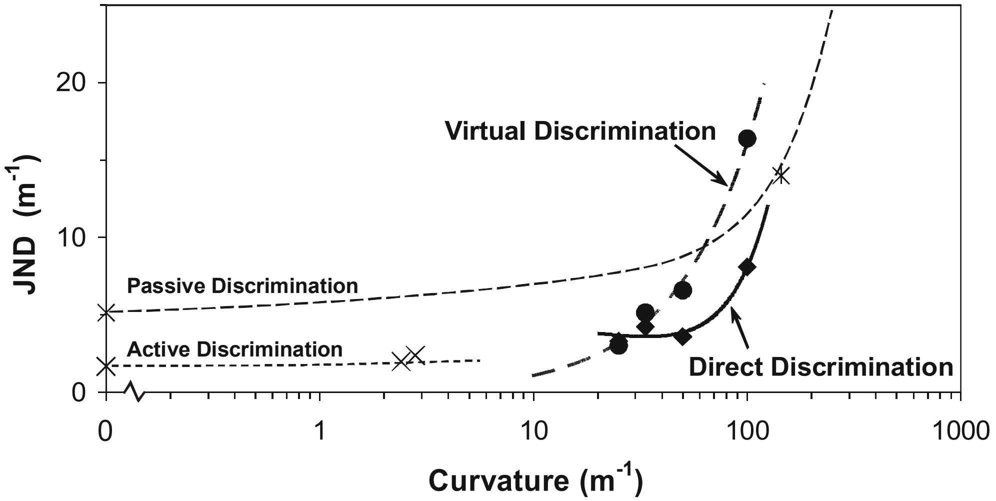

Figure 4-11. Results are framed by data reported in the literature for active fingertip curvature discrimination (Gordon and Morison [1982]) and passive discrimination (Goodwin et al. [1991]).

present in the experiment. Statistical analysis of subjects' results partitioned into the above groups revealed two major findings. First, it was found that, in general, subjects performed better at the beginning of the experiment (by as much as 28%). This indicates that fatigue was possibly a factor in the experiment. The second major finding was that subjects were more likely to spuriously identify a given stimulus as being larger if a smaller radius stimulus was presented before a larger stimulus. For direct curvature discrimination, this was 30% more likely to occur as opposed to 24% for virtual experiments. Similar trends are often found in psychophysical testing [Gescheider 1997].

By design, the contact location display relies on perception of motion on the fingertip. Limited to 15° sectors, objects with radii of curvature of 10 mm, 20 mm, 30 mm, and 40 mm lead to nominal contact movements of 2.67 mm, 5.33 mm, 8.00 mm, and 10.67 mm and JNDs of 0.36 mm, 0.60 mm, 1.01 mm, and 1.11 mm, respectively. The results of virtual curvature discrimination experiments are replotted with both radius and length axes and corresponding JNDs in Figure 4-10. As with radius, the Weber fraction for tactile length discrimination averages to 0.11. This is quite reasonable, as Biggs and Srinivasan [2002] report a Weber fraction of 10% for other length discriminations.

Many researchers have investigated the perception of curvature [Gordon and Morison 1982, Goodwin et al. 1991, Kappers et al. 1994, Louw et al. 2002]. The findings of

Gordon and Morison [1982] and Goodwin et al. [1991] are especially relevant. Similar to the present experiments, the subjects of these experiments judged object curvature with the tip of their finger. Figure 4-11 compares the curvature discrimination results to data presented by these researchers. Gordon and Morison [1982] had subjects actively explore plano-convex lenses with their fingertips. In contrast, Goodwin et al. [1991] pressed hemispherical stimuli onto the fingertips of their test subjects. These two experiments represent active and passive discrimination of curvature, respectively. As reported by Loomis and Lederman [1986], one would expect discriminations by active touch to be more accurate than those made by passive touch. While the current experiment has aspects of active touch, the motions of a subject’s finger were somewhat restricted. The results are expected to be bounded by those reported by Gordon and Morison [1982] and Goodwin et al. [1991]. The data reported by Gordon and Morison represent the expected lower bound for the experiment, while perception of curvature via passive touch, reported by Goodwin et al., represents the expected upper bound for the results. One can see that with the exception of extreme virtual cases, the data are indeed bounded.

While trends in the JND data hint at different perception strategies, especially at extreme object sizes, the magnitudes of the JNDs are similar for real and virtual tests. This experiment not only quantifies the user's perception capability, but also validates that the device can effectively communicate information necessary for virtual object discrimination.

4.5 Perception of Object Motion

A second series of experiments was performed to investigate the user's perception of object motion via the contact location display. Relative movement of a grasped object provides important cues about the object's behavior and state. For example, to identify an object picked from our pocket, we generally roll an object between our fingers. Knowledge of the location and motion of the contacts allows us to maintain a stable grasp while exploring the features of the object. The following subsections describe a simple test that illustrates the applicability of the contact display device for manipulation.

4.5.1 Experimental Procedure

Motion of an object can be described as anchored, rolling, or sliding, as shown in Figure 4-12. Changes in contact location along the fingerpad indicate relative movement between the finger and the object. At one extreme, sliding an object maintains a constant contact location relative to the fingertip. In contrast, touching an anchored object fixes the contact in space regardless of finger motion. More generally, the object motion ratio, α, relates finger and object movements according to:

$$\Delta X_O = \alpha \cdot \Delta X_F \tag{4.1}$$

where ΔX_F is the motion of the user's finger while in contact with the virtual object and ΔX_O is the resulting object motion.

Similar to the previous experiments, subjects were presented with a series of comparisons in which various object motion behaviors were presented. Ratios of $\alpha = -0.5...0.5$ were tested against a nominal anchored object with $\alpha = 0$ (Figure 4-12(a)). In a second series, ratios of $\alpha = 0.1...0.9$ were compared to a nominal rolling object with $\alpha = 0.5$ (Figure 4-12(b)). In each comparison, subjects were asked which of the pair felt more anchored or rolling, respectively (The case of pure sliding (Figure 4-12(c)), with no motion relative to the fingertip, was not tested as it was too easy to distinguish from the other

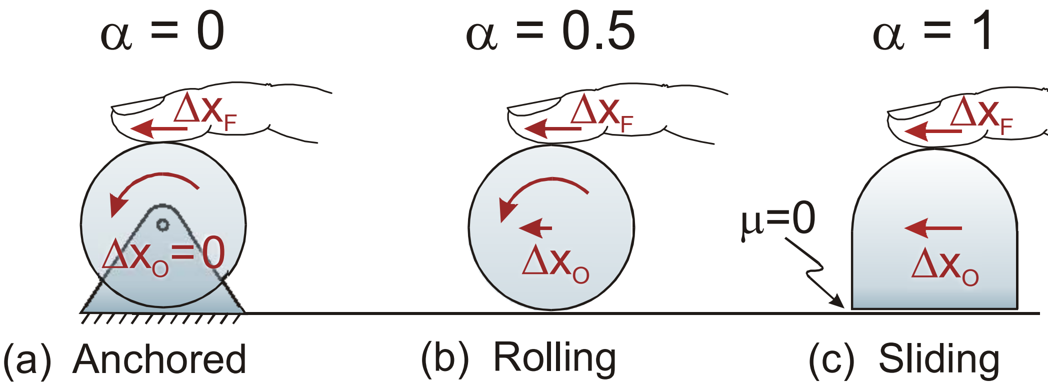

Figure 4-12. Differences in apparent object motion can be described in terms of a ratio, $\alpha = \Delta X_O / \Delta X_F$, where ΔX_O is the object displacement and ΔX_F is the fingertip displacement. Values of α for familiar object motions are depicted above.

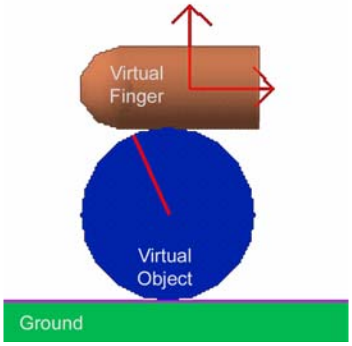

Figure 4-13. Graphics for object motion experiment.

cases). The graphics that accompanied initial training for each subject are shown in Figure 4-13.

4.5.2 Results and Discussion of Object Motion Experiments

Figures 4-14(a) and 4-14(b) show the proportions of times that subjects identified a virtual object with a given value of α as anchored or freely rolling, respectively.

It is believed that people evaluated object motion based on a comparison between absolute finger movement, observed via proprioception, and relative contact centroid movement, observed cutaneously. Based on the results of curvature discrimination experiment, the cutaneous contribution to this comparison is quite accurate. Proprioceptive length estimates are not nearly as good, which could explain the spread of the data. The standard deviation for rolling object tests was substantially smaller than for anchored objects, which can be attributed to peoples' experience rolling and manipulating objects in their hands.

The means of the anchored and rolling distributions are -0.09 and 0.56, respectively, falling close to their nominal values of 0.0 and 0.5. This mismatch is an interesting perceptual result of these unsighted object manipulations, though its exact origin is unknown. Particularly noteworthy is users' preference for negative ratios in the anchored object tests. Unlike real objects, these objects move in opposition to the fingertip input, exaggerating normal sensations.

As with the curvature discrimination results discussed earlier, statistical analysis was also completed for object motion experiments. The present data were partitioned into groups based on the order of stimuli presentation, when a particular experiment was completed during a set of trials, as well as when it was completed within the experimental session.

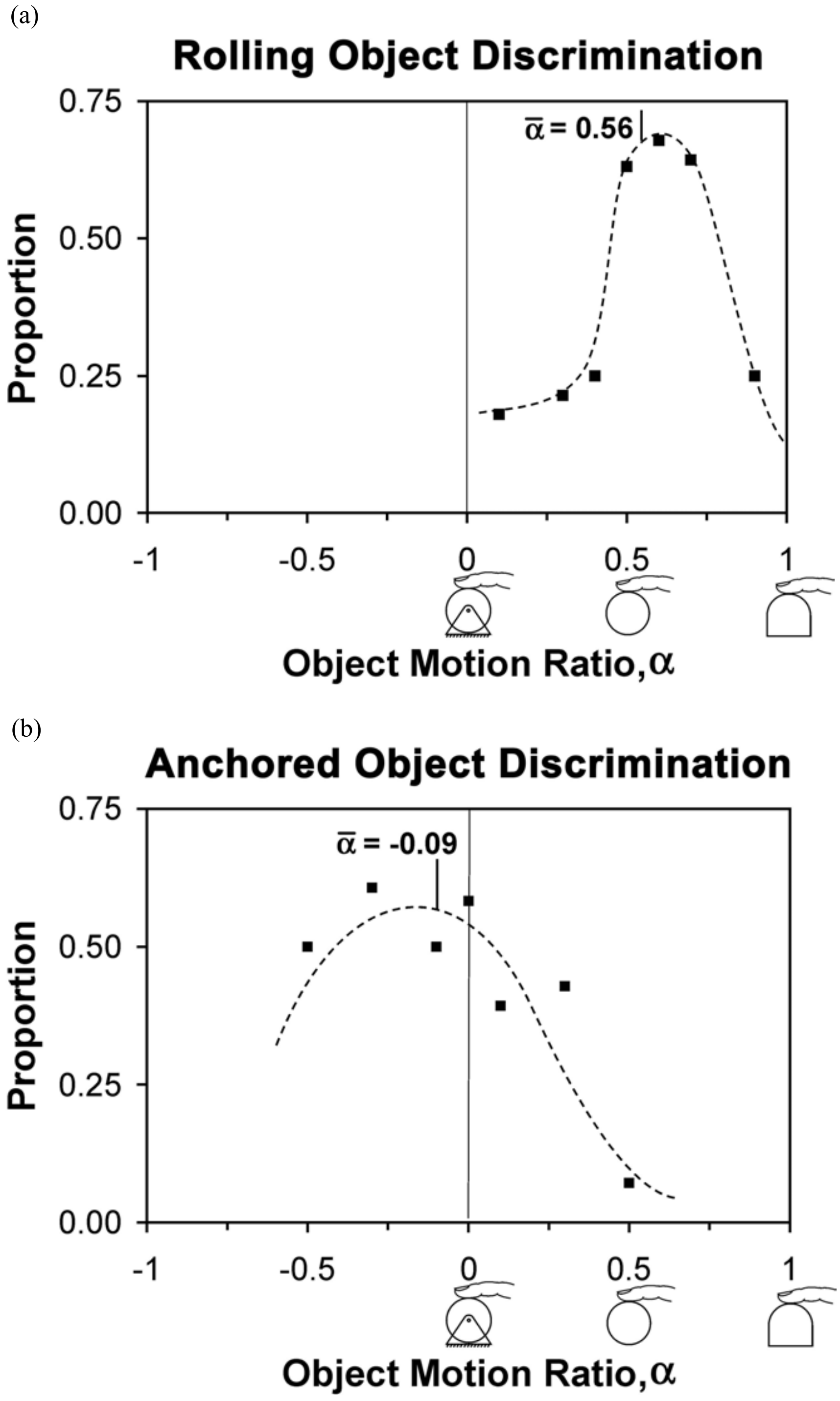

Figure 4-14. The graphs display the proportion of times a given object motion ratio was reported as being (a) rolling or (b) anchored. The means of the rolling and anchored object distributions are 0.56 and -0.09, respectively.

The results of trials in which the motion standards (i.e., $\alpha = 0$ or $\alpha = 0.5$) were presented first were isolated and examined. The data were also partitioned into those trials in which α was increasing and those in which sequential stimuli in each trial involved α decreasing. Statistical analysis of these data revealed that the order of presentation did not have a significant effect.

Trends in subject data were also compared from the beginning versus the end of each set of 12 trials. There were no trends for perception of rolling objects; however, for anchored objects, it was found that many subjects gravitated towards objects with zero or negative α value towards the end of the set of trials. Perhaps this is because some people simply chose objects which most restricted their motion (even if this involved actively moving opposite to their motion).

Subject data were also partitioned into groups based on when a particular set of trials occured. Those completing the motion experiments first were compared to those completing motion experiments at the end of the session. Those completing rolling experiments first were also compared to those completing anchored object discriminations first. In both cases, there was a statistical difference for judgements made of anchored objects between the two groups. Subjects who completed anchored object discriminations later in the experiments more reliably identified a truly anchored object ($\alpha \sim 0$ as opposed to $\alpha \sim -0.1$) compared to those completing anchored discriminations first. Learning is a possible explanation for such behavior.

Beyond the successful discrimination, subjects also commented that this experiment felt realistic. These findings suggest the device forms a promising new approach to tactile display.

4.6 General Discussion and Conclusions

This work has presented a novel device for displaying contact centroid location during haptic interactions. Unlike pin arrays, it is easily mounted on a traditional haptic display and integrated with force feedback.

In controlled experiments, it was found that human subjects could easily use the device to determine the curvature of virtual objects. Moreover, the just noticeable difference (JND) values obtained with the device were comparable to those obtained with physical specimens and direct finger contact. Different trends between virtual and direct contact illustrate slightly different perception modes and lead to increased virtual discrimination for large radii of curvature.

The virtual objects were discriminated with a Weber fraction of approximately 0.11, indicating that users can detect changes in object radius greater than 11%. Based on the motion of the contact point, this finding also implies a tactile length Weber fraction of 0.11.

It was also found that users of the device could identify various types of object motion based on the contact location change, specifically discerning rolling and anchored objects. Anecdotally, subjects reported that they found the sensation of traveling contacts a convincing simulation and a welcome improvement over probing the virtual world with a stylus.

5 Extensions and Conclusions

Through the work presented in this thesis, one only begins to understand what an exquisite instrument the human is. It represents a significant achievement of nature that man may never fully succeed in replicating. However, this thesis makes two small contributions to this effort. This final chapter summarizes the work presented in chapters 3 and 4 on tactile sensing and display, respectively. It summarizes the main contributions of this work and suggests possible extensions and future work.

5.1 Summary of Contributions

The major contributions of this thesis are:

- A new sensor for measuring local object geometry

  This sensor is meant for use in object manipulation tasks where knowledge of local object geometry is essential for object motion planning. In contrast to previous sensors, which either infer object curvature from a nearly rigid sensing array or which lead to complex non-linear problems, this sensor measures curvature directly. The sensor employs standard foil strain gages and circuitry tailored to the task of measuring curvature. The sensor's half-bridge circuitry produces an output signal that is linear with curvature and reduces sensitivity to temperature fluctuations. A mathematical framework was established to reconstruct the sensor geometry via an array of curvature measurements, based on classical Fourier analysis. The sensor is analyzed and its inherent accuracy and sensitivity are determined numerically and in experiments.

- A new approach to tactile display

  This new approach is based on displaying only a single contact representative of the centroid of contacts. Based on previous work in autonomous robotics, knowledge of contact conditions is essential for robotic dexterous manipulation. The goal was to provide a human teleoperator with this same information. A device was developed and tested on a virtual reality testbed, but is also envisioned to be used in telerobotic applications.

- Evaluation of human perception of contact location feedback

  Human subjects performed virtual manipulation tasks to better understand the value of displaying contact location in addition to force feedback. Testing indicated that subjects could easily distinguish between rolling and anchored object behaviors, which correspond to an important state change during manipulation. Experiments also showed that for gently curved objects, subjects' curvature discrimination abilities with the contact display device were comparable to their ability when directly manipulating physical models (for objects about 30 mm in radius, the measured JND was approximately 4 mm).

- Thresholds for cutaneous length-based perception, as used in rolling objects between the fingers, were determined.

  Because only a single point of contact is displayed when representing contact with a virtual object, the judgements made in virtual curvature discrimination experiments are based on the length traveled by the roller. Therefore, these tests have also contributed cutaneous length-based JNDs, not currently available in the psychophysics literature. From experiments, the Weber fraction for cutaneous length based discrimination is approximately 0.11, meaning that subjects could distinguish between a roller travel of 5 mm and 5.55 mm.

5.2 Improvements and Extensions

As with most designs, one learns a great deal from each generation of prototypes. The devices presented in this thesis have evolved considerably since their conception; however, it is clear that many improvements can still be made. The following subsections, outline suggested improvements and possible future work in these areas.

5.2.1 Tactile Sensor

Preliminary tests with the second-generation prototype indicate that future sensors should be packaged to reduce the initial curvature, improving sensor performance (reducing hysteretic error contributions). The feasibility of combining the sensing element and electronics on a single flexible substrate has been shown. However, experience suggests that it is more practical to separate the sensing element from the sensor electronics while in the prototyping stage. Sensor electronics with a suitable flex-circuit connector can be acquired inexpensively from commercial PCB vendors, permitting rapid independent iteration of the flexible sensing element.

The sensor performance could also be improved by modifying the way the sensor is mounted. The initial shape of the sensor was chosen to resemble the robot fingertips currently used for dexterous manipulation (semi-circular). However, superimposing a relatively high initial curvature on the sensor exacerbates sensor hysteresis and ultimately reduces sensor accuracy. Therefore, mounting the sensor element so that its initial curvature is reduced should improve its performance.

Results from calibration testing and thermal modeling also suggest modifying the way the gages are affixed to the substrate. Inhomogenous bonding can lead to mechanical hysteresis and thermal drift. Depositing sensor elements directly on a flexible substrate, rather than bonding prefabricated gages to a flex-circuit, would dramatically reduce sensor hysteresis and extend the dynamic range of the sensor. This would also reduce thermal gradients between the gages. Adopting a substrate with higher conductivity will further improve the sensor's thermal stability. DuPont has developed a special formulation of polyimide, called Kapton$^{\text{TM}}$ MT that has three times the thermal conductivity of standard polyimide, that would be a good candidate substrate for the next generation sensor.

In addition to the above advantages, deposition and photolithography techniques will make it possible to fabricate densely populated sensor elements and associated interconnects. Photolithography and deposition also provide a practical method for producing two-dimensional arrays and vias. One issue that must be addressed when making a two-dimensional array is the sensor's ability to conform to complex geometries. Fabricating the array on a mesh-like substrate may be a solution to this problem. Other solutions may be found in adapting approaches from the clothing and composites industries.

5.2.2 Contact Location Display

The contact location display is a valuable addition to force-feedback for virtual and remote environments. The results obtained thus far suggest that this approach will enable users to determine object geometry and changes in contact configuration during dexterous manipulation. The success also suggests many additional developments, including conversion to two degrees of freedom for display of lateral as well as proximal/distal contact motion. For this incarnation, the tactile element would perhaps become a ball bearing. Other modifications may not be as straight forward. Imparting lateral motions to the tactile element by differentially actuating push/pull wires (similar to those shown in the current 1-DOF design) seems a logical first approach. However, there are several potential issues with this approach derived from the additional degree of freedom. One of the advantages of the current design is that the lateral stiffness of the push-pull wires provides a passive degree of freedom for making and breaking contact with the tactile element. For the two degree of freedom version, it may be difficult to design a linkage with an additional degree of freedom that will still take advantage of the passive stiffness of the push-pull wires to prevent contact of the tactile element with the finger in free space (as shown in Figure 4-4). Thus, it may become necessary to actively control the making and breaking of contact (by the addition of a sensor and/or actuator). In addition, the same compliance of the push-pull wires will also limit the lateral actuation force available to move the tactile element laterally over the fingerpad (this was not an issue for actuation along the length of the finger, since the push-pull wires are aligned with this axis of motion). Therefore, one can see that augmenting the current design with an additional degree of freedom represents a challenging design problem.

Other variations of the current design would be more straightforward to implement. One might consider using a brake to control roller rotation, making it possible to transmit shear forces through the roller similar to those experienced during sliding contact. This provides an exciting opportunity to meld the current work in contact location display with work presented by Salada et al. [2002] on the display of slip for rendering virtual surfaces.

It would also be interesting to use this feature to simulate the skin stretch experienced when sliding a finger over a surface. This could be done by building a mechanical shear model of the finger and commanding appropriate contact positions to compensate for skin stretch based on the direction of travel while in contact.

One might also consider specifically tailoring the design of the tactile element to add functionality or more closely replicate specific surface properties (e.g., surface geometry, stiffness, and/or friction). For example, if medical students were to use contact location display to practice breast examinations, one might imagine constructing a tactile element made of silicone rubber to replicate the mechanical properties of breast tissue. Perhaps the tactile element would also include one or several internal pins to indicate possible subdermal masses. Other designs for multifunctional tactile elements have been envisioned in which one would place prototypical surface features around the circumference of a roller drum, and rotate the drum to the desired position when a particular surface type is desired. For example, a roller might have 3 positions on it that are smooth, textured and with a knife edge to render sliding or rolling over a smooth surface, sliding over a rough surface, and sliding along a sharp edge, respectively. Of course this type of design also necessitates additional actuation.

Ultimately, the goal is to incorporate contact location feedback in a multi-fingered system for dexterous manipulation of virtual or remote objects. The current design can be adapted to this end; however, there are obvious packaging issues with placing several such devices in close proximity. The first issue is the possible mechanical (side-by-side) interference of placing thimbles on neighboring fingers. A similar interference issue occurs when grasping virtual objects. Hardware on the pad-side of the fingers and thumb can possibly collide and/or interfere. Routing of the multiple sets of push-pull wires could also prove challenging.

It would also be interesting to extend the current experimental investigation to better understand what aspects of manipulation the device can best communicate. For instance, in manipulation, the transition from rolling to sliding contact represents an important event. One could imagine coding this event under the current kinematical framework as continuously varying the value of α during a slip event.

Another feature of the device that was not specifically investigated is its ability to make and break contact with virtual objects (as shown in Figure 4-4). Users stated that this feature enhanced the tactile illusion of initiating new contact. However, one might also consider taking this one step further. A typical complaint made of most virtual environments is that they feel as if one is interacting with a "nerf" world. This is a result of objects rendered as linear spring elements and a by-product of limited motor torque. Deficient torque is a serious limitation that hinders one's ability to render stiff interactions. However, one could consider taking advantage of the passive degree of freedom (normal to the finger surface) that exists between the Phantom^{TM} and thimble. One could consider enhancing the perception of a stiff object or object impact by anticipating contact and bringing the roller into contact with the finger with a commanded velocity designed to impede the user's interpenetration into a virtual object (i.e., matched momentum haptic rendering of impact).

5.3 Conclusion

This thesis has described new methods of tactile sensing and display for dexterous dexterous telemanipulation and virtual reality. A tactile sensor was developed specifically to measure local object geometry useful for manipulation planning. A companion tactile display renders the location of the centroid of contact, an important cue about object curvature in manipulation and exploration tasks. Concepts for both devices have been validated with initial experiments that clearly show their potential and shed new light on the human perception of curvature in manipulation tasks.

Appendix A: Sensor Bridge Circuitry and Thermal Modelling

This appendix gives some general background in strain gage circuitry and also presents some results from thermal modeling of the sensor presented in chapter 3.

A.1 Strain Gage Bridge Circuitry

This section presents some basic background for strain gage bridge circuitry that is relevant to the sensor presented in chapter 3. The goal of this sensor is to measure curvature. Since curvature is proportional to bending strain, basic bridge equations are developed with this goal in mind. Figure A-1 shows several configurations which can be used to measure bending strains. The main difference between these different options is the number of strain sensing elements. The simplest possible configuration, the quarter bridge (see Figure A-1(b)), utilizes a single strain gage on one side of the substrate, and is represented in the associated bridge circuit by its resistance, R_1. Here the remaining resistors, labeled R_d, are simply resistors on a circuit board. Keeping the design as simple as possible is desirable. However, there are many potential benefits to using additional gages in the bridge circuit. Some of these benefits are listed at the bottom of Figure A-1. Most importantly, the half-bridge and full-bridge configurations (shown in Figures A-1(c) and (d)) are temperature compensated[1] and reject axial strains, which allow bending strains to be isolated (see Fraden [1996] as well as the comments that follow Equation A.2). Both of these properties are essential for this sensor. In choosing between the half- and full-bridge options, the simpler half-bridge configuration was chosen for the final sensor design. The half-bridge possesses the same key benefits as the full-bridge, but requires only half of the area.

---

[1] These configurations reduce sensitivity to gross temperature fluctuations, but are still susceptible to drift when a temperature differential exists between a gage-pair, as can occur when the substrate has poor conductivity. See thermal modelling results in section A.2.

(a) Standard Wheatstone Bridge

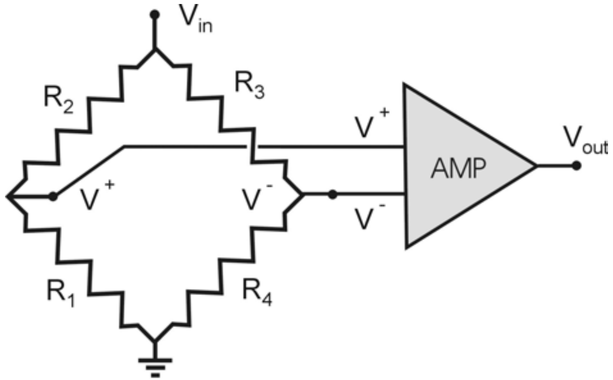

(b) Quarter-Bridge

(c) Half-Bridge

(d) Full-Bridge

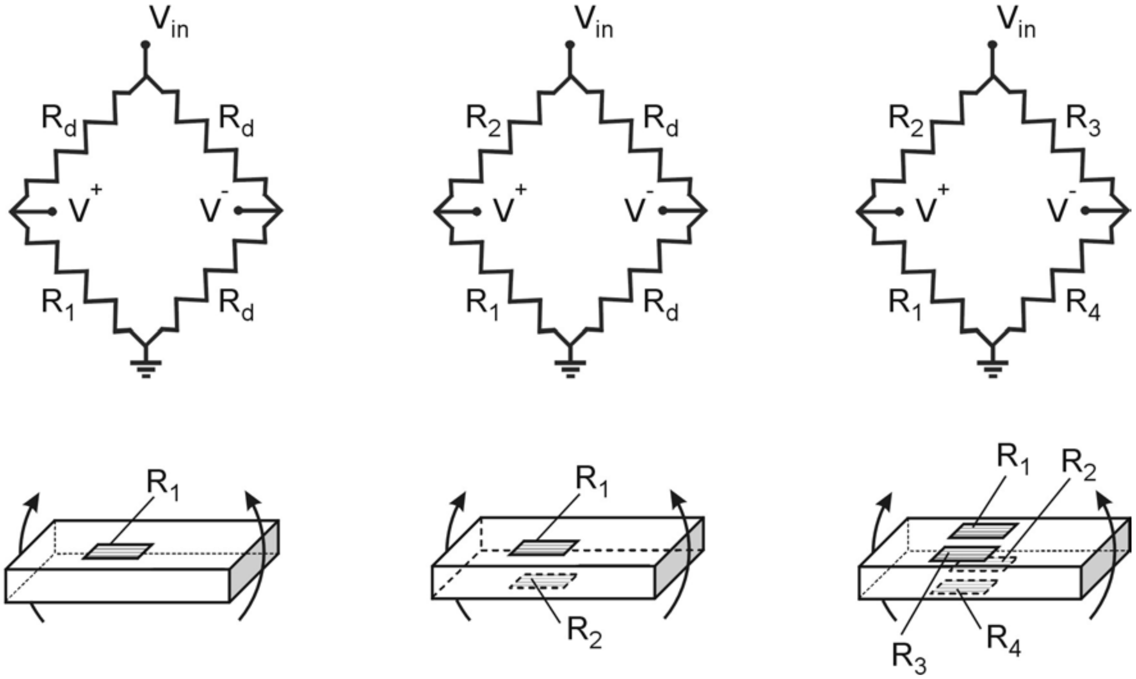

Quarter-Bridge Attributes

Desirable:

- Simplest configuration
  - Minimum number of gages

Undesirable:

- Not temperature compensated
- Sensitive to axial and bending loads

Half-Bridge Attributes

Desirable:

- Rejects axial strain
- Temperature compensated
- Near linear output
- Increased sensitivity over quarter-bridge

Undesirable:

- 2x as many gages as quarter-bridge

Full-Bridge Attributes

Desirable:

- Rejects axial strain
- Temperature compensated
- Near linear output
- Twice the sensitivity of the half-bridge

Undesirable:

- Measures strain at 2 points
- 2x as many gages as half-bridge

Figure A-1. (a) Wheatstone bridge and specialized configurations (b-d) to measure bending strain. A list of attributes are given for each. The half-bridge configuration has many advantages over the quarter-bridge, and requires fewer gages than the full-bridge.

Standard wheatstone bridge circuitry is employed to simplify the challenge of measuring the subtle changes in the resistance of the stain gages. A wheatstone bridge, is simply a clever combination of two amplified voltage dividers (shown in Figure A-2(a)). As such, it is instructive to first examine the behavior of the voltage divider separately. The equation for the output voltage of a voltage divider can be derived from Kirchoff's current law.

$$V^{+} = \frac{R_1}{R_1 + R_2} V_{in} \tag{A.1}$$

Replacing R_1 and R_2 with the resistance associated with a gage-pair, Equation A.1 can be rewritten:

$$V^{+} = \frac{R_g + \Delta R_1}{(R_g + \Delta R_1) + (R_g + \Delta R_2)} V_{in} \tag{A.2}$$

where R_g is the nominal resistance of the strain gages, and ΔR_1 and ΔR_2 are the resulting changes in resistance of the top and bottom strain gages. This equation useful to illustrate some of the desirable characteristics of the half-bridge configuration for sensing bending strains. Arranging the gages in this fashion reduces the circuit's susceptibility to temperature-induced drift and makes the circuit insensitive to axial strains. This is a result of the ratiometric nature of Equation A.2. That is, if both ΔR_1 and ΔR_2 are *both* changed by the *same amount* (such as what might result from uniform heating or axial loads), the ratio remains unchanged (nominally $1/2 \cdot V_{in}$). This is why this bridge configuration is particularly advantageous.

In contrast, if the change of resistance associated with bending in the top (ΔR_1) and bottom (ΔR_2) strain gages, are equal and opposite (due to sensor symmetry). As a result they cancel each other's contribution to the denominator of Equation A.2, leading to the simplified equation:

$$V^{+} = \frac{R_g + \Delta R}{2\ R_g} V_{in} = \left(\frac{1}{2} + \frac{\Delta R}{2\ R_g} \right) V_{in} \tag{A.3}$$

Note that this equation is linear with changes in resistance, ΔR, and consequently also linear with respect to curvature.

Using Equation A.3 and the voltage divider circuit, one could measure the strain in the sensor, but the changes in gage resistance are extremely small and result in very small voltage changes (50 millivolt full scale, with an excitation voltage, $V_{in} = 5$ volts). This is the reason why wheatstone bridge circuitry is used for strain gage measurements. The addition of another voltage divider, allows the DC component ($1/2 \cdot V_{in}$) to be subtracted out of Equation A.3, permitting amplification of the raw voltage signals:

$$V_{out} = (V^{+} - V^{-})\ Gain \tag{A.4}$$

(a) Voltage Divider

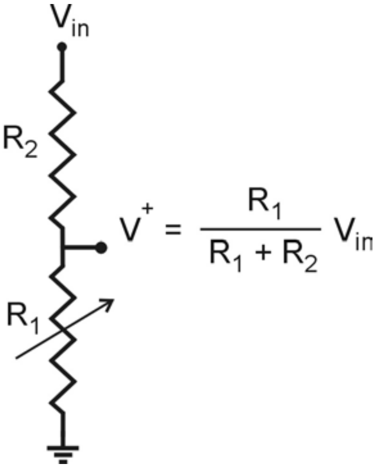

(b) Sensor Half-Bridge Schematic

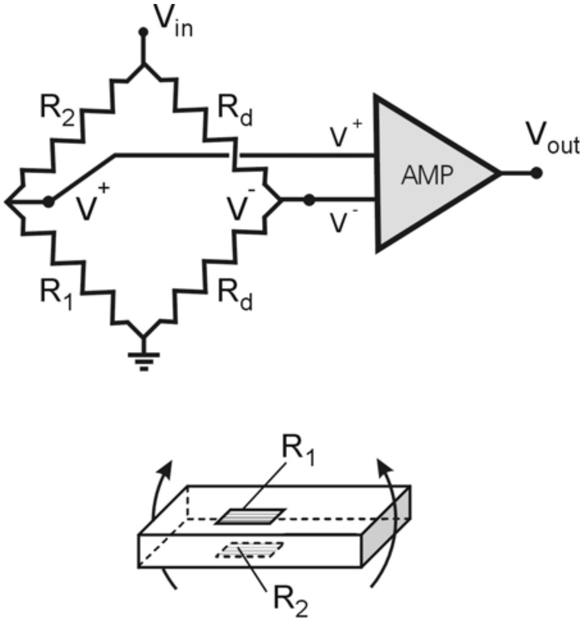

Figure A-2. (a) Voltage divider circuit and (b) half-bridge configuration of Wheatstone bridge used to measure curvature.

where V^+ is unamplified half-bridge output and V^- is the output of a dummy half-bridge used to zero out the bridge circuit (nominally $V^- = 1/2 \cdot V_{in}$). Substituting Equation 3.13 (the change in resistance associated with bending strain) into Equations A.3 and A.4 yields the final bridge equation for measuring bending strains with a pair of back-to-back gages wired in a half-bridge configuration (shown in Figure A-2(b)):

$$V_{out} = \frac{V_{in} \cdot GF \cdot (t_s + t_g) \cdot Gain}{4 r_{ave}} \tag{A.5}$$

where V_{in} is the bridge excitation voltage, rave is the mean radius of curvature of the membrane centerline, t_s is the thickness of the membrane substrate, t_g is the gage thickness and "Gain" is the bridge amplification. Equation A.5 can be rearranged in terms of average curvature, κ, where curvature can be shown as the reciprocal of radius of curvature and κ(i) represents the curvature of the i^{th} gage-pair.

$$\kappa(i) = \frac{1}{r_{ave}} = \frac{4 V_{out}}{V_{in} \cdot GF \cdot (t_s + t_g) \cdot Gain} \tag{A.6}$$

A.2 Sensor Thermal Modelling

As mentioned in section 3.3, it is important to consider thermal effects in the performance of piezoresistive sensors such as the one presented in this thesis. A thermal model of the sensor was developed to help understand environmental effects. This model is quite simple, but is useful as a tool for investigating possible sources of thermally-induced imbalance in a gage-pair of a half-bridge. This is particularly important because thermal drift is consistently a major source of error in piezoresistive sensors.

A.2.1 Thermal Modelling Results

This section presents results that were generated using the thermal model presented in section 3.3. Several scenarios were investigated to help understand the sensor's sensitivity to temperature. These models focus on predicting the differential temperature between gages in a single gage-pair. Material properties and parameter values used to generate these results are reported in Tables A-1 and A-2. The power input for the thermal model is 3.0 mW, which corresponds to the excitation voltage of 1.2 volts and a gage resistance of

Table A-1. Material properties relevant to sensor thermal modeling.

Material	Specific Heat, c (J/Kg °C)	Conductivity, k (W/m °C)	density (Kg/m^3)	TCR[a] (ppm/°C)
Constantan	397	22	8800	10
Kapton^{TM}	1090	0.1-0.35	1400	N/A
Silicone Rubber	1300	0.2	1120	N/A
Adhesive	1100	0.42		N/A
1% metal film resistor	N/A	N/A	N/A	100

---

a. TCR is the temperature coefficient of resistivity and describes the change of resistance with changes in temperature.

120 ohms. It should be noted that the results presented here are only meant to be representative of trends in performance. If a high degree of accuracy is required, the model would require detailed correlation to experimental data.

A.2.1.1 Sensor Warm-up with Asymmetric Boundary Conditions

As a consequence of asymmetry in thermal boundary conditions, a small temperature differential appears during sensor warm-up. As shown in Figure A-3, the model predicts an exponential rise in temperature for both gages, with a steady state temperature differential of 0.14°C. Assuming that the gage resistances are perfectly balanced before applying an excitation (also assumed when looking at the scenarios presented in the following sub-sections), only the differential temperature is of primary concern. The small temperature differential causes a resistance imbalance in Equations A.2 and A.4. Based on the temperature

Table A-2. Parameter values used in thermal models.

Parameter	Thermal Resistance, R[a] (°C/W)	Parameter	Thermal Capacitance[b] (J/°C)
$R_{sub,X1}$ & $R_{sub,X2}$	25.6	$CR_{sub,Y}$	2.0e-3
$R_{sub,Y}$	8000	$C_{skin,Y}$	5.8e-3
$R_{skin,X1}$	38.4		
$R_{skin,X2}$	760		
$R_{skin,Y}$	400		

---

a. The thermal resistance, R, is a function of the conductivity, k, and conduction path length and area, L and A, respectively. R = L/(k•A)

b. The thermal capacitance, C, is related to the specific heat, c, by the formula: C = c•m, where m is the mass.

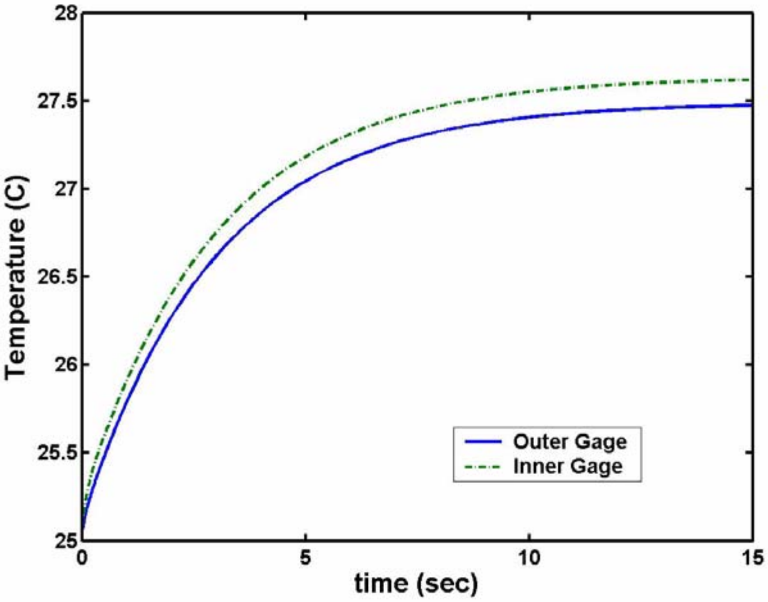

Figure A-3. Sensor warm-up from ambient (25°C). A slight temperature differential between the inner and outer gages results from asymmetric thermal boundary conditions. This asymmetry is a result of the protective silicone rubber skin on the sensor. The steady-state temperature differential is 0.14°C.

coefficient of resistivity (TCR) for constantan (shown in Table A-1), the resistance differential is 0.168 mΩ and will therefore result in an induced voltage of 0.31 mV (based on Equation A.2 and an amplifier gain of 880x). This would lead to a false curvature signal of $2.4 \times 10^{-3}\ m^{-1}$ (quite small). However, one would expect that the sensor would be calibrated after it is warmed up, so even this small inaccuracy can be eliminated.

The scenarios investigated in the following subsections all assume that calibration occurred under the nominal conditions presented in this section. Therefore, the 0.14°C differential that occurs during sensor warm-up will be subtracted from the calculated temperature differentials in the following subsections.

A.2.1.2 Imbalance in Gage Resistance

There are always small variations in the actual resistance value associated with a strain gage. The variations in resistance observed for this sensor are quite small (less than 2 Ω). For the purposes of illustrating the effect that a resistance differential will have on the output of the sensor, a differential of 5 Ω will be considered. This imbalanse results in 0.13mW of extra power dissipation through one of the gages (assumed to be the inner gage as a worst case scenario). The transient rise still resembles that shown in Figure A-3, but

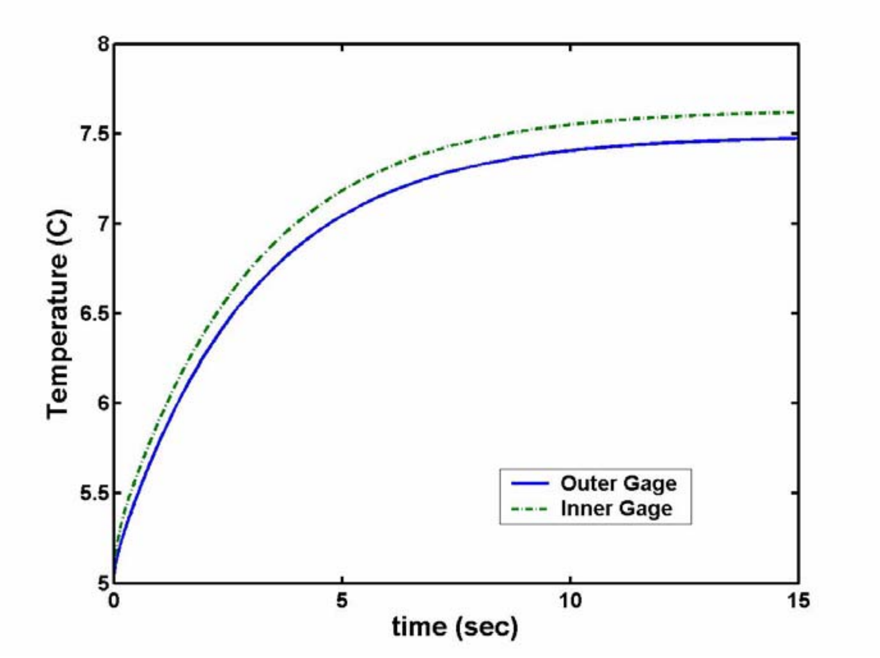

Figure A-4. Effect of operating the sensor at 5°C. This has little effect on the steady state temperature differential, which is 0.14°C. However, there are other consequences that should be considered (see discussion in section A.2.1.3).

the temperature differential is increased by 0.01°C. This results in a false curvature offset of 1.7 x 10^{-4} m^{-1} (a negligible amount).

A.2.1.3 Operating Sensor in Cold Environment

It is also important to consider the effects of operating the sensor in environments that are hotter or colder than typical. Figure A-4 shows the temperature rise during warm-up when used at an ambient temperature of 5°C. Though the steady-state operating temperature is much lower, the temperature differential is exactly the same as presented in the previous subsection and no imbalance is expected. However, there are several other consequences of operating at a lower temperature.

The gage factor for constantan has a nominal value of 2.1, but its value is temperature dependent. Based on specifications provided by Vishay's Measurements Group, the gage factor can change by about a quarter percent as a result of a 20°C drop in operating temperature. This directly affects the sensor gain, causing a 0.26% loss in sensitivity.

In addition to its effect on the gage factor, the cold will also decrease the value of every resistor in the sensor as well as the reference diode, which regulates the excitation voltage. This will not only affect the excitation voltage and amplifier gain, but also the self-heating characteristics of the gages.

The nominal value of the gain resistor on the instrumentation amplifier is 56 Ω, resulting in a gain of approximately 880x. Since this resistor has a TCR[2] of 100ppm/°C, the resistor value is reduced by only 0.11 Ω due to the 20°C drop in operating temperature. This amount of change will reduce the amplifier gain by about 0.18%.

The data sheet for the reference diode (LM4051) shows that the diode will drift slightly as a result of changing temperature. For a 20°C decrease in temperature, the reference voltage will drop an estimated 0.4 mV. For a nominal operating voltage of 1.216 volts, this represents a 0.033% loss in sensitivity.

Finally, the small change in resistance of the gages as a result of the 20°C decrease in temperature will lead to an increase in power dissipated though the gages. This change in resistance is approximately 0.024 Ω and results in an increase of power dissipated

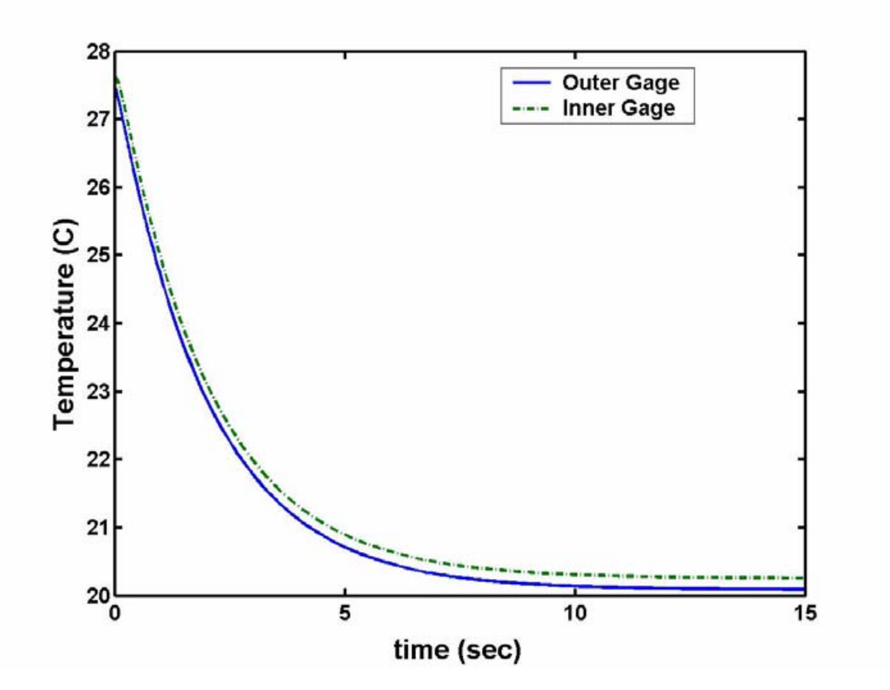

Figure A-5. Effect of touching a cold (5°C) object. This has only a slight effect on the temperature differential between the gages. The steady state temperature differential is 0.17°C, only a 0.03°C difference from nominal (refer to Figure A-3 for nominal warm-up).

---

[2] TCR = temperature coefficient of resistivity.

through the gages of 0.8 μW. As shown in the previous section, this will have a negligible effect.

A.2.1.4 Contact with a Cold Object

It is also important to consider how contact with a hot or cold object will affect the output of the sensor. Figure A-5 shows the response of the sensor when coming into contact with a cold object (5°C). As shown, the operating temperature of both gages is reduced by approximately 7°C. However, this results in only a 0.02°C differential in temperature between the gages. This leads to an induced voltage of 44 μV or, equivalently, a false curvature signal of 3.5 x 10^{-4} m^{-1}, a very small effect.

A.2.1.5 Inhomogeneous Substrate Conduction

A large concern in manufacturing the sensor is homogeneity of bonding and construction of the sensor elements. Not only will this affect the mechanical performance of the sensor, but it will also affect its thermal performance. To investigate this issue, the thermal model was altered to represent a bad thermal joint between the gages and the substrate (as might happen if the gage locally delaminated from the substrate). To do this, the value of the resistance between the inner gage and the substrate, $R_{sub,X2}$, was increased by an order of mag-

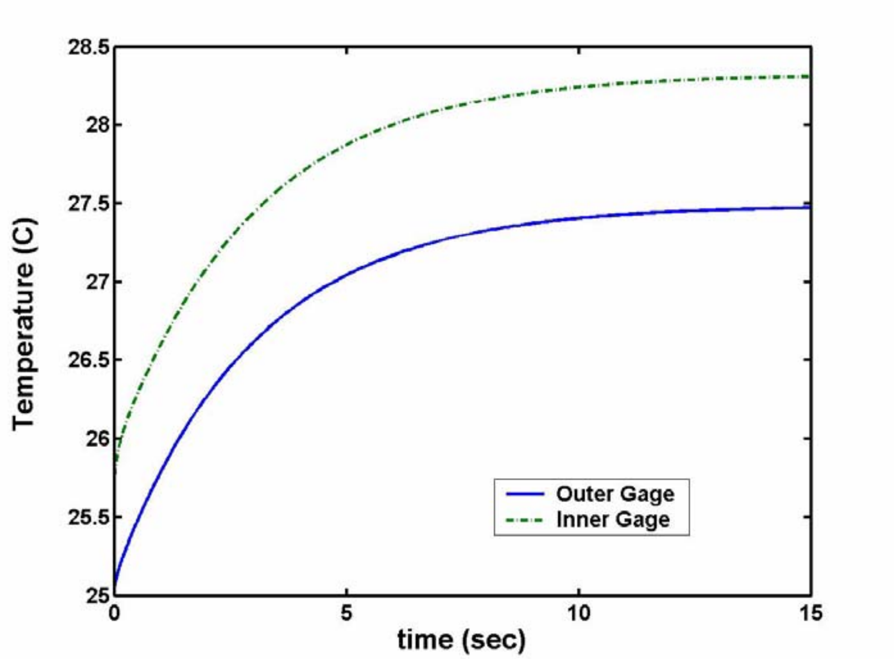

Figure A-6. Effect of increasing the thermal resistance of the inner gage heat flow into the substrate by tenfold has only a slight effect on the temperature differential between the gages. The steady state temperature differential is 0.84°C. This is 0.7°C difference from the nominal warm-up temperature imbalance (refer to Figure A-3 for nominal warm-up).

nitude (altering $R_{sub,X2}$ represents the worst case scenario). As shown in Figure A-6, this leads to an additional temperature differential between the gages of 0.7°C, an induced voltage of 1.54 mV or, equivalently, a false curvature signal of 0.012 m^{-1}. This makes a much larger contribution than many of the other sources of thermal imbalance.

A.2.2 Summary of Thermal Modelling Results

The simple thermal model presented herein makes a useful tool for examining thermal effects for this sensor. In agreement with actual sensor behavior, the model predicts a small temperature rise during warm-up that is on order of a few degrees. In examining the scenarios presented in section A.2.1, there are three main design factors that greatly affect the sensor's ability to maintain relative immunity to thermal effects. These factors are: (1) the conductivity of the substrate ($R_{sub,Y}$), (2) bonding of the substrate to the gages ($R_{sub,X}$), and (3) thermal isolation provided by a protective skin ($R_{skin,X2}$).

The most important design factor is the substrate. The substrate must have good thermal conduction in order to dissipate heat and reduce temperature gradients between the gages. In addition, it is also extremely important that the thermal interface between the substrate and gages is homogeneous. Slight variations, or worse, a partial delamination can lead to temperature differentials that can induce spurious signals of considerable magnitude. The third of these factors is the insulating protective skin, such as the silicone rubber skin chosen for the sensor. The protective skin reduces heat transfer from the environment and thus reduces internal thermal gradients.

Contributions of the most significant thermal effects are listed in Table 3-2.

Appendix B: Contact Location Display Design Details

The design of the device for displaying contact location reported in chapter 4 was the result of many iterations. This appendix outlines some of the previous device iterations and provides more details of the current design.

B.1 Early Prototype Designs

As with many designs, the initial proof-of-concept prototype was produced by modifying an existing product. The initial prototype used the linear actuator from a 3.5 inch floppy

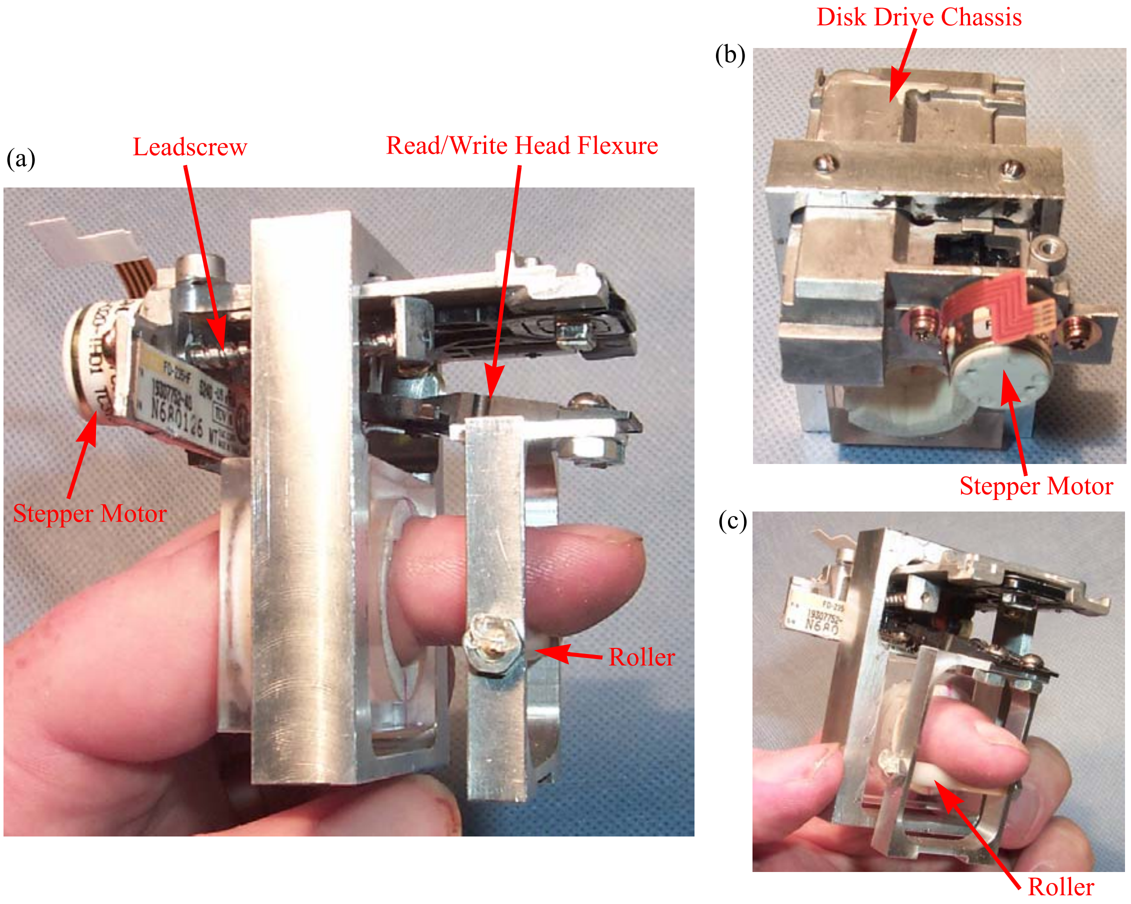

Figure B-1. Proof of concept prototype made from a 3.5 inch floppy disk drive mechanism. (a) Side view of device. The actuator is grounded to the middle phalynx of the index finger by a foam lined ring. The picture shown in (b) provides a view of the device from the top and back sides and (c) provides a view of the device from the front.

disk drive. Figure B-1(b) shows the portion of the disk drive chassis that was cut away from the rest of the disk drive, leaving only the portion necessary to support the linear actuator mechanism. A simple bracket was designed to mount the actuator to the middle phalynx of the index finger, and a small bracket was used to suspend a small roller off the arm originally used to support the read/write head. A small torsion spring on the arm supporting the read/write head provided a preload force to keep the roller in contact with the user's finger as it flexed or extended. The disk drive's bipolar stepper motor provided a simple means to drive the motion of the actuator (using a standard stepper motor driver chip like a MC3479); however, pulses of the stepper motor produce a buzzing sensation that rapidly numb the receptors of the user's fingertip. Other issues included somewhat clumsy ergonomics and insufficient motor torque that caused the actuator to lose steps. Despite these issues, this prototype did demonstrate the potential of displaying contact location, and soon after its completion, work began on a custom-designed device that would address the shortcomings of this simple prototype.

The subsequent design (see Figure B-2) was also mounted to the middle phalynx of the index finger (a second unit was also envisioned for the thumb to permit use with the lab's two-fingered telemanipulator). This device was designed to fit a wide range of finger sizes. This was accomplished by designing the device such that it could be mated and demated to interchangeable rings that could be custom designed to the dimensions of the user's finger. This interface also provided a natural pivot for the device that is coincident with the axis of rotation of the distal interphalangeal joint. This pivot provides a degree of freedom for the roller to follow the contour of the finger as it is flexed or extended during manipulation tasks. It also provides a degree of freedom to make and break contact with the user's finger. It was envisioned that the device would be used in combination with Immersion's CyberGrasp. A torsion spring provides a small moment that moves the roller away from the user's fingertip (see Figure B-2(a)). Force applied through the cables of the CyberGrasp counteracts the moment of the spring and brings the roller into contact with the finger.

Like the design presented in chapter 4, this device employs a linear actuator to position a small roller along the user's fingertip. The device is grounded to the finger using a ring produced through Fused Deposition Manufacturing (FDM), lined with foam, and covered with lycra/spandex cloth. A small leadscrew drives the roller back and forth over the operator's finger using a DC servo-motor, encoder, and PD controller.

This design represents a quantum improvement over the previous prototype, but several issues still plagued this design. For instance, use of the servomotor eliminated the

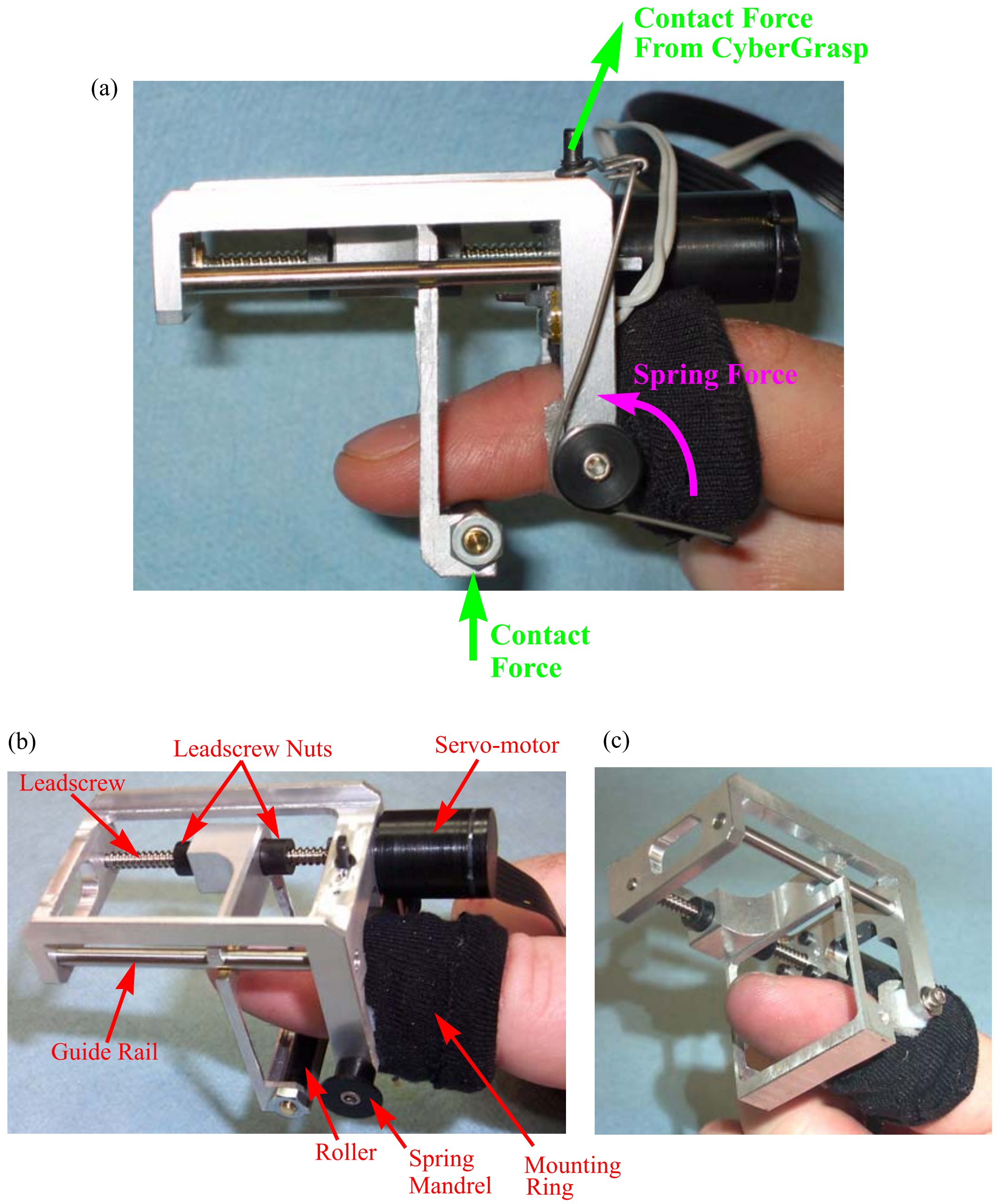

Figure B-2. Custom prototype of contact location display mounting to middle phalynx of index finger. (a) Side view of prototype shown with longer motor for increased torque and torsion spring to apply contact force for the roller. (b) and (c) show the device from alternate angles.

pulsing of the stepper motor, but other harmonic noise, due to bearing misalignment on the leadscrew, cropped up in its place. This issue is normally mitigated using a flexible coupling between the motor and leadscrew, but space limitations made this impractical to incorporate in this design. One of the other main problems was in balancing the moments of the torsion spring and cable force of the CyberGrasp. Part of this issue is a result of changing cable orientation as the user's finger is flexed. There were also several other minor issues with this design, but ultimately the design was abandoned because it would be too difficult to guarantee the desired fit and function across a range of users that would be necessary to validate the feedback concept experimentally.

B.2 Details of Current Design

The design of the device presented in chapter 4 corrects many of the shortcomings of the designs shown in the section above (prototype shown in Figure B-3 below). One of the main differences from the previous designs is that the current design is grounded to the finger at the distal rather than the middle phalynx of the user's finger. This is a change that can be credited to fellow Ph.D. student, Sean Bailey, for suggesting. The other main difference is that the actuator was relocated from the fingertip to the user's wrist, and push-pull wires are used to couple its motion back to the user's fingertip. This is an adaptation to a design that my advisor, Mark Cutkosky, suggested for a 2-DOF version of the device. The following sub-sections provide some of the details of the current design.

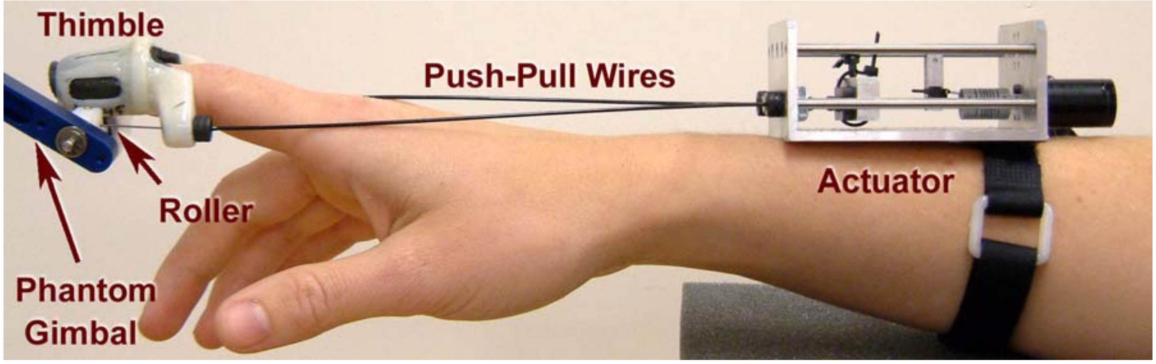

Figure B-3. a) Prototype of the contact location display. The roller is attached to a commercial force-feedback device to provide reaction forces to the finger. A small servo-motor provides precise positioning of the roller via push-pull wires. The roller is suspended below the finger, only touching the user when interaction forces are displayed by the Phantom^{TM}.

B.2.1 Actuator Assembly

The actuator design evolved directly from the previous prototype and uses many of the same components. Unlike the previous design, where great effort was made to reduce the mass of the device, this was no longer as critical since the actuator is situated on the user's wrist. This meant that the outer frame of the actuator bracket could be cut from a standard 1/8 inch wall 6061-T6 aluminum box-beam. The actuator was powered by a small DC servo-motor (MicroMo, part # 1524T006SRIE2-512) which was coupled to an 1/8 inch diameter leadscrew with a lead of 0.075 inch/revolution (Kerk Motion Control, part # NTBF2.1075T x 3inches) by a small flexible coupling (HeliCal, part # ACR037-3-1.5mm). This coupling significantly reduces the effects of small misalignments of the lead screw (both in bearing misalignment and shaft orientation and straightness). Radial loading in the leadscrew shaft is supported at one end by the motor bearings and at the other end by a small ball bearing assembly (Small Parts Catalog, part # A7Y55-G1809) press-fit into the aluminum frame. These particular bearings have an inner race that extends outboard on either side of the bearing assembly that made it possible to use a standard collar to restrain the axial motion of the leadscrew. A small shoulder was cut into the leadscrew on one side

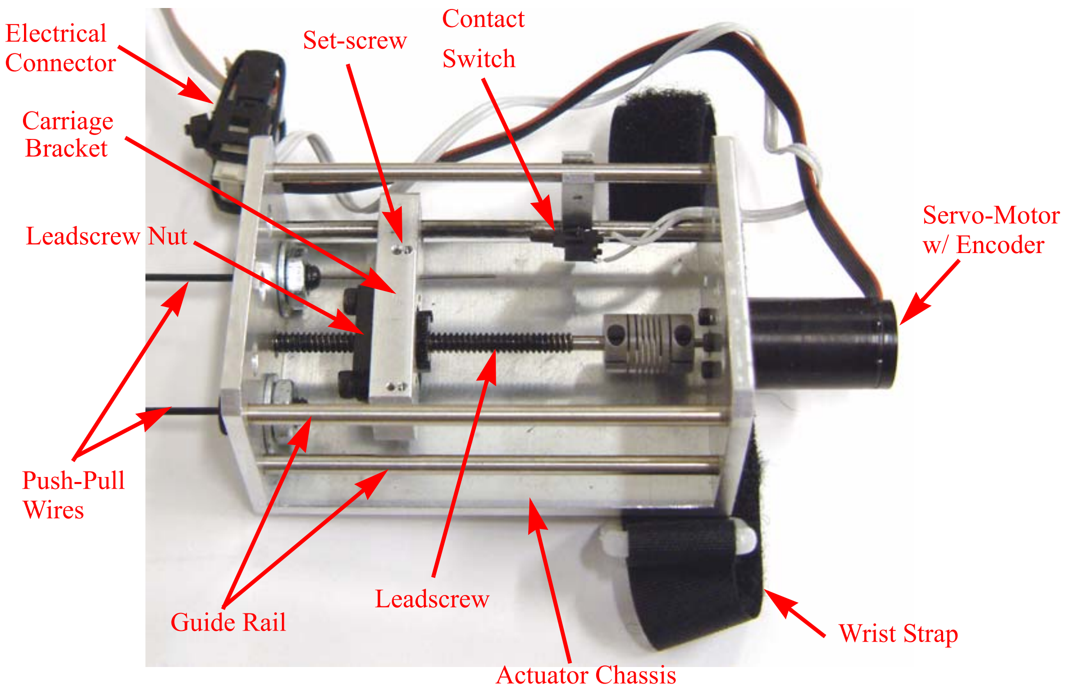

Figure B-4. Actuator assembly. A leadscrew couples the motion of the motor to the push-pull wires. The device is calibrated by driving the carriage against a small contact switch at startup.

of the bearing to restrain motion along the length of the leadscrew in one direction, while the collar captures motion in the opposite direction so that axial loads are carried through the press-fit bearing rather than the motor bearings.

The rotary motion of the motor is converted to linear motion using a standard flanged leadscrew nut (Kerk Motion Control, part # BF2.1075N) that is in turn bolted to an aluminum carriage bracket. This bolted interface permitted easy interchanging of different pitch leadscrew/nut combinations for fine tuning device performance. The carriage bracket couples the linear travel of the leadscrew nut to the two push-pull wires. The connection to the leadscrew shaft locks down all but the rotational degree of freedom (about the leadscrew shaft) of the carriage bracket. This degree of freedom is restrained by 1/8 inch diameter polished guide rail on which a machined slot in the carriage bracket rests.

Small 0-80 set-screws were used to lock the position of the push-pull wires to the carriage bracket, allowing easy adjustment of the push-pull wires. The push-pull wire assemblies were grounded to the actuator chassis by a threaded (10-32) interface. External machine nuts were used to fasten this interface rather than threading the through-hole in the chassis (or using nut plates) because the wire assemblies needed to be free to rotate to permit interchanging of thimbles. Because of this arrangement, one only needs to loosen these nuts when interchanging thimbles.

A small contact switch is used to calibrate the actuator encoders upon startup. This switch is mounted to a small bracket whose position can be adjusted along the length of the 1/8 inch diameter guide rails. The switch, although compact, has a relatively long 0.1 inch stroke before bottoming out. Consequently, there are no hard collisions during calibration. The switch was scavenged from an old HP floppy drive.

B.2.2 Thimble Assembly

The thimble assembly was designed to accommodate a wide range of finger sizes. It accomplishes this goal by making use of custom designed thimbles, each which include a threaded interface to the push-pull wires for interchangeability. The assembly consists of a thimble and roller carriage (see Figure B-5). The roller carriage provides the mounting point for the Phantom^{TM} in addition to housing the roller. Small 0-80 set screws allow the roller carriage to be detached from the push-pull wires. The version of the roller carriage shown below also houses a small pneumatic cylinder, used to prevent the rotation of the roller.

B.2.2.1 Thimble Design

To meet the goal of fitting a wide variety of finger sizes, the thimbles were designed to be interchangeable. Fused Deposition Modeling (FDM) was employed to make the prototypes, which made it possible to produce an entire family of ergonomically designed thimbles. The ergonomic shape and design of the thimble was inspired by a Stanford Product Design student, Eric Schultz. He developed the detailed solid models of an index finger off which the thimble designs were built.

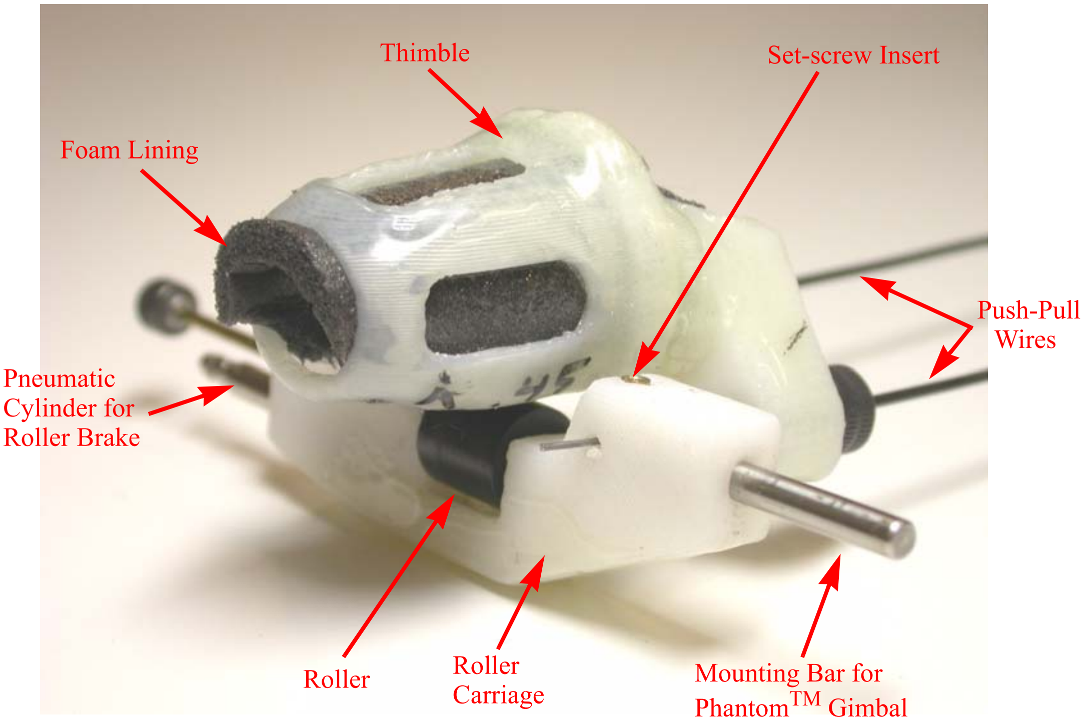

Figure B-5. Thimble assembly. The thimble was produced by FDM and coated in epoxy. It is lined with foam for comfort and to accommodate small variations in user’s finger sizes.

Table B-1. Percentile fingertip sizes (source: The Measure of Man and Woman [Dreyfuss 2002]).

	1st Percentile	50th Percentile	99th Percentile
Men's index fingertip			
Width at distal knuckle (inches)	0.60	0.72	0.84
Thickness at distal knuckle (inches)	0.49	0.61	0.73
Women's index fingertip			
Width at distal knuckle (inches)	0.52	0.61	0.70
Thickness at distal knuckle (inches)	0.42	0.51	0.60

The thin-walled ABS models which emerge from the FDM machine are too brittle to be used directly; however, by painting them with ordinary 5-minute epoxy they are transformed into the tough prototypes that were used with the display device. Cutouts were added to the top and sides of the thimble to improve breatheability.

Each thimble was lined with thin PVC foam tape (from Gaska Tape Inc.), both for comfort as well as to accommodate small variations in finger size. Empirically it was found that 0.080" 8 lb/ft^3 PVC foam provided a good compromise for fit and comfort (7 lb/ft^3 tape becomes permanently compressed, so the fit continues to change over its lifetime). The original intention was to vary the size of the thimble and use the same foam thickness in all thimbles. However, the thimbles used in the experiments all had the same cross-section with varying foam lining thickness to accommodate different finger sizes. These thimbles spanned a range from the 1st percentile up to approximately the 90th percentile man, or, equivalently, from just under 50th percentile up to the 99th percentile woman [Dreyfuss 2002], with tape that ranged from 1/16 inch up to 3/16 inch thick (see Table B-1).

One other critical dimension in the design is the vertical offset between the underside of the user's finger and the roller. During testing, it was necessary to use thimbles with various offsets to prevent false roller contacts. The nominal value of the offset dimension between the thimble centerline and the centerline of the push-pull wires was 0.45 inches (as indicated in Figure B-6), though this varied from 0.40 inches up to 0.475 inches for the thimbles used during testing (a collection of thimbles is shown in Figure B-7). An orthographic layout of the thimble design is shown in Figure B-6, which includes key dimensions.

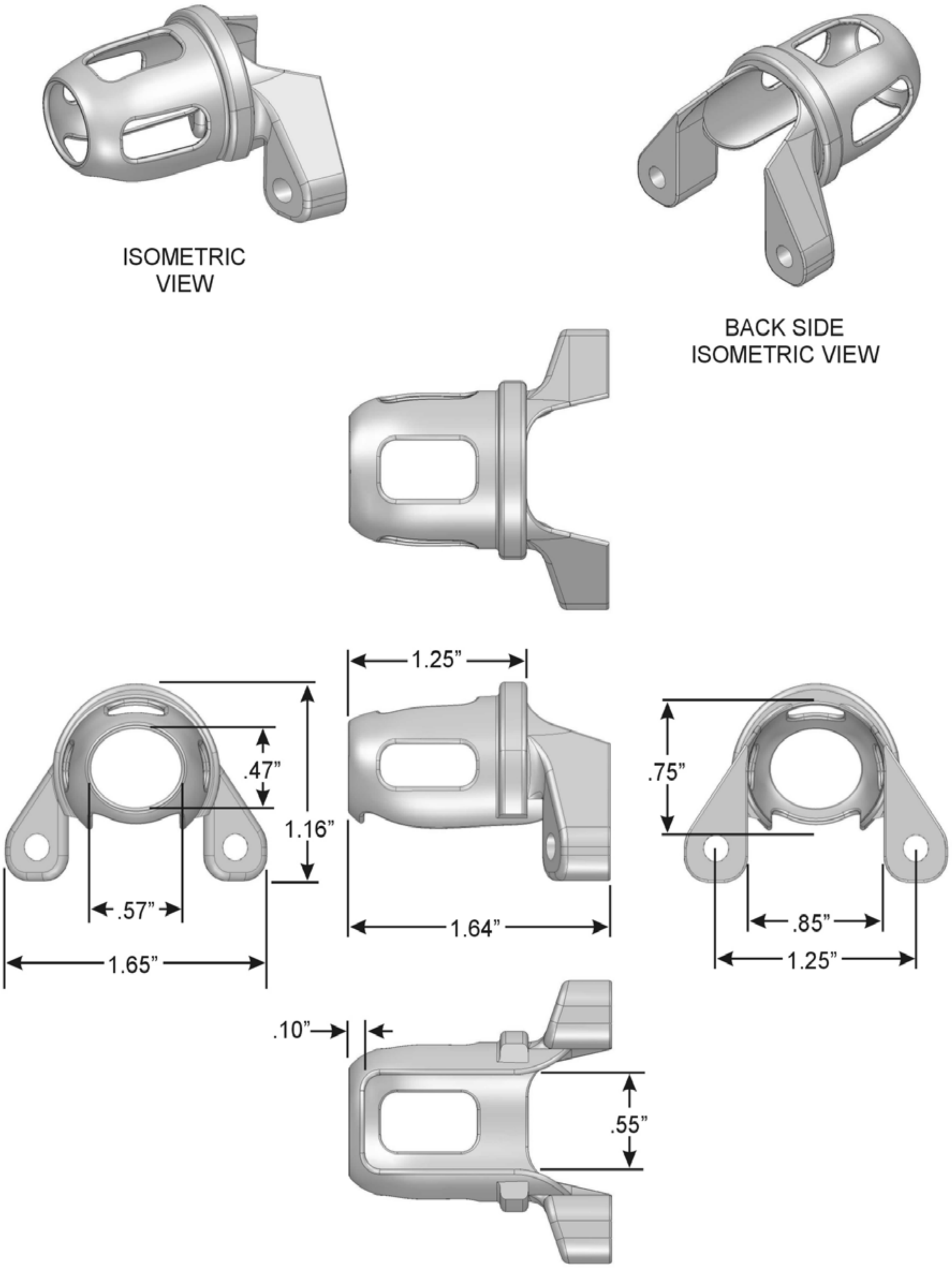

Figure B-6. Orthogonal layout of thimble design with relevant dimensions.

Figure B-7. A family of thimbles were used to accommodate the wide range of finger sizes. The thimbles are lined with 1/6 inch, 1/8 inch, or 3/16 inch PVC foam tape. The thimbles also differ based on the vertical offset from the bottom of the user's finger to the centerline of the push-pull wires.

B.2.3 Push-Pull Wire Assemblies

The push-pull wire assemblies work much like the brake and shifter cables on a bicycle. However, instead of stranded steel cable, the present design uses solid spring wire to prevent buckling during pushing motions. Several options for the push-pull wire assemblies were considered. Each of these designs were similar, utilizing steel spring wire with a plastic jacket, with either end of the plastic jacket terminated by center-drilled socket head cap screws. Terminating these assemblies with a standard threaded interface permitted initial fine tuning of the wire assemblies and interchangeability of thimbles to accommodate a wide range of finger sizes. The threaded interface also simplified device maintenance.

Initially, standard nylon-jacketed assemblies from Carl Stahl Sava Industries, Inc. were considered (eg., part # C-130N which includes a 0.032 inch diameter stainless steel wire and 0.130 inch O.D. nylon sheath). This drove the initial sizing of the threaded interface which terminates the wire assemblies. It was determined that a 10-32 cap screw would be required for the 0.130 inch diameter hole which would accommodate the nylon sheaths. Conveniently, the nylon sheaths were stiff enough to be press-fit into the cap screws without restricting the motion of the internal wires. However, there was a small problem with these wire assemblies. Their large diameter made them very stiff, which required the user to overcome the inherent stiffness of the push-pull sheaths when flexing their finger.

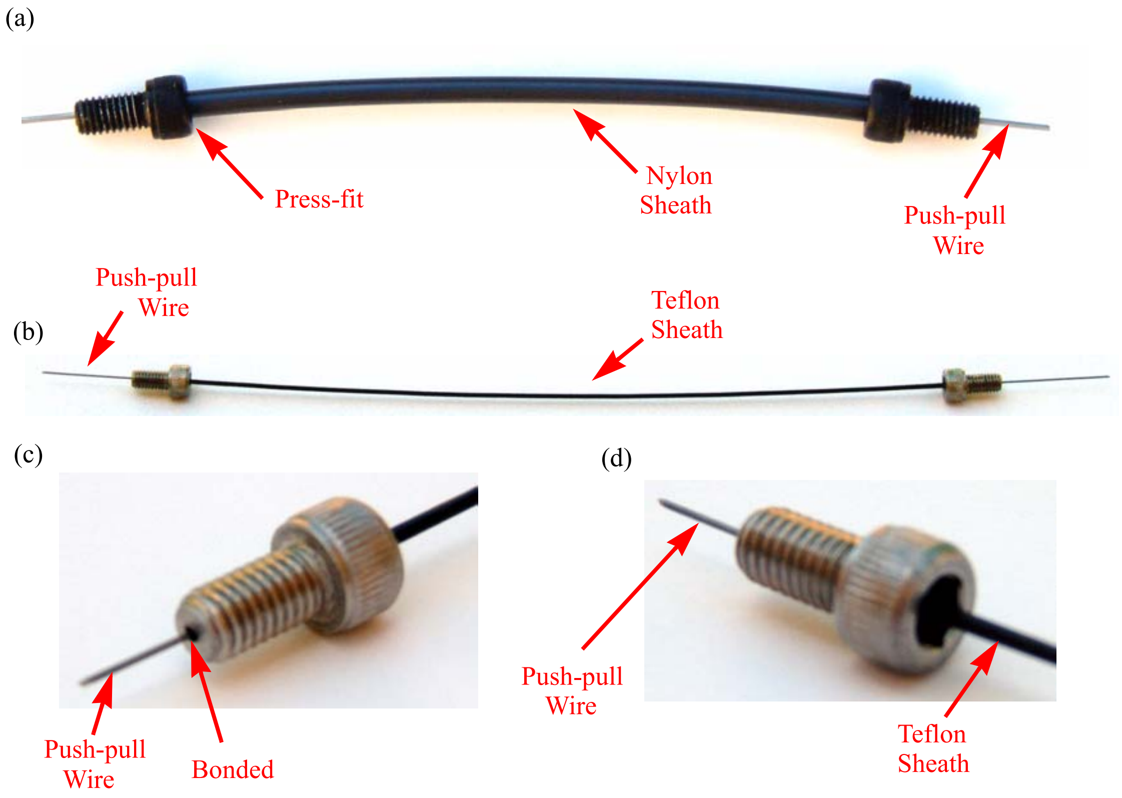

Figure B-8. Push-pull wire assembly. (a) Sava push-pull wire assembly. The ends of the nylon sheath are press-fit into center-drilled 10-32 cap screws. (b) Custom designed push-pull wire assembly with teflon sheath. The center-drilled cap screws were bonded to the ends of the Tefon® sheaths. (c) and (d) show a close-up of the sheath bonded into the center-drilled 10-32 cap screws.

Though it was possible to preshape the nylon sheaths to minimize this effect, the mobility of the user's finger was still greatly restricted.

As an alternative to the thicker nylon sheathing, Teflon® tubing was substituted. Thin Teflon® tubing is available at most larger electronics stores. A variety of wire and sheath sizes were experimented with before settling on 0.024 inch diameter music wire in combination with 22 AWG teflon tube (.027 inch I.D.). However, there was an issue joining the thinner teflon tubing to the cap screws. The tubing collapses when trying to press fit it into the cap screws, causing the wires to bind in this area. The natural solution would be to drill a larger hole in the cap screw and bond them together, but it can be quite difficult to bond anything to Teflon®. However, there is commercially available product, made by the Measurements Group called Tetra-Etch, specially made to treat Teflon® for bonding. After etching, the sheaths were bonded to the cap screws with standard 5-minute epoxy.

Eliminating the press-fit attachment to the cap screw greatly reduced sliding friction. The teflon wire assemblies were also internally lubricated with oil to further reduce friction.

B.3 Device Performance

The dynamic performance of the contact display device was evaluated with the device worn on the index finger and wrist and attached to the Phantom^{TM} as shown in Figure 4-3(b). The device was evaluated in this configuration to account for any effects that the inertia of the user's hand might have on overall system performance.

Figure B-9 shows plots of the device evaluated under various conditions. The response to both sinusoidal and step inputs were recorded. Ideally, a human hand would provide the forcing function for dynamic evaluation, but there are several practical reasons why this was not possible. However, a plot showing the tracking error when rendering a stationary object (as was done in the object motion experiments in section 4.5) is shown in Figure B-9(a). This plot shows the tracking behavior for hand motions with an amplitude of about 1 cm, from 0.5 Hz up to 2 Hz. In this range the device continues to track quite well. Data were also recorded up to about 5 Hz hand motion (with ~1 cm peak-to-peak amplitude), though it was difficult to move at this rate with any repeatability. Nonetheless, even this rate was well within the bandwidth of the device (i.e., the tracking amplitude had not dropped below the -3 dB point). The remainder of the dynamic characterization was performed by programming a forcing function for the device (roller) motion worn on a stationary hand.

Figure B-9(b) shows the device response to a 2 mm step input. The response is slightly underdamped with a 50 ms rise time. On close inspection, slight oscillations can be observed during the rising response. These are most likely a result of the compliance in the cantilevered portion of the push-pull wires.

In contrast to Figure B-9(a), the plots in (c) and (d) were generated by driving the roller with a sinusoid with the user's hand stationary. A plot of the tracking performance when driven by a 5 Hz sine wave with 1 cm peak-to-peak amplitude is shown in Figure B-9(c). A similar plot for a 8 Hz sine wave is shown in Figure B-9(d). Tracking performance degrades significantly in going from 5 Hz up to 8 Hz, where it reaches the -3dB point. From these plots, it was determined that the small motion bandwidth of the device is approximately 8 Hz.

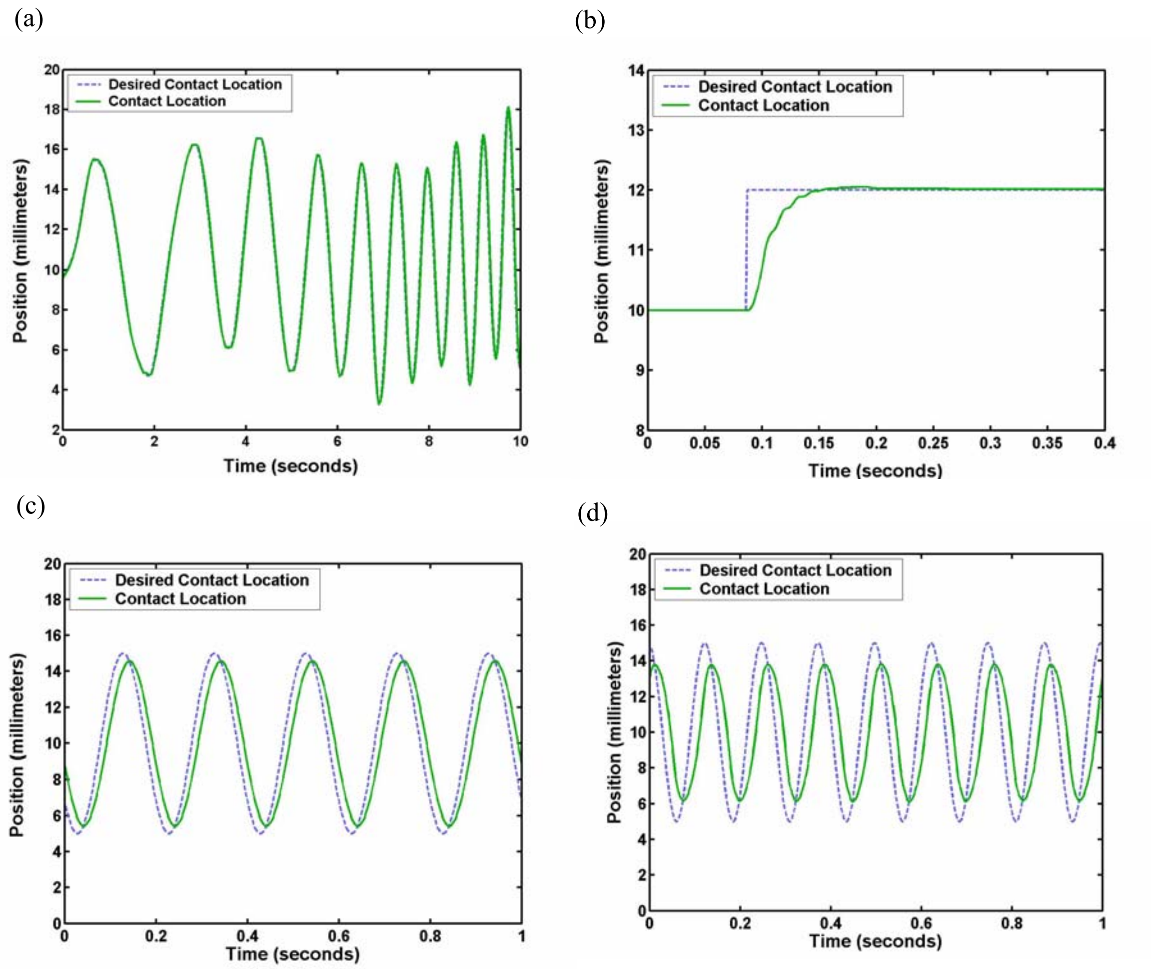

Figure B-9. Performance plots for the contact display device. (a) Tracking plot for the device rendering a stationary object. The desired position is based on the motion of the user's finger. (b) Device response to a 2 mm step input. The response is slightly underdamped with a 50 ms rise time. In contrast to (a) plots (c) and (d) were generated by driving the roller with a sinusoid with the *user's hand stationary*. (c) Tracking plot for the contact display driven by a 5 Hz sine wave with 1 cm peak-to-peak amplitude. (d) Tracking plot for the contact display driven by a 8 Hz sine wave with 1 cm peak-to-peak amplitude. As seen in plot (d), there is considerable lag as the tracking performance falls off. The small motion bandwidth of the device is approximately 8 Hz. Plots shown courtesy of Katherine J. Kuchenbecker of the Stanford Telerobotics Lab.

Appendix C: Kinematics of Motion for Curvature Discrimination Experiments

This appendix outlines the mathematics used to describe the motion of simulated objects during curvature discrimination experiments (section 4.4). As mentioned in section 4.2, the kinematics for the curvature discrimination experiments are slightly more complex than for the object motion experiments (section 4.5). However, as in the object motion experiments, the motion of the contact and object position/angle can be described as a function of the motion of the user's finger. As such, control of the roller position, as described in section 4.2, is still valid for curvature discrimination experiments.

The calculations used to determine the current position of contact with the virtual object (as well as the current position of the object) are based on pure rolling between the virtual object and finger, and are derived for the two-dimensional configuration under which tests were conducted (see Figure 4-6(c) and the figure shown below). Even this simplified scenario results in non-linear equations to describe the kinematics; however, because the subject's range of motion was limited to ±7.5°, the kinematics for real-time simulation can be linearized by using a small angle approximation. The full non-linear solution is provided below. The linearized solution, used in real-time simulations, is also given along with the computed accuracy of this simplification. Refer to Figure C-1 for graphics accompanying the following equations.

The position and motion of the point of contact, P, and the orientation, θ, of the virtual object can be described as a function of the horizontal motion of the user's finger, ΔX_F. The following equation describes the initial position of the point of contact, P_1.

$$P_1 = -(R_d \sin\theta_1)\,\hat{e}_x + (R_d \cos\theta_1 + r_c)\,\hat{e}_y \tag{C.1}$$

where R_d is the distance from the origin (the pivot point) to the center of curvature for each stimulus, r_c is the radius of this disk, and θ_1 is the orientation of the virtual object at time 1. R_d can always be determined from R_w and r_c, because the curves of the stimuli are inscribed in a circular wheel of radius, R_w. Thus,

$$R_d = R_w - r_c \tag{C.2}$$

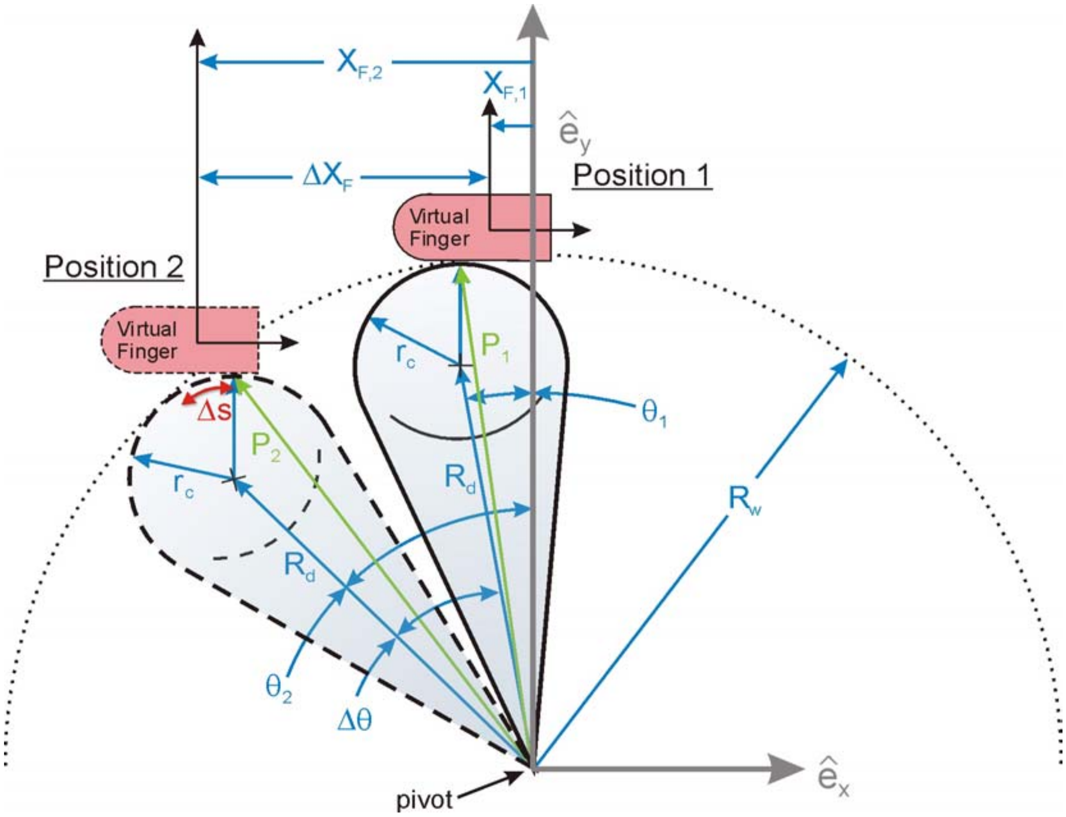

Figure C-1. Schematic representation of the virtual object motion in curvature discrimination experiments. Virtual objects were constrained to follow an arc, pivoting about the origin. The curvature stimuli were small circular disks inscribed on a circular wheel of radius, R_w. Only x and y motions of the virtual finger were allowed (no rotation), so object kinematics can be described purely as a function of finger position, given some initial configuration.

The position at some arbitrary time later, P_2, can be represented similarly.

$$P_2 = -(R_d \sin\theta_2)\, \hat{e}_x + (R_d \cos\theta_2 + r_c)\, \hat{e}_y \tag{C.3}$$

where θ_2 is the orientation of the virtual object at time 2, and the other variables are the same as described for Equation C.1.

Because pure rolling between the finger and the virtual object was prescribed in the kinematic model, the motion of the user's finger can be used to calculate the motion of the virtual object. This allows the simulation to be driven based on measurements of the current location of the user's finger. For pure rolling, the arc-length over which the position of the contact moves on both the finger and object is the same and is described by the equation.

$$\Delta s = r_c\ \Delta\theta \tag{C.4}$$

In this simplified case, the contact is **always** on the top of the object (since the virtual finger is not allowed to rotate), so the position of the user's finger in the x-direction at time 2 ($X_{F,2}$) can be related to the final position of the object using the relation in Equation C.4.

$$X_{F,2} = P_2 \cdot \hat{e}_x - \Delta s = -R_d \sin\theta_2 - r_c\ \Delta\theta \tag{C.5}$$

The following equation relates the user's finger motion to the motion of the contact and object.

$$\Delta X_F = X_{F,2} - X_{F,1} = (-R_d \sin\theta_2 - r_c\ \Delta\theta) - (-R_d \sin\theta_1) \tag{C.6}$$

This equation can be rewritten in terms of the initial orientation and the unknown rotation of the wheel.

$$\Delta X_F = R_d\ (\sin\theta_1 - \sin(\theta_1 + \Delta\theta)) - r_c\ \Delta\theta \tag{C.7}$$

Rewriting this in a suitable form to solve for the unknown rotation angle, $\Delta\theta$, using standard trigonometric identities.

$$\Delta X_F = R_d\ [\sin\theta_1 - (\sin\theta_1 \cos\Delta\theta + \sin\Delta\theta \cos\theta_1)] - r_c\ \Delta\theta \tag{C.8}$$

Rearranging Equation C.8 results in an equation in terms of the previously computed stimulus angle, θ_1, other known constants, and the finger motion in the x-direction, ΔX_F.

$$\Delta X_F = R_d\,[\sin\theta_1(1-\cos\Delta\theta) - \cos\theta_1\sin\Delta\theta] - r_c\,\Delta\theta \tag{C.9}$$

The y-position of the contact and user's finger can be described similarly. While in contact, the change in y-position of the user's finger and the y-position of the contact is identical and is simply a function of the unknown wheel rotation, as is the case for the x-direction shown in Equation C.9.

$$\Delta Y_F = R_d\,(\cos\theta_2 - \cos\theta_1) = R_d\,(\cos(\theta_1 + \Delta\theta) - \cos\theta_1) \tag{C.10}$$

So, if Equation C.9 can be solved for the rotation of the stimulus, $\Delta\theta$, the position of the contact and virtual object can be fully described. A standard numerical approach to solving a nonlinear equation, such as Equation C.9, is to use Newton's Method (also known as Newton-Raphson). The standard form applied to solve for the change in object orientation is:

$$\Delta\theta_{i+1} = \Delta\theta_i - \frac{f(\Delta\theta)|_{\Delta\theta_i}}{f'(\Delta\theta)|_{\Delta\theta_i}} \tag{C.11}$$

where $\Delta\theta_{i+1}$ is the iterated solution for $\Delta\theta$, $\Delta\theta_i$ is the initial guess at the solution for $\Delta\theta$, and f is simply Equation C.9 rewritten by moving ΔX_F to the right hand side of the equation.

$$f = R_d\,[\sin\theta_1(1-\cos\Delta\theta) - \cos\theta_1\sin\Delta\theta] - r_c\,\Delta\theta - \Delta X_F$$

f' is the derivative of f

$$f' = R_d\,[\sin\theta_1\sin\Delta\theta - \cos\theta_1\cos\Delta\theta] - r_c$$

In each iteration, f is evaluated at $\Delta\theta_i$. The solution converges quite rapidly with a suitable initial guess at the solution (see discussion later in this appendix for a suitable initial guess for this solution).

In contrast to the non-linear solution, if the motions of the virtual object will only deviate a small distance from vertical, a small-angle approximation can be applied to Equation C.9, resulting in an equation linear in $\Delta\theta$:

$$\Delta X_F = R_d\,(-\cos\theta_1 - r_c)\,\Delta\theta \tag{C.12}$$

This equation can be rearranged to directly solve for $\Delta\theta$:

$$\Delta\theta = \frac{\Delta X_F}{(-R_d \cos\theta_1 - r_c)} \tag{C.13}$$

Note that for small angles the denominator of the above equation is nearly constant. This quantity represents the instantaneous radius of rotation, and, as one can see from Equation C.2, the denominator is nearly equal to the radius of the wheel, R_w (negated). Thus, a good initial guess, $\Delta\theta_i$, for the non-linear solution of Equation C.11 is $\Delta\theta_i = -\Delta X_F / R_w$.

In the curvature discrimination experiments discussed in section 4.4, the motion of the virtual objects was restricted to approximately ±7.5° of rotation. In these experiments, the radius of the wheel, R_w, was 75 mm. When comparing the solutions of Equation C.11 and Equation C.13 at the extremes of travel, it is seen that there is only a slight difference. For instance, for a finger motion 1 cm from top-dead-center and a stimulus with radius, r_c, equal to 10 mm, the linearized solution gives a net object rotation of -0.1334 radians (or -7.643°) as opposed to the solution from the full non-linear solution of -0.1337 radians (or -7.660°). While the linearized solution underpredicts the rotation by about 0.2% and results in an error in rendered contact location of approximately 0.02 mm, this amount of error is imperceptible (based on the results reported in chapter 4).

It is also interesting to compare the accuracy of the linearized solution to the accuracy of the Phantom^{TM} measurements used to drive our simulation. The joint angles of the Phantom^{TM} are measured using 1000-tick encoders (in quadrature). In combination with the 10:1 gear reduction of the capstan drive and link length of 15 cm, this means that 1 bit of resolution on the encoders is equivalent to about 0.023 mm. Quite coincidentally, this is similar to the worst-case accuracy of the linearized solution. For this reason, the linearized equation was used in real-time computations.

Bibliography

Asamura, N., Yokoyama, N., and Shinoda, H., "Selectively Stimulating Skin Receptors for Tactile Display", Computer Graphics and Applications, IEEE, vol. 18, 1998, pp. 32-37.

Asamura, N., Shinohara T., Tojo Y., Koshida N., and Shinoda H., "Necessary Spatial Resolution for Realistic Tactile Feeling Display." In Proceedings of the 2001 International Conference on Robotics and Automation, IEEE, 2001, pp. 1851-1856.

Bicchi, A., Salisbury, J.K., Brock, D.L., "Contact Sensing From Force Measurements." International Journal of Robotics Research 12(3), 1993 , pp. 249-262.

Biggs, J. and Srinivasan M.A., Chapter 5 in Haptic Interfaces. Handbook of Virtual Environments. K. Stanney, Ed.: London, Lawrence Earlbaum, Inc., 2002.

Brocket, R.W., "Robotic Hands with Rheological Surfaces." Proceedings of the 1985 IEEE International Conference on Robotics and Automation, 1985, pp. 942-946.

Burdea, G.C., Force and Touch Feedback for Virtual Reality. New York: J. Wiley & Sons, 1996.

Caldwell, D.G., Tsagarakis, N., Giesler, C., "An Integrated Tactile/Shear Feedback Array for Stimulation of Finger Mechanoreceptor," Proceedings of the 1999 IEEE International Conference on Robotics and Automation, 1999, pp. 287-292.

Canepa, G.M., M., De Rossi, D., Caiti, A., Parisini, T., "Shape from Touch by a Neural Net." presented at Robotics and Automation, 1992. Proceedings., 1992 IEEE International Conference on Robotics and Automation, 1992.

Chang, D.C., "Tactile Array Sensors and Data Interpretation for Dexterous Robotic Rolling Manipulation." Ph.D. Thesis in Mechanical Engineering: Stanford University, 1995.

Charlebois, M.G., K.; Payandeh, S., "Shape Description of General, Curved Surfaces Using Tactile Sensing and Surface Normal Information." Proceedings of the 1997 International Conference on Robotics and Automation, IEEE, 1997, pp. 2819-2824.

Cohn, M.B., Lam, M., and Fearing, R.S., ``Tactile Feedback for Teleoperation", SPIE Conf. 1833, Telemanipulator Technology, Boston, MA, Nov. 15-16, 1992.

Dario P., Tactile Sensing: Technology And Applications. Sensors And Actuators A-Physical 26(1-3), 1991 pp. 251-256.

Dennerlein, J.T., Millman P.A., and Howe R.D., "Vibrotactile Feedback for Industrial Telemanipulators." Proceedings of the ASME Dynamic Systems and Control Division, Dallas, TX, USA, 1997.

Dreyfuss, H., Tilley, A.R., The Measure of Man and Woman: Human Factors in Design, New York, N.Y. : Wiley, 2002.

Fearing, R.S., Tactile Sensing, Perception and Shape Interpretation, Ph.D. Thesis in Electrical Engineering: Stanford University, 1988.

Fearing, R.S. and Binford T.O., "Using a Cylindrical Tactile Sensor for Determining Curvature." IEEE Transactions on Robotics and Automation, vol. 7, 1991, pp. 806-817.

Fearing, R.S., Moy G., and Tan E., "Some Basic Issues in Teletaction." In Proceedings of the 1997 International Conference on Robotics and Automation, IEEE, 1997, pp. 3093-3099.

Ferrier, N.J. and Brockett, R.W., "Reconstructing the Shape of a Deformable Membrane from Image Data." International Journal of Robotics Research 19(9), 2000, pp. 795-816.

Fischer, H., Neisius, B., and Trapp, R., "Tactile Feedback for Endoscopic Surgery." In Interactive Technology and New Paradign for Healthcare, edited by K. Morgan, R.M. Satava, H.B. Sieburg, R. Mattheus, J.P. Christensen,IOS Press, 1995, pp. 114-117.

Fraden, J., Handbook of Modern Sensors. 2nd edition Springer-Verlag, New York, 1996.

Fukuda, T., Morita, H., Arai, F., Ishihara, H., and Matsuura, H., "Micro Resonator Using Electromagnetic Actuator for Tactile Display." Proceedings of the 1997 International Symposium on Micromechatronics and Human Science, 1997, pp. 143-148.

Gescheider, G.A., "Psychophysics: The Fundamentals." 3rd ed: Lawrence Erlbaum Associates, 1997.

Ghodssi, R., Beebe, D.J., White, V., Denton, D.D., "Development of a Tangential Tactor Using a Liga/MEMS Linear Microactuator Technology." International Mechanical Engineering Congress and Exposition, Microelectromechanical Systems, DSC Vol. 59, Nov. 17-22, 1996, pp. 379-386.

Goodwin, A.W., John K.T., and Marceglia A.H., "Tactile Discrimination of Curvature by Humans Using Only Cutaneous Information from the Fingerpads." Experimental Brain Research, vol. 86, 1991, pp. 663-672.

Gordon, I.E. and Morison V., "The Haptic Perception of Curvature." Perception & Psychophysics, vol. 31, 1982, pp. 446-450.

Haidacher, S. and Hirzinger G., "Contact Point Identification in Multi-Fingered Grasps Exploiting Kinematic Constraints." presented at Proceedings of the 2002 IEEE International Conference on Robotics and Automation, Washington, DC, 2002, pp. 1597 -1603.

Hasser, C.J. and Weisenberger J.M., "Preliminary Evaluation of a Shape-Memory-Alloy Tactile Feedback Display." presented at Proc. of Symposium on Haptic Interfaces for Virtual Environments and Teleoperator Systems, ASME Winter Annual Meeting, 1993, pp. 73–80.

Hasser, C.J. and Daniels, M.W. "Tactile Feedback with Adaptive Controller for a Force-Reflecting Haptic Display." 15th Souther Biomedical Engineering Conference, Dayton, OH, March29-31, 1996, pp. 526-533.

Hayward, V. and Cruz-Hernandez J.M., "Tactile Display Device Using Distributed Lateral Skin Stretch," presented at Symposium on Haptic Interfaces for Virtual Environment and Teleoperator Systems" , IMECE 2000, 2000.

Hogan, N. “Impedance control - An approach to manipulation: Part I. Theory.” Journal of Dynamic Systems, Measurement, and Control - Transactions of the ASME, Volume 107, Issue 1, 1985, pages 1-7.

Howe, R.D. Kontarinis, D.A.; Peine, W.J., "Shape memory alloy actuator controller design for tactile displays," Proceedings of the 34th IEEE Conference on Decision and Control, 1995, pp. 3540-3544 .

Iwata, H.Y., H.; Kawamura, R., Nakaizumi, F; Kawamura, R, "Project Feelex: Adding Haptic Surface to Graphics," presented at Proceedings of SIGGRAPH 2001, 2001.

Johansson, R.S., "How is grasping modified by somatosensory input?" In Motor Control: Concepts and Issues. Dahlem Konferenzen Edited by HUMPHREY DR, FREUND H-J, John Wiley & Sons Ltd, Chichester, 1991, pp. 331-355.

Johansson, R.S. and LaMotte, R.H., "Tactile detection thresholds for a single asperity on an otherwise smooth surface," Somatosensory Research, vol. 1(1), 1983, pp. 21-31.

Johansson, R.S. and Vallbo, Å.B., "Tactile sensory coding in the glabrous skin of the human hand," Trends Neuroscience vol. 6, 1983, pp. 27-31.

Kaczmarek, K.A. and Bach-Y-Rita, P., "Tactile Displays." In W. Barfield and T. Furness, editors, Advanced Interface Design and Virtual Environments. Oxford University Press, 1993.

Kaczmarek, K.A., Webster, J.G., Bach-Y-Rita, P., and Tompkins, W.J., "Electrotactile and Vibrotactile Displays for Sensory Substitution Systems." IEEE Transactions on Biomedical Engineering, vol. 38, 1991, pp. 1-16.

Kammermeier, P., Buss, M., and Schmidt, G., "Dynamic Display of Distributed Tactile Shape Information by a Prototypical Actuator Array." Proceedings of the International Conference on Intelligent Robots and Systems, 2000, pp. 1119-1124.

Kammermeier, P. and Schmidt, G., "Application-Specific Evaluation of Tactile Array Displays for the Human Fingertip," Proceedings of the International Conference on Intelligent Robots and Systems, 2002, pp. 2937-2942.

Kappers, K.M.L., Koenderink, J.J., Lichtenegger, I., "Haptic Identification of Curved Surfaces." Perception and Psychophysics, Vol. 56(#1), July 1994, pp. 53-61.

Klatzky, R.L., & Lederman, S.J., "Intelligent exploration by the human hand." In S. Venkataraman & T. Iberall (Eds.), Dextrous hands for robots. New York: SpringerVerlag, 1990, .pp. 66-81.

Kontarinis, D.A., Son J.S., Peine W.J., and Howe R.D., "A Tactile Shape Sensing and Display System for Teleoperated Manipulation." Proceedings of the 1995 IEEE International Conference on Robotics and Automation, Nagoya, Japan, May 1995, pp. 641-646.

Kontarinis, D.A. and Howe, R.D., Tactile Display of Vibratory Information in Teleoperation and Virtual Environments, Presence-Teleoperaotrs and Virtual Environments, vol. 4, 1995, pp. 387-402. [Kontarinis 1995a]

Lederman, S.J. "The perception of surface roughness by active and passive touch." Bulletin of the Psychonomic Society, 18(5), (1981), pp. 253-255.

Lee, M.H., "Tactile Sensing: New Directions, New Challenges." International Journal of Robotics Research, vol. 19, 2000, pp. 636-43.

Loomis, J.M., and Lederman, S.J. "Tactual Perception." In Boff, K.R., Kaufman, L., and Thomas, J.P. (Eds.), Handbook of perception and human performance: Vol. 2. Congnitive processes and performance. New York: Wiley, 1986, pp. 31.1-31.41.

Louw, S., Kappers, A.M.L, Koenderink, J.J., "Active Haptic Detection and Discrimination of Shape." Perception and Psychophysics, Vol. 64(#7), Oct. 2002, pp. 1108-1119.

Maeno, T., "Tactile Sensation of Humans - Mechanical Dynamics, Analogy and Illusion." Transactions of the Institute of Electrical Engineers of Japan, Part E, vol. 122, 2002, pp. 469-73.

Monkman, G.J., "Electrorheological Tactile Display." Pressence, MIT Press, Vol. 1, No. 2, 1992.

Montana, D.J., "The Kinematics of Contact and Grasp." International Journal of Robotics Research, vol. 7(3), 1988, pp. 17-32.

Moy, G., Wagner, C., and Fearing, R.S. (2000a), "A Compliant Tactile Display for Teletaction." IEEE Int. Conf. on Robotics and Automation, April 2000, 2000, pp. 3409-3415.

Moy, G., Singh, U., Tan, E., and Fearing, R.S. (2000b), "Human Tactile Spatial Sensitivity for Tactile Feedback," In Proceedings of the 2000 International Conference on Robotics and Automation, IEEE, 2000.

Nowlin, W.C., Experimental "Results on Bayesian Algorithms for Interpreting Compliant Tactile Sensing Data." Proceedings of the 1991 IEEE International Conference on Robotics and Automation, 1991, pp. 378-383.

Pawluk, D.T.V., Van Buskirk C.P., Killebrew J.H., Hsiao S.S., and Johnson K.O., "Control and Pattern Specification for a High Density Tactile Array." In Proceedings of the ASME Dyn. Sys. and Control Division, ASME International Mechanical Engineering Congress and Exposition, New York, NY, USA, 1998, pp. 97-102.

Peine, W.J., Wellman, P.S., and Howe, R.D., "Temporal bandwidth requirements for tactile shape displays." Sixth Annual Symposium on Haptic Interfaces for Virtual Environment and Teleoperator Systems, ASME International Mechanical Engineering Congress and Exposition, Dallas, Nov. 15-21, 1997, pp. 107-113.

Petriu, E.M., Das S.R., Yeung S.K., Liu S.-Q., Huang W.-Y., Wang A.-M., and Song A.-G., "Robotic Tactile Perception: Overview and Prospect of Research and Development on Robot Tactile Sensory Technology", Robot, vol. 24, 2002, pp. 362-74.

Johnson K.O. and Phillips J.R., "Tactile spatial resolution: I. Two-point discrimination, gap detection, grating resolution, and letter recognition," Journal of Neurophysiology, vol. 46, 1981, pp. 1177-1191.

Rucci, M. and Dario P., "Development of Cutaneo-Motor Coordination in an Autonomous Robotic System." Autonomous Robots, vol. 1, 1994, pp. 93-106.

Russell, R.A., "A Tactile Sensor Skin for Measuring Surface Contours." IEEE TENCON 1, 1992, pp 262 -266.

Salada, M.A., Colgate J.E., Lee M.V., and Vishton P.M., "Validating a Novel Approach to Rendering Fingertip Contact Sensations." In Proceedings of the 10th Symposium on Haptic Interfaces for Virtual Environment and Teleoperator Systems, 2002, pp. 217-224.

Schiff, W. and Foulke, E., editors. Tactual Perception: A Sourcebook, Cambridge University Press, Cambridge, 1982.

Sheridan, T.B. Telerobotic, Automation, and Human Supervisory Control. Cambridge, MA: The MIT Press, 1992.

Shimoga, K.B., "A Survey of Perceptual Feedback Issues in Dexterous Telemanipulation: Part I, Finger Force Feedback," Proceedings of IEEE Virtual Reality Annual International Symposium, 1993, pp. 263-270.

Shimoga, K.B., "A Survey of Perceptual Feedback Issues in Dexterous Telemanipulation: Part II, Finger Touch Feedback." Proceedings of IEEE Virtual Reality Annual International Symposium, 1993, pp. 271-279.

Shimoga, K.B. and Goldenberg A.A., Soft Robotic Fingertips. I. A Comparison of Construction Materials, International Journal of Robotics Research, vol. 15, 1996, pp. 320-350.

Shimojo, M., "Tactile Sensing and Display." Transactions of the Institute of Electrical Engineers of Japan, Part E, vol. 122, 2002, pp. 465-468.

Siegel, M., "Tactile Display Development: The Driving-Force for Tactile Sensor Development," presented at Haptic Virtual Environments and Their Applications, IEEE International Workshop 2002 HAVE, 2002, pp. 115-118.

Springer, S.L. and Ferrier N.J., "Design and Control of a Force-Reflecting Haptic Interface for Teleoperational Grasping." Journal of Mechanical Design, vol. 124, 2002, pp. 277-283.

Srinivasan, M.A. and R.H. LaMotte, "Encoding of shape in the responses of cutaneous mechanoreceptors. Information Processing in the Somatosensory System. Wenner-Gren Intl. Symposium Series. O. Franzen and J. Westman, Macmillan Press, 1991, pp. 59-69.

Summers, I.R. and Chanter C.M., "A Broadband Tactile Array on the Fingertip." Journal of the Acoustical Society of America, vol. 112, 2002, pp. 2118-2126.

Tachi, S., "Roles of Tactile Display in Virtual Reality." Transactions of the Institute of Electrical Engineers of Japan, Part E, vol. 122, 2002, pp. 461-464.

Tang, H. and Beebe D.J., "A Microfabricated Electrostatic Haptic Display for Persons with Visual Impairments." Rehabilitation Engineering, IEEE Transactions on [see also IEEE Trans. on Neural Systems and Rehabilitation], vol. 6, 1998, pp. 241-248.

Taylor, P.M., Creed, A.J., Sianaki, A.H., Varley, C.J., and Moser, A., "Creating the Illusion of Shape for Virtual Environments." in Innovative Actuators for Mechatronic Systems, IEE Colloquium on, 1995, pp. 7/1-7/7.

Timoshenko S.P. and Gere J.M., Theory of Elastic Stability. McGraw-Hill, 1961, pp. 340-342.

Vallbo, Å.B. and Johansson, R.S., "Properties of cutaneous mechanoreceptors in the human hand related to touch sensation," Human Neurobiology, vol. 3, 1984, pp. 3-14.

Voyles, R.M. Jr., Fedder G., and Khosla P.K., "Design of a Modular Tactile Sensor and Actuator Based on an Electrorheological Gel," Proceedings of the 1996 IEEE International Conference on Robotics and Automation, 1996, pp. 13-17.

Wagner, C.R., Lederman, S.J., Howe, R.D., "A Tactile Shape Display Using Rc Servomotors," Proceedings of the 10th Symposium on Haptic Interfaces for Virtual Environment and Teleoperator Systems, (HAPTICS 2002), 2002, pp. 354-355.

Wellman, P.S., Peine W.J., Favalora G., and Howe R.D., "Mechanical Design and Control of a High-Bandwidth Shape Memory Alloy Tactile Display." Experimental Robotics V, vol. 232, 1998, pp. 56-66.

Yoshikawa, T. and Nagura A., "A Three-Dimensional Touch/Force Display System for Haptic Interface." In Proceedings of the 1999 IEEE International Conference on Robotics and Automation, 1999, pp. 2943-2951.

Zilles, C.B. and Salisbury, J.K., "A Constraint-Based God-Object Method for Haptic Display," In proceedings of the 1995 IEEE/RSJ International Conference on Intelligent Robots and Systems 95. 'Human Robot Interaction and Cooperative Robots', 1995, pp. 146-151.